

THE AUSTRALIAN NATIONAL UNIVERSITY

HONOURS THESIS

---

# GUESSing GALAH

---

*Author:*

Jane Jinying LIN

*Supervisor:*

Prof. Martin ASPLUND

*A thesis submitted in fulfilment of the requirements  
for the degree of Bachelor of Philosophy*

*in the*

Research School of Astronomy and Astrophysics

August 2015

THE AUSTRALIAN NATIONAL UNIVERSITY

## *Abstract*

Research School of Astronomy and Astrophysics

Bachelor of Philosophy

### **GUESSing GALAH**

Jane Jinying LIN

The aim of galactic archaeology is to piece together the history of the assembly of the Milky Way. Studies find that open clusters and accreted satellites show unique, measurable, homogeneous chemical abundances and this enables the technique of chemical tagging to identify stars originating from the same group. The GALAH survey aims to observe one million stars belonging primarily to the Galactic disk using the high-resolution multi-object spectrograph HERMES on the 3.9m Anglo-Australian Telescope. The high resolution, high signal-to-noise GALAH spectra will allow the abundances of up to 30 elements to be determined, covering all of the nucleosynthetic production channels.

This thesis presents the GALAH Ultra Enigmatic Spectroscopic Script (GUESS), a global fitting initial stellar parameter estimation algorithm. GUESS provides initial stellar parameters to the more sophisticated GALAH analysis pipelines in order to minimise computational time, and boost accuracy. The approximate uncertainties for GUESS derived parameters are:  $T_{\text{eff}} = 164$  K,  $\log g = 0.38 \text{ cm s}^{-2}$  and  $[\text{Fe}/\text{H}] = 0.23 \text{ dex}$ . GUESS parameters are found to be comparable with APOGEE, IRFM and ARGOS, and has also found to out perform Theremin. Preliminary results show a dramatic improvement in Theremin when GUESS initial parameters are supplied. GUESS also independently produces radial velocity measurements. GUESS radial velocities are found to be comparable with APOGEE and out performs GAP in consistency. To date, the GUESS parameter-velocity set contains approximately 90000 stars and is the biggest set available within the GALAH collaboration.

## *Acknowledgements*

I would like to thank Martin for being a cool supervisor.

I would like to thank Mike, Katie, Fan, Ly, Luca, Surya, Sean and the GASP team for helping me with the technical aspects and listening to my ramblings during group meetings.

I would like to thank my office mates, floor mates, and friends for keeping me sane throughout the year.

Last but not least, I would like to thank the couch in DF29 for its unconditional support, this thesis is dedicated to you.

# Contents

<b>Abstract</b>	<b>i</b>
<b>Acknowledgements</b>	<b>ii</b>
<b>Contents</b>	<b>iii</b>
<b>List of Figures</b>	<b>v</b>
<b>List of Tables</b>	<b>vii</b>
<b>1 A Primer on Stellar Spectroscopy</b>	<b>1</b>
1.1 Radiative Transfer . . . . .	1
1.1.1 TE vs LTE vs NLTE . . . . .	3
1.2 Spectral Lines . . . . .	6
1.2.1 Line strength . . . . .	7
1.2.2 Line broadening . . . . .	8
1.3 Spectroscopic Stellar Parameters . . . . .	10
1.3.1 Automated pipelines . . . . .	11
1.3.2 Benchmark stars . . . . .	12
<b>2 Galactic Archaeology and GALAH</b>	<b>14</b>
2.1 Galactic Archaeology . . . . .	14
2.1.1 Galactic components . . . . .	15
2.1.2 Chemical tagging . . . . .	17
2.1.3 Ongoing surveys . . . . .	17
2.2 GALAH . . . . .	18
2.2.1 Scientific goals . . . . .	19
2.2.2 Synergistic observations . . . . .	21
2.2.3 Instrument . . . . .	22
2.2.4 Survey strategies . . . . .	23
2.2.5 Data flow . . . . .	25
<b>3 GUESS I- Radial Velocity</b>	<b>28</b>
3.1 GUESS (Part I) . . . . .	28
3.1.1 SNR cut . . . . .	29
3.1.2 Median filter and continuum normalisation . . . . .	30

3.1.3	Cross Correlation . . . . .	31
3.1.4	Uncertainties . . . . .	36
3.2	Comparison with GAP and APOGEE . . . . .	36
3.3	Clusters . . . . .	39
3.3.1	M67 . . . . .	40
3.3.2	47Tuc . . . . .	40
3.4	Comparison of Multiple Reductions . . . . .	41
<b>4</b>	<b>GUESS II- Parameter Estimation</b>	<b>45</b>
4.1	GUESS (Part II) . . . . .	45
4.1.1	Continuum normalisation . . . . .	46
4.1.2	Simplex . . . . .	47
4.1.3	Nearest neighbor . . . . .	52
4.1.4	Compare and contrast . . . . .	58
4.2	Comparison with Other Pipelines . . . . .	58
4.2.1	ASPCAP . . . . .	58
4.2.2	IRFM . . . . .	62
4.2.3	Theremin . . . . .	66
4.2.4	ARGOS . . . . .	71
4.3	Clusters . . . . .	73
4.3.1	M67 . . . . .	74
4.3.2	47Tuc . . . . .	76
4.4	Discussion . . . . .	78
4.4.1	Uncertainties . . . . .	78
4.4.2	Issues . . . . .	79
4.4.3	GUESS 2: Electrical Boogaloo . . . . .	80
<b>5</b>	<b>Application- Local Linear Embedding</b>	<b>81</b>
5.1	Local Linear Embedding . . . . .	81
5.1.1	Number of neighbors . . . . .	84
5.2	The GALAH LLE Projection . . . . .	85
<b>6</b>	<b>Conclusion</b>	<b>89</b>
6.1	Summary of Results . . . . .	89
6.1.1	Radial velocity . . . . .	89
6.1.2	Parameter estimation . . . . .	90
6.2	Future Work . . . . .	90

# List of Figures

1.1	Line formation 1 . . . . .	6
1.2	Line formation 2 . . . . .	7
1.3	Curve of growth . . . . .	8
1.4	Voigt profile . . . . .	9
1.5	Excitation balance . . . . .	10
1.6	Logg dependence of Ca lines . . . . .	11
1.7	vsini profile fitting . . . . .	12
2.1	Image of the Milky Way . . . . .	16
2.2	$\delta C$ distribution . . . . .	20
2.3	Example HERMES spectrum . . . . .	23
2.4	Distribution of GALAH fields on the sky . . . . .	24
2.5	Flow chart of the GALAH data analysis procedure . . . . .	27
3.1	SNR comparison from GAP, median and MAD . . . . .	30
3.2	SNR distribution of 90000 GAP stars . . . . .	31
3.3	Median filtered spectrum . . . . .	32
3.4	Normalisation . . . . .	33
3.5	AMBRE grid . . . . .	34
3.6	Mean subtracted cross correlation . . . . .	35
3.7	Example of cross correlation . . . . .	35
3.8	Continuum problem . . . . .	36
3.9	RV offsets . . . . .	37
3.10	APOGEE-GAP-GUESS comparison . . . . .	39
3.11	RV distribution of 1062 M67 stars . . . . .	40
3.12	RV distributions of 1134 47Tuc stars . . . . .	41
3.13	A successfully reduced star . . . . .	42
3.14	A problematic star . . . . .	43
3.15	SNR comparisons . . . . .	44
4.1	Oracle iterations . . . . .	46
4.2	Normalisation . . . . .	48
4.3	Illustration of the simplex method . . . . .	49
4.4	Problems with the simplex . . . . .	50
4.5	Distributions of median distances for three values of FWHM . . . . .	51
4.6	Different number of neighbors . . . . .	53
4.7	Reconstructed spectrum . . . . .	53
4.8	HR diagram of $\sim$ 1500 stars . . . . .	54

---

4.9	Simplex and nearest neighbor comparison 1 . . . . .	56
4.10	Simplex and nearest neighbor comparison 2 . . . . .	57
4.11	Differences between ASPCAP and GUESS for 37 stars . . . . .	61
4.12	IRFM and GUESS results of 47Tuc and M67 . . . . .	63
4.13	IRFM and GUESS results of NGC362 and NGC288 . . . . .	64
4.14	IRFM and GUESS results of NGC1851 and OmegaCen . . . . .	65
4.15	HR diagrams from GUESS and Theremin . . . . .	68
4.16	Native Theremin . . . . .	69
4.17	Theremin with GUESS initial parameters . . . . .	70
4.18	Differences between ARGOS and GUESS for 329 stars . . . . .	72
4.19	HR diagrams of both GUESS and ARGOS . . . . .	73
4.20	GUESS results of M67 . . . . .	75
4.21	GUESS results of 47Tuc . . . . .	77
4.22	Artefacts . . . . .	79
5.1	LLE vs PCA . . . . .	82
5.2	Neighbor dependence of LLE . . . . .	84
5.3	LLE- $T_{\text{eff}}$ . . . . .	85
5.4	LLE-logg . . . . .	86
5.5	LLE-[Fe/H] . . . . .	86
5.6	Spectra of the outlying group . . . . .	87

# List of Tables

1.1	TE vs LTE vs NLTE . . . . .	5
1.2	24 Gaia benchmark stars . . . . .	13
2.1	HERMES wavelength windows . . . . .	22
2.2	Expected contributions to the GALAH sample . . . . .	24
4.1	Wavelength table for the parameter grid . . . . .	47
4.2	Parameter summary of the model grid . . . . .	47
4.3	Benchmark results for the simplex method . . . . .	52
4.4	Benchmark results for the nearest neighbor method . . . . .	55
4.5	Example output from GUESS . . . . .	59
4.6	Differences between ASPCAP and GUESS for 37 stars . . . . .	60
4.7	Difference between IRFM and GUESS for 6 clusters . . . . .	62
4.8	Parameter ranges for the model grid used in Theremin . . . . .	66
4.9	Native Theremin . . . . .	71
4.10	Theremin with GUESS initial parameters . . . . .	71
4.11	Differences between ARGOS and GUESS for 329 stars . . . . .	72
4.12	Uncertainty table . . . . .	78

# Chapter 1

## A Primer on Stellar Spectroscopy

STELLAR spectroscopy is the study of spectral features in the spectra of stars. This chapter provides an overview of its underlying physics.

### 1.1 Radiative Transfer

Radiative transfer is the dominant physical mechanism underlying stellar spectroscopy. It is primarily concerned with the photosphere, where photons are emitted. In this layer, radiative transfer is the main way of energy transportation. Other methods of energy transfer are also present, such as convection and in some extreme cases, conduction. But their effects are negligible in the photosphere, where the stellar spectrum is formed.

To better understand the mathematical formulation of radiative transfer, the notion of specific intensity,  $I_\nu$ , is introduced. This is the intensity of a particular frequency  $\nu$ . It is defined to be-

$$I_\nu = \frac{dE_\nu}{\cos \theta dA d\omega dt d\nu} \quad (1.1)$$

Where  $d\nu$  is the spectral band,  $dE_\nu$  is the energy within this band,  $dt$  is the time and  $dA$ ,  $d\omega$ ,  $\theta$  are geometrical elements associated with the position of the observer, and the area of photosphere emitting the radiation. Integrating  $I_\nu$  over all spectral bands yields the over all intensity  $I$ .

From specific intensity, one can calculate the mean specific intensity ( $J_\nu$ ) and the flux ( $F$ ). They are defined as the following-

$$J_\nu = \frac{1}{4\pi} \int_0^{2\pi} \int_0^\pi I_\nu \sin \theta d\theta d\phi \quad (1.2)$$

$$F = \int_0^{2\pi} \int_0^\pi I_\nu \sin \theta \cos \theta d\theta d\phi \quad (1.3)$$

Radiative transfer describes the change in  $I_\nu$  over a length of a medium. There are two basic factors which affect the emergent intensity- emission (characterised by the monochromatic emissivity  $j_\nu$ ) and extinction (characterised by the monochromatic extinction coefficient  $\alpha_\nu$ ). Denoting the geometrical path as  $s$ , one can write the radiative transfer equation to be-

$$dI_\nu = j_\nu ds - \alpha I_\nu ds \quad (1.4)$$

Further defining the monochromatic optical path length to be  $d\tau_\nu \equiv \alpha \nu ds$  and the source function to be  $S_\nu \equiv \frac{j_\nu}{\alpha_\nu}$ . Dividing through by  $\alpha_\nu$  yields-

$$\frac{I_\nu}{d\tau_\nu} = S_\nu - I_\nu \quad (1.5)$$

Integrating the optical path along  $s$  yields the monochromatic optical thickness  $\tau_\nu$ . This is essentially the length a photon can travel before being absorbed. The formal solution to Equation 1.5 as a function of optical thickness is-

$$I_\nu(\tau_\nu) = I_\nu(0)e^{-\tau_\nu} + \int_0^{\tau_\nu} S_\nu(t_\nu) e^{\tau_\nu - t_\nu} dt_\nu \quad (1.6)$$

Where  $I_\nu(0)$  is the initial intensity. The first term corresponds to the attenuation of the initial intensity and the second term is the combination of emission and re-attenuation within the medium. The resulting emergent intensity is strongly dependent on the relative values of the optical thickness, source function and initial intensity.

The source function is very important in radiative transfer. It is the sum of the emission and extinction coefficients of all species present in the medium. In fact, both flux and mean intensity can be interpreted as the depth-weighted samplings of the source function. Approximating the source function as a polynomial expansion, one can derive the three Eddington-Barbier approximations near the surface-

1.  $I_\nu^+(\tau_\nu = 0, \cos \theta) \approx S_\nu(\tau_\nu = \cos \theta)$
2.  $J_\nu(\tau_\nu = 0) \approx \frac{1}{2}S_\nu(\tau_\nu = 1/2)$

$$3. F_\nu(\tau_\nu = 0) \approx \pi S_\nu(\tau_\nu = 2/3)$$

The first one is especially useful, as it states at the surface the outgoing emergent intensity ( $I_\nu^+$ ) is approximately the source function at one optical depth under the surface. The photon contributions from deeper within the star is reabsorbed before reaching there. This causes phenomena such as limb darkening.

Further in the star, the source function can be expanded as a Taylor-McLaurin series. There, the photons are trapped and the radiation field is isotropic. As  $\tau_\nu \gg 1$ , the new approximations are:

$$1. I_\nu(\tau_\nu, \cos \theta) \approx S_\nu + \cos \theta \left[ \frac{dS_\nu(t_\nu)}{dt_\nu} \right]_{\tau_\nu}$$

$$2. J_\nu \approx S_\nu$$

$$3. F_\nu(\tau_\nu) \approx \frac{4\pi}{3} \left[ \frac{dS_\nu(t_\nu)}{dt_\nu} \right]_{\tau_\nu}$$

In the last approximation, flux is proportional to the gradient of the source function. This is due to the presence of slight anisotropy at such depths.

### 1.1.1 TE vs LTE vs NLTE

The source function is vital in solving radiative transfer. However obtaining a good estimate requires accurate atomic level information on all species in the medium and hence is challenging in most cases. There are three main types of atomic transitions which will absorb, emit and scatter photons (and other particles), their likelihoods are determined by the Einstein coefficients. The three types are:

1. Bound-bound, transitions between two bound levels of an atom. This includes radiative, induced, collisional and spontaneous excitations/de-excitations.
2. Bound-free, between a free electron and an atom. This includes induced, collisional and spontaneous photo-ionisation/recombination.
3. Free-free, between two free electrons. This includes scattering and collisions.

In thermodynamical equilibrium (TE), all processes are balanced and are in equilibrium with each other. There are no changes macroscopically and all the microscopic changes are balanced. All equipartition laws hold at a unique temperature. Local thermodynamical equilibrium (LTE) is similar, but with temperature varying extremely slowly in space, such that within a small neighborhood, the conditions fulfil TE.

In both TE and LTE, the level populations are well defined by the local temperature and by three distributions- the Maxwell distribution for speed and velocity (Equation 1.7), the Boltzmann distribution for excitation (Equation 1.8) and the Saha distribution for ionisation (Equation 1.9).

$$\frac{n(\mathbf{v})}{N} d\mathbf{v} = \left( \frac{m}{2\pi kT} \right)^{1/2} e^{-\frac{mv^2}{2kT}} d\mathbf{v} \quad (1.7)$$

Maxwell's equation, where  $n$  is the portion of particles at velocity  $\mathbf{v}$ ,  $N$  is the total number particles,  $m$  is the mass,  $k$  is the Boltzmann's constant and  $T$  is the temperature.

$$\frac{n_l}{N} = \frac{g_l}{U(T)} e^{-\frac{\chi_l}{kT}} \quad (1.8)$$

Boltzmann's equation, where  $n_l$  is the portion of particles at  $l$ th excitation state,  $\chi_l$  is the excitation energy of the state,  $U(T)$  is the partition function and  $g_l$  is the statistical weight (i.e. the number of microstates given a macrostate).

$$\frac{n_i}{n_{i+1}} = \frac{2U_{i+1}}{N_e U_i} \frac{2\pi m_e k T^{3/2}}{h^2} e^{-\frac{\chi}{kT}} \quad (1.9)$$

Saha's equation, where  $n_i$  is the portion of particles in the  $i$ th ionisation state,  $N_e$  is the free electron density and  $\chi$  is the ionisation energy from  $i$ th state to  $i + 1$ th state.

In both TE and LTE, the source function ( $S_\nu$ ) can be described by the Planck function-

$$B_\nu(T) = \frac{2h\nu^3}{c^2} \frac{1}{e^{h\nu/kT} - 1} \quad (1.10)$$

Where  $h$  is the Planck constant. Equation 1.10 reduces down to Wiens approximation when  $\frac{h\nu}{kT} \gg 1$  and Rayleigh-Jeans approximation when  $\frac{h\nu}{kT} \ll 1$ . Integrating  $B_\nu$  over all  $\nu$  gives the Stefan-Boltzmann law  $B(T) = \sigma T^4/\pi$ , where  $\sigma$  is the Stefan-Boltzmann constant.

There are multiple ways for electrons to move between states- radiative (a photon is absorbed), collisional (mechanical energy from collisions), spontaneous (de-excitation without provocations) and stimulated (de-excitation by a passing photon). The above distributions hold when collision dominates over radiation.

All matters become more complicated in non-local thermodynamical equilibrium (NLTE). Similar to TE and LTE, NLTE follows statistical equilibrium- the assumption that the radiation fields and level populations ( $n$ ) remain constant with time. Mathematically-

$$\frac{dn_i}{dt} = \sum_{j \neq i}^N n_j P_{ij} - n_i \sum_{j \neq i}^N p_{ij} = 0 \quad (1.11)$$

Where  $P_{ij} = R_{ij} + C_{ij}$ ,  $C_{ij}$  and  $R_{ij}$  are the collisional and radiative rates, respectively.

However the local Saha-Boltzmann equilibrium no longer applies (Table 1.1 gives a summary of the applicability of distributions). Qualitatively, this means the local level populations depend on  $J_\nu$  at different locations and frequencies, which in turn are dependent on the level populations everywhere else. This requires solving the radiative transfer and the rates equations simultaneously at all locations.

TABLE 1.1: Summary of conditions of TE, LTE and NLTE

distribution	TE	LTE	NLTE
Maxwell	yes	yes	normally
Boltzmann	yes	yes	no
Saha	yes	yes	no
$S_\nu$	$= B_\nu$	$= B_\nu$	$\neq B_\nu$
$I_\nu$	$= B_\nu$	$\neq B_\nu$	$\neq B_\nu$
$J_\nu$	$= B_\nu$	$\neq B_\nu$	$\neq B_\nu$
$F_\nu$	$= 0$	$\neq 0$	$\neq 0$

The photosphere is usually assumed to be both 1D and LTE, thus simplifying the source function to the Planck function in one direction only. This means that it is possible to solve radiative transfer if the local temperature is known. In this case, the effects of NLTE on the level populations  $n$  can be accounted for by the departure coefficients  $b = n/n_{LTE}$ .

In an ideal world, one would like to have all atomic transitions computed under 3D-NLTE. However due to the coupled nature of level populations and rates, NLTE calculations are computationally expensive and requires far more atomic data than LTE. Currently, only 10-15 elements have been treated under 1D-NLTE and only two under 3D-NLTE (lithium and oxygen).

## 1.2 Spectral Lines

Figure 1.1 illustrates the formation of a line under the Eddington-Barbier approximation.

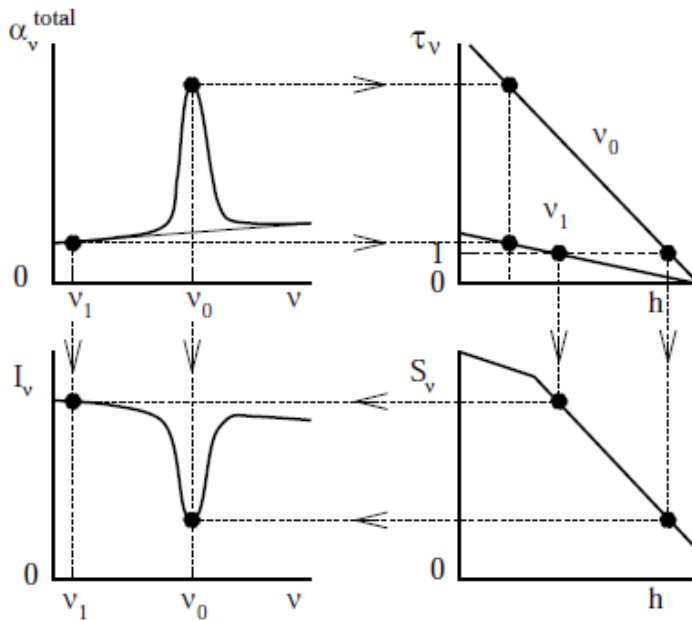


FIGURE 1.1: Formation of a line under the Eddington-Barbier approximation from a thick homogeneous medium. Figure taken from Rutten (2003).

Intuitively, the extinction coefficient  $\alpha_\nu$  (upper left) determines the optical depth ( $\tau_\nu$ ) at various heights ( $h$ ) below the atmosphere (upper right). The larger the extinction, the steeper the  $\tau_\nu$  profile. The Eddington-Barbier approximation states that the emergent intensities ( $I_\nu$ , lower left) are the source function at  $\tau_\nu = 1$  (lower right).

For very strong lines, there are double emission features in the line cores, shown in Figure 1.2.

In Figure 1.2, the atmosphere has a temperature rise in the chromosphere, shown by the deviation from the Planck function at high  $h$  (bottom right). The initial dip of intensity at  $\nu_1$  (bottom left) is caused by this temperature difference between the two layers.

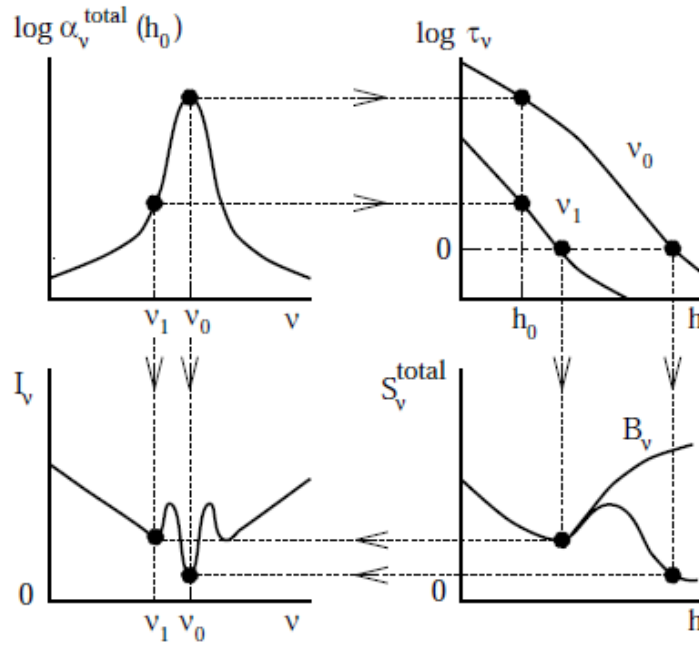


FIGURE 1.2: Formation of double emission features at the core of a very strong line.  
Figure taken from Rutten (2003).

### 1.2.1 Line strength

The strength (depth) of a line is dependent on multiple factors such as temperature, pressure and elemental abundance. Temperature is the most dominant factor controlling line strength, due to its power law and exponential dependences in ionisation (Equation 1.9) and excitation (Equation 1.8). For most lines, increasing temperature means an increase in strength, until some maximum is reached, then followed by a decrease. The increase in strength arises from the increase of excitation and the decrease arises from the negative H ion causing an increase in opacity.

Line strength is also pressure dependent. For FGK stars, pressure can be correlated to surface gravity (Section 1.3). Generally, lower surface gravity corresponds to stronger lines. However its effect is substantially smaller than temperature.

The changes in line strength with respect to abundance is illustrated by the curve of growth in Figure 1.3, which plots the abundance against equivalent width.

There are three stages in the curve of growth- in the first stage, the lines are weak, the strength is dominated by the Doppler core in a linear fashion. In the second stage, the line saturates, resulting the curve to be asymptotically approaching constant strength.

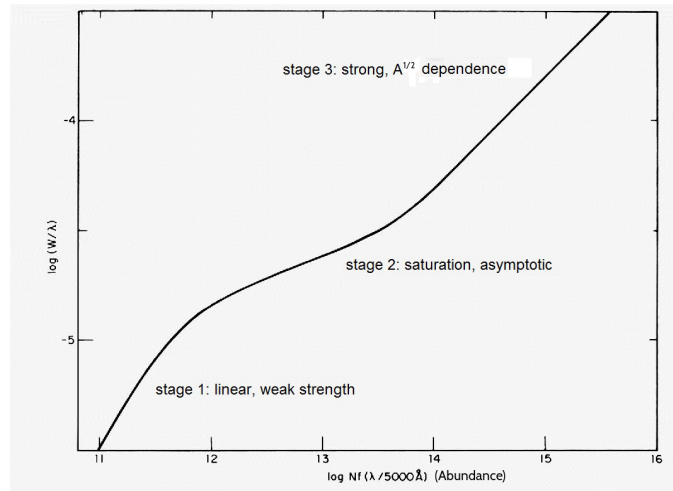


FIGURE 1.3: Curve of growth for an element, with equivalent width in the y axis and abundance in the x axis. Figure taken from Aller (1991).

Finally in the last stage, the strength is dependent on the atomic absorption of the line species, showing  $A^{1/2}$  dependence (where  $A$  is abundance).

### 1.2.2 Line broadening

There are a number of ways in which a spectral line can be broadened. They can be categorised into two groups- local and non-local broadenings. The local broadenings are-

- Natural line broadening

It occurs when an electron is spontaneously de-excited. The uncertainty principle relates the life time of the excited state and its transition energy. This means a shorter life time corresponds to a larger uncertainty in energy and hence inducing a broad emission. This broadening introduces a Lorentzian profile into the lines.

- Collisional broadening (pressure broadening)

It is due to the interactions with other local particles. There are two forms- impact pressure broadening and quasistatic pressure broadening. The former is when the emission is interrupted by collisions, limiting the time of the process and increasing the energy uncertainty. Again a Lorentzian profile is introduced. The latter is due to the presence of other particles shifting the energy levels of the emitting particle. Generally, a Gaussian profile is introduced.

- Thermal broadening

It occurs due to the thermal motions of the particles. Their velocities (governed by

the Maxwell distribution) causes the lines to be Doppler shifted. A Gaussian profile is introduced.

The overall profile is the convolution of all individual profiles, named the Voigt profile, pictured in Figure 1.4.

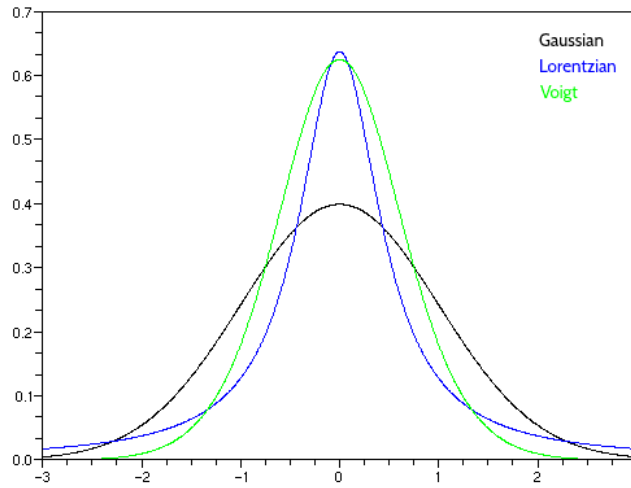


FIGURE 1.4: Voigt profile (green) resulting from the convolution of a Gaussian (black) and a Lorentzian (blue).

The non-local effects are-

- Microturbulence and macroturbulence

They are two parameters introduced in 1D stellar atmosphere models. Both are due to the convection motions in the upper layers of the star and are generally described by Gaussian profiles.

- Rotational broadening

Due to the rotation of the star causing Doppler broadening of the lines.

- Instrumental broadening

Broadening of the spectral lines introduced by the spectrograph. Normally takes the form of a Gaussian.

### 1.3 Spectroscopic Stellar Parameters

Effective temperature ( $T_{\text{eff}}$ ), surface gravity ( $\log g$ ), metallicity([Fe/H]) and rotational velocity ( $v\sin i$ ) are the fundamental stellar parameters on which all spectroscopic analyses base on. Multiple methods exist in obtaining them (e.g., spectroscopy, photometry and asteroseismology). This section focuses on the spectroscopic approaches.

Iron abundance, or metallicity ([Fe/H]) is calculated by measuring the equivalent width of the lines and obtaining the abundances from the curve of growth.

Effective temperature ( $T_{\text{eff}}$ ) has the most dominant effect on the observed spectra. For stars cooler than 8000K, the Balmer lines can serve as excellent  $T_{\text{eff}}$  indicators, as they have virtually no  $\log g$  dependence.  $T_{\text{eff}}$  is derived by fitting the Balmer profile with synthetic spectra. In this approach, continuum regions must be carefully selected and the line core is excluded from the fit as it is subject to NLTE effects.

$T_{\text{eff}}$  can also be derived from the excitation balance of metal lines. Excitation equilibrium dictates that the abundances from the same element must agree for all excitation potentials (EPs). Generally FeI lines are used to perform the balance. Figure 1.5 shows changes on excitation balance as  $T_{\text{eff}}$  is changed.

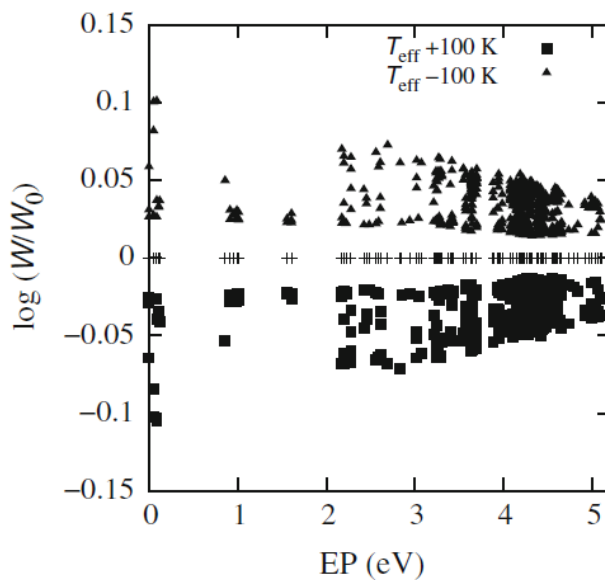


FIGURE 1.5: Plot of EP (x axis) against abundance (y axis). The crosses represent the excitation balance at the ‘correct’  $T_{\text{eff}}$ , showing no trend in EP. The squares and triangles are deviations from the ‘correct’  $T_{\text{eff}}$ . The trends in EP are proportional to the deviations. Figure taken from Niemczura et al. (2014).

Surface gravity ( $\log g$ ) can be derived from the stellar radius and mass, however this is complicated as these quantities are difficult to measure directly. As eluded to previously,  $\log g$  affects the abundances of certain lines. This effect is especially significant for Ca lines, as illustrated in Figure 1.6.

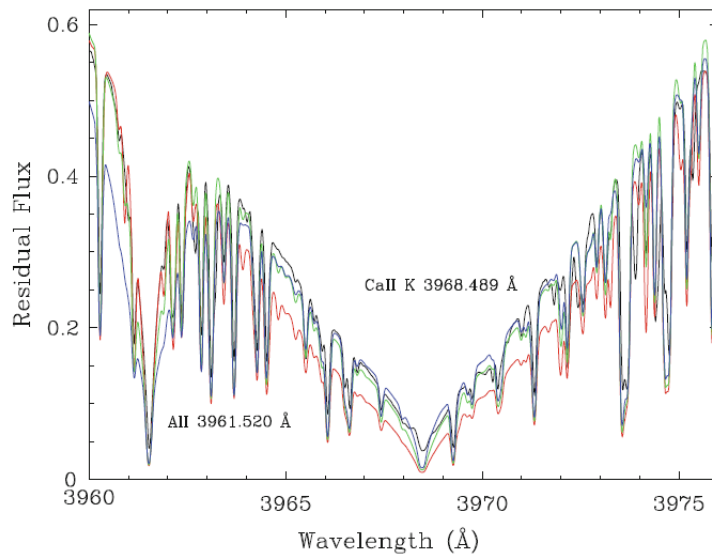


FIGURE 1.6: Plot of the observed CaII H line (black) with three synthetic spectra at different  $\log g$ s over plotted (red, green and blue, with  $\log g = 3, 4$  and  $5$ , respectively).

Figure taken from Niemczura et al. (2014).

In addition to line profiles,  $\log g$  can also be obtained by performing ionisation balance. Ionisation equilibrium dictates that the abundances from the different stages of ionisation of the same element must agree.

Stellar rotation ( $v \sin i$ ) is a line broadening mechanism, it changes the width and the depth of the line whilst conserving equivalent width.  $v \sin i$  can be found by fitting the observed line profiles to synthetic rotational profiles, as shown in Figure 1.7. In this process, it is vital to only select the lines free of strong collisional broadening and correct for instrumental broadening before comparison.

### 1.3.1 Automated pipelines

Presently, two methods exist in automatic derivations of stellar parameters with spectroscopy—the synthesis method and the equivalent width (EW) method. The former involves the computation of synthetic model spectra and finding the synthetic spectrum which best

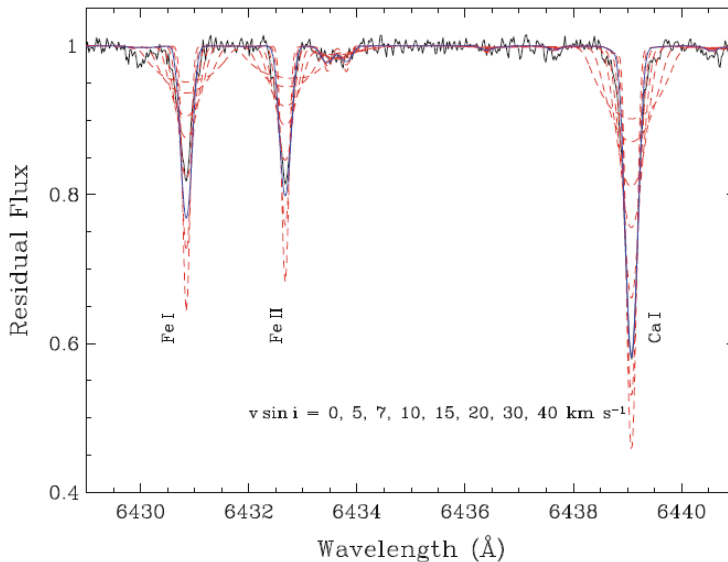


FIGURE 1.7: Plot of the observed spectrum (black) with eight synthetic rotational spectra from  $v \sin i = 0$  to 40 km/s over plotted (red). The best fitting model is in blue ( $v \sin i = 7$  km/s). Figure taken from Niemczura et al. (2014).

fits the observed spectrum. The quality of the fit can be assessed by many metrics, for example, a popular choice being  $\chi^2$ . The latter, the EW method derives stellar parameters directly from the observed spectrum (for example, by performing excitation/ionisation balance on selected lines). These parameters are iterated and compared to predicted values from different model atmospheres to finalise the parameters.

Both methods have advantages and disadvantages. The EW method is quicker as it only focuses on a number of lines, whereas the synthetic method requires a well populated model grid and substantial wavelength coverage. On the other hand, the EW method relies heavily on the cleanliness and the choices of the lines. Blended and/or weak lines can easily compromise its results.

The abundances of individual elements are determined after the stellar parameters are finalised. They are found by finding the best matching model abundances.

### 1.3.2 Benchmark stars

The integrity of a pipeline can be tested by applying it on the benchmark stars. They are stars with stellar parameters derived by methods completely independent of spectroscopy (e.g., photometry and asteroseismology). They are selected to cover the HR diagram and

stellar parameter space. The degree of agreement between the pipeline results and the literature results is an indication of its trustworthiness.

The most well studied benchmark star is the sun, however it is representative of only one spectral class. The Gaia benchmark stars (Jofré et al. (2014)) are a library of stars which populate the majority of parameter space. They are particularly useful in pipeline calibrations because they are also analysed by the eleven nodes in the Gaia-ESO survey (Chapter 2, 2.1.3), thereby providing another source of comparable results. Table 1.2 lists 24 Gaia benchmark stars and their parameters.

TABLE 1.2: Table of the 24 Gaia benchmark stars. The values are from the April 2014 release of Gaia FGK stellar parameters.

star	spec. type	[Fe/H] [dex]	$T_{\text{eff}}$ [K]	$\log(g)$ [ $\text{cm s}^{-2}$ ]
Procyon	F5IV-V	0.01	6554	3.99
HD84937	sdF5	-2.03	6356	4.15
HD49933	F2V	-0.41	6635	4.2
DeltaEri	K1III-IV	0.06	4954	3.75
HD140283	sdF3	-2.36	5514	3.57
EpsFor	K2V	-0.6	5123	3.52
BetaHya	G0V	-0.04	5873	3.98
HD22879	F9V	-0.86	5868	4.27
TauCet	G8.5V	-0.49	5414	4.49
18Sco	G2Va	0.03	5810	4.44
MuAra	G3IV-V	0.35	5902	4.3
BetaVir	F9V	0.24	6083	4.1
Arcturus	K1.5III	-0.52	4286	1.64
HD122563	F8IV	-2.64	4587	1.61
MuLeo	K2III	0.25	4474	2.51
EpsVir	G8III	0.15	4983	2.77
XiHya	G7III	0.16	5044	2.87
HD107328	K0IIIb	-0.33	4496	2.09
HD220009	K2III	-0.74	4275	1.47
AlphaTau	K5III	-0.37	3927	1.11
AlphaCet	M1.5IIIa	-0.45	3796	0.68
BetaAra	K3Ib-II	-0.05	4173	1.04
GammaSge	M0III	-0.17	3807	1.05
EpsEri	K2Vlk:	-0.09	5076	4.6

## Chapter 2

# Galactic Archaeology and GALAH

OUR local galaxy, the Milky Way, is a barred spiral galaxy. Most of its stars are located in the disk. The disk stars are relatively young and are concentrated in the spiral arms which extend out from the central bulge. The number of spiral arms is a controversial issue, with the current consensus being four (Urquhart et al. (2014)). Our sun is located on the Orion-Cygnus arm, roughly 8kpc away from the galactic centre.

Over all, it is estimated that the Galaxy contains 100 billion stars and is the host of at least 100 billion planets. It is estimated to contain  $1.5 \times 10^{12}$  solar masses and an age of 13Gyr. Most of the matter in the Galaxy is stored in its dark matter and hot gas halos, both of which extend far beyond the visible structure.

The Milky Way is a dominant member of the Local Group of galaxies. This group also contains one other large galaxy- Andromeda and several smaller galaxies like Triangulum and numerous satellites. Going further out, the Local Group is a part of the Virgo Supercluster.

This chapter will describe galactic archaeology- the study of fossil remnants of the early galaxy to reconstruct its past history and present an overview on the GALAH survey.

### 2.1 Galactic Archaeology

In 1962, Eggen, Lynden-Bell and Sandage (ELS) published a remarkable paper on galactic evolution- *Evidence from the motions of old stars that the Galaxy collapsed* (Eggen et al.

(1962)). In this paper, the U, V, W motions<sup>1</sup> of 221 dwarf stars are analysed to compute their eccentricities and angular momenta, relying on the fact that the average time for which this information is lost is much longer than the age of the Galaxy. It is found that metal poor stars are correlated with higher eccentricities. From this, ELS argued that the Milky Way formed from the rapid collapse of a uniform isolated gas cloud.

This paper is of high impact as it showed that by studying the kinematics and chemical composition of the present day Galaxy, it is possible to piece together its past evolution.

The collapse picture from ELS does not remain unchallenged. In 1978, Searle and Zinn published a paper in which the abundances of 177 red giants in 19 globular clusters are measured. They found there to be no radial abundance gradient in the clusters and the abundance distribution is independent of galactocentric distance (Searle and Zinn (1978)). This does not fit with the rapid collapse halo scenario, for which the metallicity should be distance dependent and with a small age spread. Instead, they proposed a scheme of hierarchical aggregation of smaller elements in the early universe.

The general consensus that emerged from the past two decades, based on cold dark matter (CDM) simulations and direct observations, is a mixture of gas cloud collapsing and galactic merging. In broad brush strokes, after the epoch of reionisation, the dark matter halo is believed to have formed first. Dark matter pulls baryonic matter into the proto-galaxy, causing violent gas in-falls and accretion of gases around the central black hole. It is also around this time, when the first of the globular clusters formed, as a result of merging satellite galaxies. As time passes, the Galaxy settles down and most of the remaining baryons start to form the disk. The process of satellite accretion plays an integral role in the build up of the disk and the bulge, as shown by CDM simulations. This process appears to have taken place before  $z \sim 2$ , making direct observations impossible. Hence efforts are focused on the reconstruction using the present day Galaxy.

### 2.1.1 Galactic components

It is generally agreed upon that our Galaxy has four visible components- the central bulge/bar, the thin and thick disks and a stellar halo.

The Milky Way has a small boxy bulge, as shown by Figure 2.1. The exact age of the bulge is poorly defined, but colour magnitude diagrams (CMDs) show it being old. Its oldness

---

<sup>1</sup>The U, V, W are components of velocity of a star in the directions of galactic anticenter, galactic rotation and the north galactic pole, with respect to the local standard of rest.

is also confirmed by metallicity measurements of red giant stars in the bulge (McWilliam and Rich (1994)). The giants have alpha enhanced abundances and are similar to the older stars in the disk. The alpha elements are produced during core collapse supernovae, suggesting rapid chemical evolution. The formation history of the bulge is also poorly understood. Two competing scenarios have been proposed- the bulge as a product of merger or a product of galactic internal instabilities. Understanding the formation of the bulge is one of the major goals in galactic archaeology.

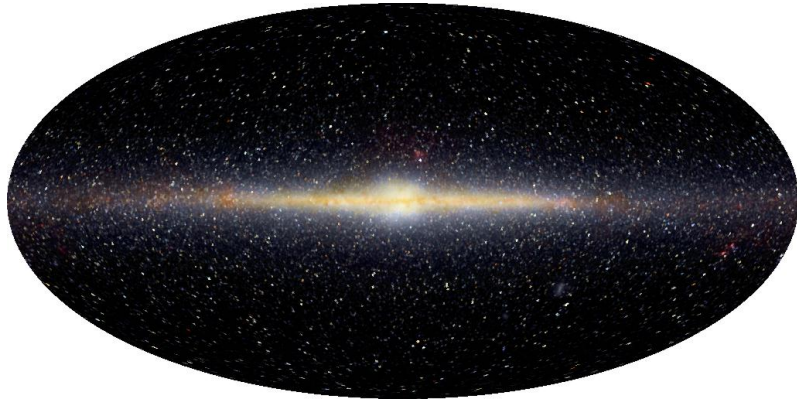


FIGURE 2.1: Image of the Milky Way taken by the COBE satellite.

The disk is the dominating feature in Figure 2.1. It has two parts- the thin disk, where most of the star light is concentrated and a fainter engulfing thick disk. The thick disk spans approximately 1kpc above the galactic plane (Gilmore and Reid (1983)) and is three times thicker and ten times less bright than the thin disk. Their stellar populations also differ, with the thick disk stars being significantly more metal poor than their thin disk counterparts. Current theory suggests the thick disk formed from the heating of the early stellar disk by accretion or merging.

The stellar halo is a spherical distribution of stars above and below the disk, spanning roughly 40kpc. It contains over a hundred globular clusters and some of the oldest stars known in the Galaxy (around 12Gyr, Kalirai (2012)). It is extremely faint, as it contains only approximately 1% of the total stellar mass. In contrast to the disks, the halo is almost entirely supported by its velocity dispersion. It is composed of a mixture of accreted stars from satellites (which underwent chemical evolution before hand) and locally formed stars.

In addition to the visible components, the Milky Way also has a dark matter halo, which contributes to more than 90% of the total mass in the Galaxy, extending at least 100kpc from the centre. The shape of the halo is believed to be spheroidal (Ibata et al. (2001)).

### 2.1.2 Chemical tagging

A complete reconstruction of the Galaxy's history is challenging, as eons of heating cause integrals of motion to be lost. Star forming clusters are dissolved quickly due to dynamical interactions such as external tidal stripping. Hence it is extremely difficult to recover star forming sites kinematically. However it is not entirely impossible as few clusters have been identified in phase space (e.g., the Argus association- De Silva et al. (2013) and the Wolf 360 group- Bubar and King (2010)). These clusters have ages around 2-3 Gyrs- young compared to the age of the Galaxy. Thus it remains problematic in recovering older sites.

Fortunately this issue can be approached chemically. One of the driving ideas behind galactic archaeology is *chemical tagging* (Freeman and Bland-Hawthorn (2002)) which finds lost cluster members by identifying them in chemical space. It relies on two fundamental assumptions-

1. Star forming sites have homogeneous abundance patterns.
2. The patterns differ from cluster to cluster in a measurable degree.

Observations (e.g., Letarte et al. (2010)) have shown that the building blocks of the Galaxy- the accreted satellites have undergone different chemical evolutions compared to the stars formed in situ. Open clusters have also been found to be internally homogeneous at the uncertainty level of 0.05 dex (e.g., De Silva et al. (2007)). This is confirmed theoretically by Bland-Hawthorn et al. (2010) and in simulations by Feng and Krumholz (2014).

In addition to internal homogeneity, chemical tagging also requires the patterns to vary from cluster to cluster so different clusters can be separated out. This assumption is satisfied qualitatively by the degree of abundance spread observed in existing spectroscopic samples (e.g., Bensby et al. (2014)). A more quantitative discussion on the dimensionality of GALAH chemical space is given in Section 2.2.1.

### 2.1.3 Ongoing surveys

In this section, a number of ongoing surveys in galactic archaeology are described.

The Apache Point Observatory Galactic Evolution Experiment (APOGEE, Holtzman et al. (2015)) is a part of the Sloan Digital Sky Survey (SDSS). The first phase APOGEE-I was conducted in three years from 2011 to 2014, the second phase is being planned for

both hemispheres from 2014 to 2020. The main goal of APOGEE-I is to observe 150000 stars to map out the kinematical and chemical structure of the Milky Way. APOGEE utilises a multi-object spectrograph which observes 300 stars simultaneously at a resolution of 22500, in the H band ( $1.51 - 1.7 \mu\text{m}$ ). The observations are made using the SDSS 2.5m telescope. Accurate radial velocities and elemental abundances of 15 species are released with the data.

The LAMOST Experiment for Galactic Understanding and Exploration (LEGUE, Deng et al. (2012)) is a four year galactic structure survey with the aim of acquiring spectra of 7.4 million stars. The main scientific goals of LEGUE include deriving kinematic features and abundance for the thick and thin disks, recovering stellar moving groups as remnants of accreted dwarf galaxies. LEGUE will be conducted in three components—the galactic spheroid, the disk and the anticenter. Observations will be carried out on the 6m LAMOST telescope at a resolution of 1800, with a wavelength window of 3700-9000Å. LAMOST also uses a multi-object spectrograph capable of observing 4000 targets in a single pointing. Most of LEGUE spectra will have radial velocity and metallicity uncertainties on the order of  $\sim 7\text{km/s}$  and 0.3 dex, respectively. LEGUE will also be providing abundances of alpha elements.

The Gaia-ESO Public Spectroscopic Survey (Gilmore et al. (2012)) is the ground complement of the Gaia space mission. Gaia will obtain astrometry for one billion stars brighter than  $G=20$ . Gaia-ESO will provide follow up observations of 100000 stars using the FLAMES multi-object spectrograph mounted on the 8.2m Very Large Telescope. FLAMES has two components with resolutions of 19000 and 47000, capable of observing 130 and 8 simultaneous targets, respectively. Combined with Gaia precision astrometry, Gaia-ESO will deliver accurate distances, 3D spatial distributions and abundances for at least 12 elements. Its top level science goals include understanding the formation and the evolution of open clusters and the thin disk, whilst also probing the structures of the halo disk and the origin of the thick disk.

Finally, the GALactic Archaeology with HERMES (GALAH) is the biggest spectroscopic survey under-way in the southern hemisphere. It is described in detail in the next section.

## 2.2 GALAH

GALactic Archaeology with HERMES (GALAH) is an ambitious spectroscopic survey being conducted on the 3.9m Anglo-Australian Telescope (AAT). This section provides

an overview of the survey.

### 2.2.1 Scientific goals

With a planned sample size of one million stars, GALAH is expected to recover approximately 30000 star formation sites and 50 giant clumps by chemical tagging (Bland-Hawthorn and Freeman (2004)). This is the primary goal of GALAH in galactic archaeology. Recovery of these sites will be facilitated by obtaining accurate chemical abundances for the following 29 species across all nucleosynthetic production channels-

Light elements- Li, C

Alpha elements- O, Mg, Si, Ca, Ti

Light odd-Z elements- Na, Al, K

Iron-peak elements- Sc, V, Cr, Mn, Fe, Ni, Co, Cu, Zn

s-process elements- Rb, Sr, Y, Zr, Ru, Ba, La

r-process elements- Ce, Nd, Eu

A preliminary group finding exercise is carried out by Mitschang et al. (2013), in which abundances from 291 stars from 30 clusters are tabulated from literature. The chemical difference between any two stars ( $i$  and  $j$ ) is defined as the sum of the Manhattan metric ( $\delta C$ ) between all chemical dimensions, shown in Equation 2.1.

$$\delta C = \sum_C^N \frac{|A_C^i - A_C^j|}{N} \quad (2.1)$$

Where  $C$  is a particular chemical species,  $N$  is the total number of species and  $A_C$  is the abundances of a species. The distributions of  $\delta C$  for stars from the same clusters and stars from different clusters are shown in Figure 2.2.

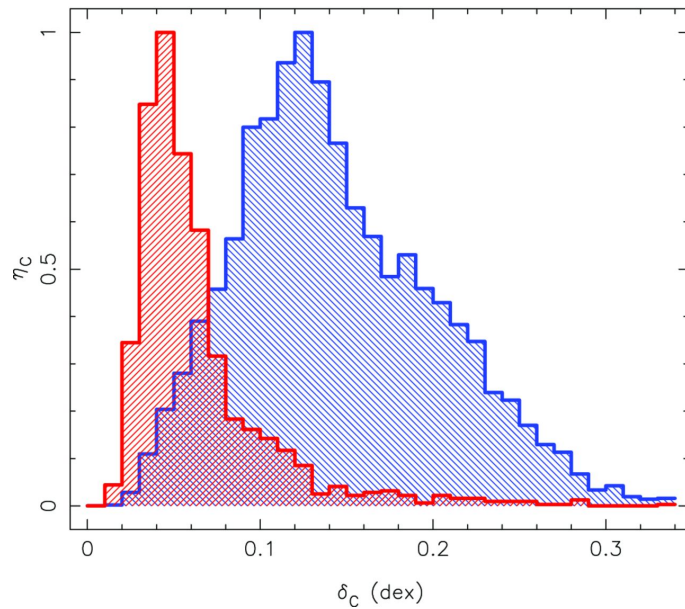


FIGURE 2.2: Distributions of  $\delta C$  for two populations of stars using eight elements. Figure taken from Mitschang et al. (2013).

Encouragingly, there are two distinct peaks in Figure 2.2, however a substantial overlap between the two populations is also evident. A subsequent probability function is defined to quantify the likelihood of any given two stars belonging to the same group. Mitschang et al. (2013) finds the efficiency of such a function is only 12% at the 90% confidence level.

It should also be noted that the effectiveness of chemical tagging does not simply rely on the number of elements studied. Many of the 29 GALAH elements share the same origins and vary together. Thus it is important to determine the number of independent dimensions of the GALAH chemical space. Ting et al. (2012) carried out a principle component analysis (PCA)<sup>2</sup> on a set of GALAH-similar spectra and found the number of independent dimensions to be between 7 and 9, depending on the nucleosynthetic processes dominating the given population.

These results show that it is extremely difficult for chemical tagging to accurately recover a large number of sites. Further more, new evidence suggests internal chemical inhomogeneities on the level of  $\sim 0.01$  dex in the cluster Hyades (Liu et al. (2015), in prep). It is unclear how universal these inhomogeneities are and how much impact this will have on chemical tagging. The large GALAH data set will be crucial in investigating these issues.

---

<sup>2</sup>As a side note, machine learning algorithms such as PCA reduces the dimensionality of the data yet retaining most of its information. The author speculates performing chemical tagging in the dimensionally reduced space could yield improved results compared to the native C-space.

In addition to its main goal of galactic archaeology, GALAH will produce a plethora of ancillary science. Two examples are described below.

GALAH mainly targets the disk. Its abundances will help to reconstruct its chemical evolution and to better constrain its age-metallicity-kinematic relation. Historically, the thick disk is not very well observed and its formation history remains unclear. GALAH has about 20% of its targets in the thick disk (Table 2.2). This gives GALAH unique opportunities in studying the thick disk and its formation. The bulk of the GALAH targets ( $\sim 80\%$ ) will be from the thin disk, a huge sample for characterising the thick and thin disk normalisation.

A number of metal rich stars are also expected to be found by GALAH. They can be used to understand the signatures of planet formation and the extent of radial migration.

### 2.2.2 Synergistic observations

In the era of modern survey, it is beneficial to have common targets between surveys for cross calibration and complementarity. GALAH is designed to work together with a number of on-going surveys to maximise the combined science output.

GALAH shares a number of targets with Gaia-ESO and APOGEE. This common sample will be used to cross calibrate the different analysis pipelines involved. This is particularly useful for checking the infrared parameters from APOGEE with the optical parameters from GALAH. Using this common sample, it is possible to place the surveys on a common footing, thus extending the parameter space coverage beyond a single survey.

On top of ground based Gaia-ESO and APOGEE, the CoRoT (Baglin et al. (2006)) and Kepler 2 (K2) (Borucki et al. (2010)) missions will provide GALAH with accurate asteroseismological parameters (e.g., stellar radii, surface gravities and masses) for a portion of stars. Combining these parameters with GALAH spectroscopically derived temperature and metallicity, it is possible to obtain accurate stellar ages. This overlap is especially significant for K2, as GALAH will observe 40000 K2 stars across all galactic components.

Finally, the most significant contribution comes from Gaia (Lindegren et al. (2008)). From 2017, Gaia will provide precise astrometry for *all* GALAH stars. At its best, the Gaia parallaxes and proper motions will have uncertainties of approximately  $25\mu\text{as}$  and  $25\mu\text{as yr}^{-1}$ , corresponding to  $1\text{kpc}$  and  $1\text{kpc yr}^{-1}$  in distance and transverse motion uncertainties. Together with GALAH radial velocity (see Chapter 3 for a detailed discussion), 3D velocity

maps can be constructed for the whole GALAH data set. Gaia will also provide accurate absolute magnitude and astrometric surface gravities.

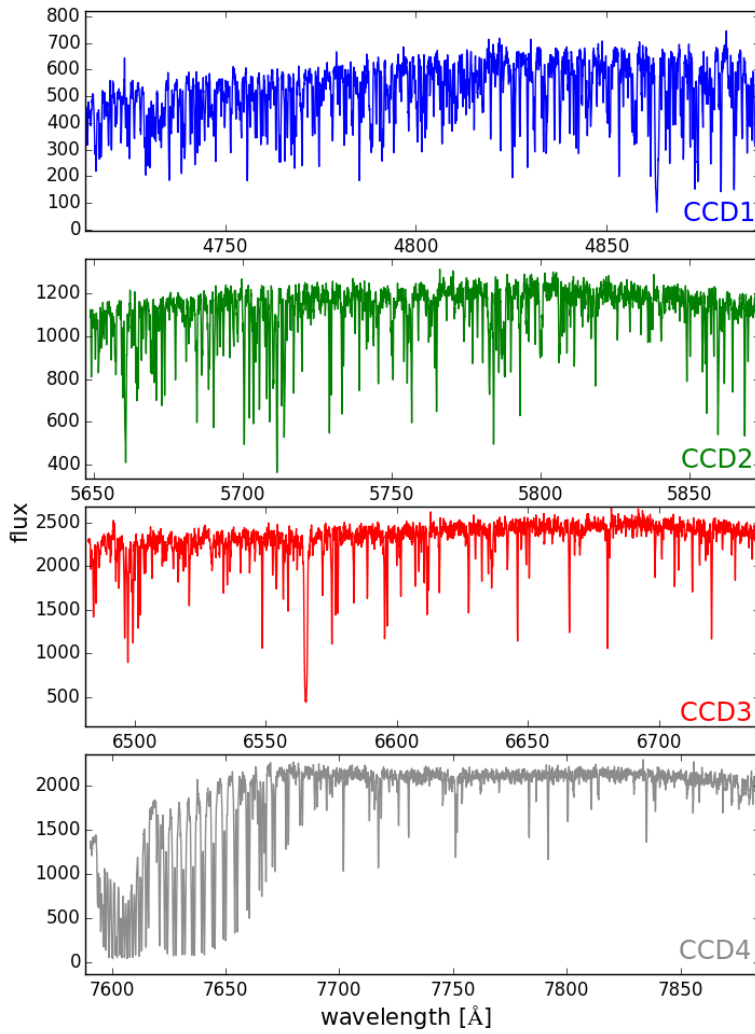
### 2.2.3 Instrument

The High Efficiency and Resolution Multi-Element Spectrograph (HERMES, Heijmans et al. (2012)) is the primary instrument of GALAH. It has four  $4 \times 4\text{K}$  E2V CCDs targeting four non-overlapping wavelength windows (Table 2.1), with a total spectral coverage of approximately  $1000\text{\AA}$ . These wavelength ranges are selected for maximising the number of spectral features for chemical tagging. HERMES is capable of simultaneously acquiring spectra of 392 targets in a  $2^{\circ}2$  field of view, using the existing 2dF positioner on the AAT.

Two resolution modes are available-  $R \sim 28000$  and 50000. The high resolution mode is achieved using a slit mask, resulting in a 50% light loss. Figure 2.3 shows a spectrum taken by HERMES.

TABLE 2.1: HERMES wavelength windows.

CCD	colour	wavelength ( $\text{\AA}$ )
1	blue	4718 - 4913
2	green	5649 - 5873
3	red	6481 - 6739
4	NIR	7590 - 789

FIGURE 2.3: A spectrum observed by HERMES at  $R \sim 28000$ .

#### 2.2.4 Survey strategies

The current goal for GALAH is to observe 400000 stars by 2018, with the ultimate goal of observing one million stars. All stars will be observed at  $R \sim 28000$ . The targets are magnitude limited between  $V=12$  and 14, and target selection is done based on 2MASS (Skrutskie et al. (2006)) JHK photometry according to Equation 2.2. The target fields are restricted to have galactic latitude greater than  $10^\circ$  and declination between  $-80^\circ$  and  $+10^\circ$ . The cut on galactic latitude is mainly due to the amount of extinction at lower latitudes.

$$V(J, K) = K + 2(J - K + 0.14) + 0.382e^{2(J-K-0.2)} \quad (2.2)$$

With 2dF's capacity of simultaneously observing 392 stars, GALAH fields are chosen to have target densities greater than 400 per  $2^{\circ}2$  field. In total, 4303 fields are prepared for GALAH. 3300 fields out of which need to be observed to fulfil the goal of one million stars. Figure 2.4 illustrates the distribution of GALAH fields on the sky. Table 2.2 summaries the expected contribution of different galactic components to the GALAH sample based on Galaxia models (Sharma et al. (2011)).

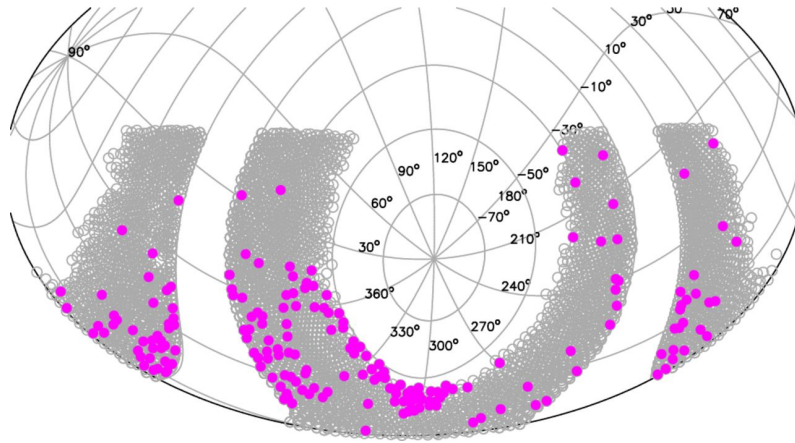


FIGURE 2.4: Distribution of the GALAH fields in the sky. The grey circles represent planned fields, whereas the purple circles represent the fields already been observed as of Nov 2014. Figure taken from De Silva et al. (2015).

TABLE 2.2: Expected contribution of different galactic components to the GALAH sample.

component	dwarf (%)	giant (%)
thin disk	57.87	18.56
thick disk	4.63	17.82
halo	0.05	1.02
bulge	0	0.05

GALAH requires a minimum signal to noise ratio (SNR) of 100 per resolution element. To achieve this, each field will be exposed three times consecutively. For seeing under  $2''$ , the individual exposure time is 20 minutes. Additional 20 and 60 minutes are given in total if the seeing is greater than  $2''$  and  $2.5''$ , respectively. No observations will be carried out for seeing greater than  $3''$ .

GALAH has started observing at the end of 2013. As of Apr 2015, approximately 120000 stars have already been observed. The first internal data release will occur in July 2015.

### 2.2.5 Data flow

Similar to Gaia-ESO, GALAH has multiple parallel analysis pipelines, with the rationale being the complementarity of different approaches. Figure 2.5 is a flow chart illustrating the different steps involved in data analysis.

Currently there are three data reduction pipelines- IRAF (an IRAF based pipeline written by Kos et al.), 2dfdr (also known as the GALAH Analysis Pipeline, GAP. An existing reduction pipeline from the Australian Astronomical Observatory) and HerPy (a Python based pipeline written by Ireland et al.). All three pipelines are undergoing quality tests and the collaboration will eventually settle down to one. A detailed comparison between these procedures are presented in Chapter 3, Section 3.4.

There are two initial parameter estimation algorithms- GUESS (a global fitting script developed for this project, described in detail in Chapters 3 and 4.) and photometry.

The initial parameter estimations will be fed into four stellar parameters pipelines-

- SME (Spectroscopy Made Easy, Valenti and Piskunov (1996), adapted by K. Lind et al. for GALAH)

SME is an IDL based code which derives stellar parameters from excitation/ionisation equilibrium. It is also capable of deriving elemental abundances, radial, turbulent and rotational velocities. The original SME assumes plane parallel LTE atmosphere models, but a NLET Fe grid has been implemented since. Presently, SME is a highly successful node in Gaia-ESO.

- Theremin (Wylie de Boer et al.)

Theremin derives stellar parameters from excitation/ionisation equilibrium of Fe and Ti lines. A detailed discussion on Theremin is presented in Chapter 4, Section 4.2.3.

- Oracle (Casey et al.)

Oracle is a generative solver which optimises all available parameters, including all elemental abundances, simultaneously.  $T_{\text{eff}}$  and  $\log g$  are derived from Fe and Ti excitation/ionisation balance, with constraints from hydrogen wings and asteroseismology priors. All uncertainties are well characterised by Markov chain Monte Carlo. Efforts are being made towards implementing <3D> and NLTE corrections.

- The Cannon (Ness et al. (2015))

The Cannon is a data driven stellar parameter pipeline. It relies on a set of training spectra with well defined parameters. The algorithm fits a flexible model to the set at each wavelength. This model is then used to derive the stellar parameters for the unknown stars. The Cannon is remarkable because it is completely independent of synthetic models and line lists, but entirely dependent on the training set. In GALAH, such a set will be constructed using SME, Theremin and Oracle, achieving accurate parameters which span and populate the parameter ranges.

The parameters obtained from the four pipelines will then be homogenised and fed into the three abundance pipelines- SME, Theremin and Oracle. The resulting abundances will again be homogenised to derive the final abundances for data release.

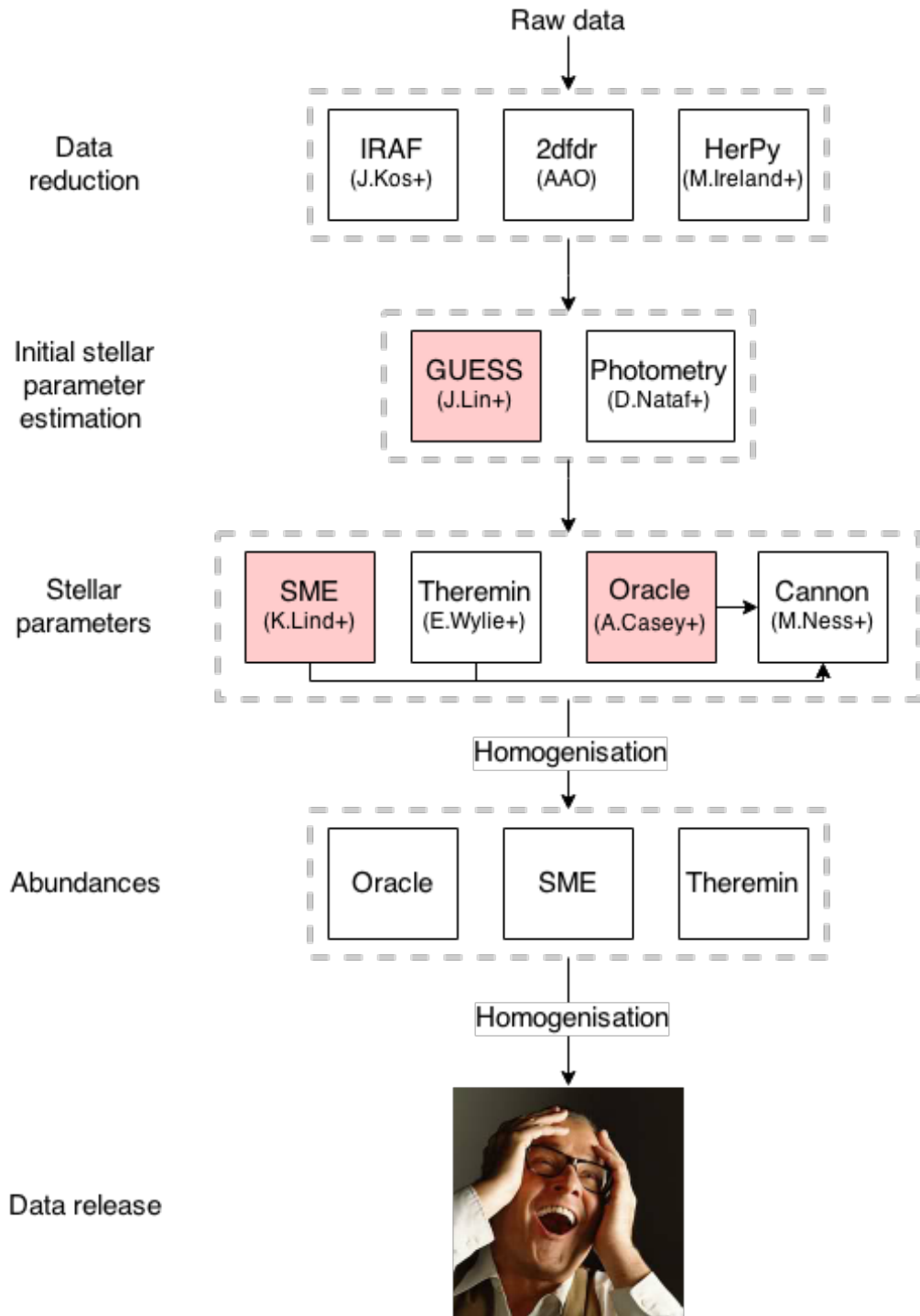


FIGURE 2.5: Flow chart of the GALAH data analysis procedure. The author is involved in the steps highlighted in pink.

## Chapter 3

# GUESS I- Radial Velocity

RADIAL velocity (RV) correction is an important first step in the spectroscopic analysis of GALAH spectra. In other large scale surveys, RV is often determined using multiple methods. For example, in the SEGUE Stellar Parameter Pipeline (Lee et al. (2008)), the spectra are firstly cross correlated with a template of SDSS spectra to produce an initial estimate. These values are then refined by finding the best-match RV template in the external ELODIE library (Prugniel et al. (2007)), which contains high resolution, high precision RV spectra of more than a thousand stars. If both methods fail, there is a third method which finds RV based on the shifts in specific spectral features. As GALAH is still in its early stages, only one method of measuring RV has been implemented, as a part of GAP (GALAH Analysis Pipeline). For this project, a separate RV code, GUESS, is written for GAP reduced, extracted 1D spectra. This chapter will provide a description of GUESS and comparison of results with GAP and APOGEE.

### 3.1 GUESS (Part I)

*'The Inner Machinations of my mind are an enigma.'*- Patrick Star

The GALAH Ultra Enigmatic Spectroscopic Script (GUESS) is an independent pipeline written for this project. It consists of two parts- RV correction and initial stellar parameter estimation. This chapter discusses the RV aspect and Chapter 4 discusses the parameter aspect. The GAP reduced data is chosen as it is the largest available data set in GALAH at the time of this writing.

In GUESS, raw RV is calculated by cross correlating the spectra with a template of synthetic spectra. The steps involved are described in detail in this section. Only three out of four arms are used in calculating RV. The infrared arm is ignored because it has fewer lines for cross correlation and its wavelength solution is imperfect.

### 3.1.1 SNR cut

The first step is to apply a signal to noise ratio (SNR) cut to the GAP reduced spectra. This is done mainly because GAP does not distinguish between non-science and science fibres and extracts all to the same directory. Thus the SNR cut is being used as an easy way to weed out these non-science fibres and otherwise unusable data.

Calculating signal in a spectrum usually requires definition of the continuum level. However it is problematic here because the continuum regions are in rest wavelengths. Instead, the median of the spectrum is adopted as the signal because it is most robust (not prone to outliers like the mean) and simple to calculate.

Noise is usually defined as the standard deviation of the spectrum, in the absence of spectral features (i.e. in the continuum regions). Over the whole spectrum, it can be approximated using its median absolute deviation (MAD). Intuitively one can consider it as the difference between successive pixels. For a normally distributed variable  $x$ , its SNR is calculated as:

$$\text{SNR} = \frac{1.4826}{\sqrt{2}} \text{ median}(|x_{i+1} - x_i|) \quad (3.1)$$

Where  $i$  is the index of one pixel. This method provides a simple and robust way for an initial SNR estimation. Figure 3.1 compares the SNR distribution of 2000 stars obtained via MAD, native GAP and median. The native GAP SNR values are the variances from 2dfdr. The median method is calculated ad hoc by firstly shifting the spectra to rest, then finding the median of the continuum regions (signal) and dividing by the standard deviation of the region (noise). MAD is found to underestimate SNR when compared to the more conventional methods at high SNRs.

Despite this difference, MAD is sufficient for the purpose of weeding out non-science spectra. Figure 3.2 shows the SNR distribution for 90000 stars. A SNR cut at 3 is adopted to exclude the peak near 0 corresponding to non-science spectra.

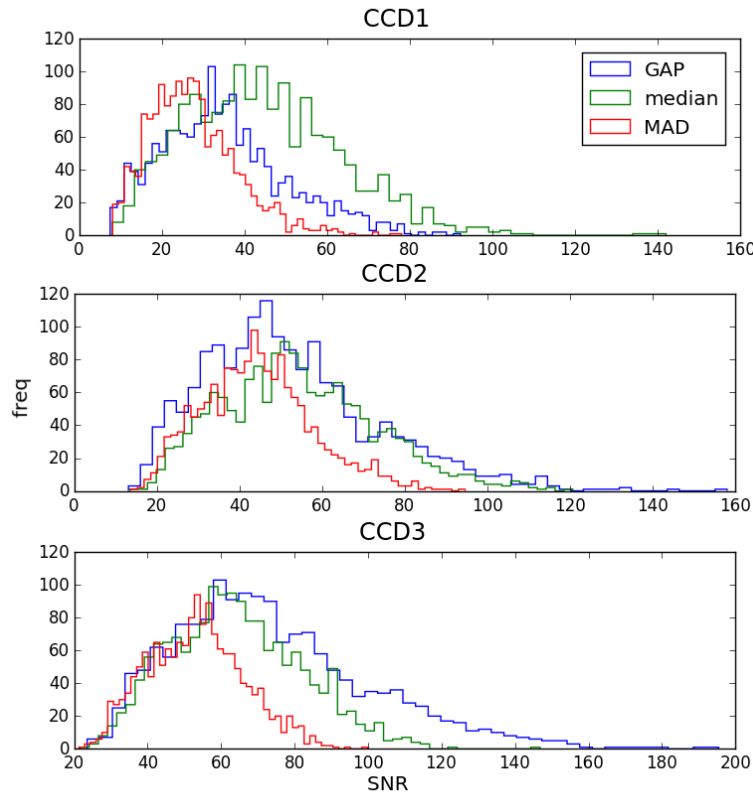


FIGURE 3.1: Comparison of SNR derived from three different methods for 2000 stars- GAP (blue), median (green) and MAD (red). The three methods agree reasonably well at the low SNR end for CCD2 and 3. However MAD appears to underestimate SNR for all CCDs.

### 3.1.2 Median filter and continuum normalisation

In the next step, GUESS applies a median filter to the spectra and performs continuum normalisation. The median filter is in place to remove any remaining cosmic rays present after data reduction. For every 5 pixel window, if any pixel lies five standard deviations beyond the median of the window, it is replaced by the median. This way, only extremely thin spikes (i.e. cosmic rays) are affected. Figure 3.3 shows the comparison between a raw and median filtered spectrum.

The spectra are then continuum normalised. CCD1 and CCD3 have very smooth continua, they are fitted with the univariate splines, using the Python function `scipy.interpolate.UnivariateSpline`. The only parameter in this fit is the smoothing factor `s`, which determines how smooth the function is. For CCD1 and 3, a smoothing factor of `s=1e15` is found to be optimal. To prevent the fit being skewed by major hydrogen features,

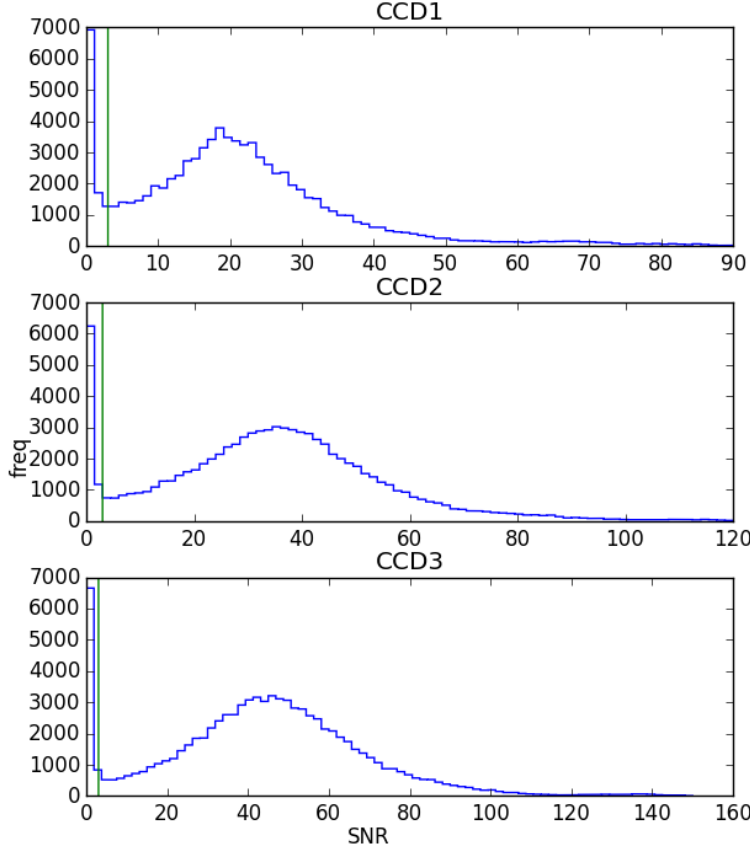


FIGURE 3.2: SNR distribution of 90000 stars reduced by GAP. CCD1 (blue) has artificially low SNR than the other two arms (green and red) because presence of large spectral features in its wavelength range. The green line denotes the SNR cut at 3, excluding the unusable data.

$H_\alpha$  (4847-4900Å) and  $H_\beta$  (6530-6592Å) regions are excluded from the fit (shown by the dashed lines in Figure 3.4).

For CCD2, the 1D spectra extraction step in GAP is performed poorly and resulted in a very wavy shape. It is best fitted by a 4th order polynomial. Figure 3.4 shows an example of normalised spectrum.

### 3.1.3 Cross Correlation

Finally, the data spectrum is cross correlated with a template of synthetic AMBRE spectra (de Laverny et al. (2012)). The AMBRE spectra are computed using MARCS model atmospheres (Gustafsson et al. (2008)) and Turbospectrum radiative transfer code. GUESS

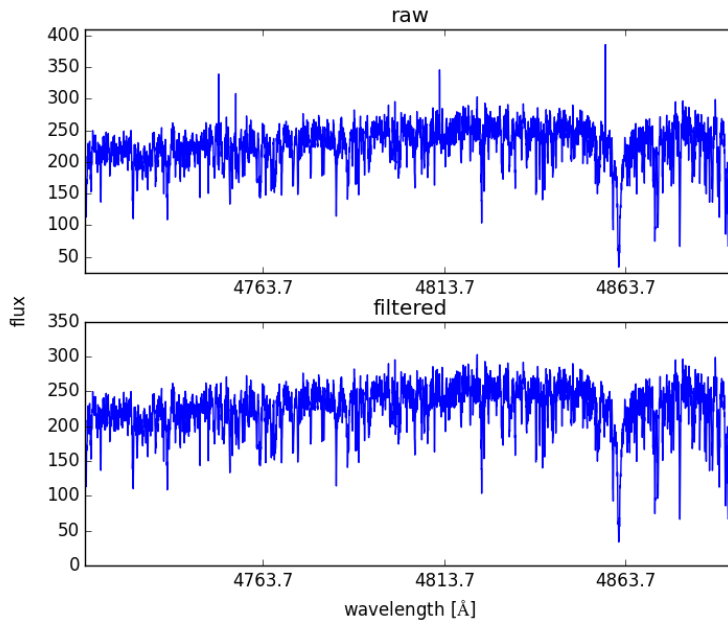


FIGURE 3.3: Comparison between raw (upper panel) and median filtered (bottom panel) spectrum in the blue arm (CCD1). Note the absence of cosmic rays in the filtered spectrum. The spectral features have not been altered.

uses a gird of 15 model spectra (see Figure 3.5 ). They range from 4000-7500 K in temperature, with constant  $\log g$  at  $4.5 \text{ cm s}^{-2}$  and alpha enrichment at 0 dex.

The goodness of the cross correlation is calculated by the cross correlation coefficient  $c_k$ -

$$c_k = \sum_i (f_i \ g_{i+k}) \quad (3.2)$$

Where  $f$  and  $g$  are both functions in the cross correlation.  $c_k$  can be normalised such that at the right shift  $k$ ,  $c_k = 1$ -

$$c_k = \frac{\sum_i (f_i \ g_{i+k})}{\sqrt{\sum_i (f_i^2) \sum_i (g_i^2)}} \quad (3.3)$$

The Python function `numpy.correlate` used for correlation pads the empty pixels by zeroes. This means the spectra are approximately two top hat functions, with the resulting cross correlation dominated by their rectangular shapes, shown by Figure 3.6. To remove this artefact and make the peak cross correlation more defined, both data and model spectra are moved down to the zero level by subtracting their individual means. Both spectra are also normalised according to Equation 3.3.

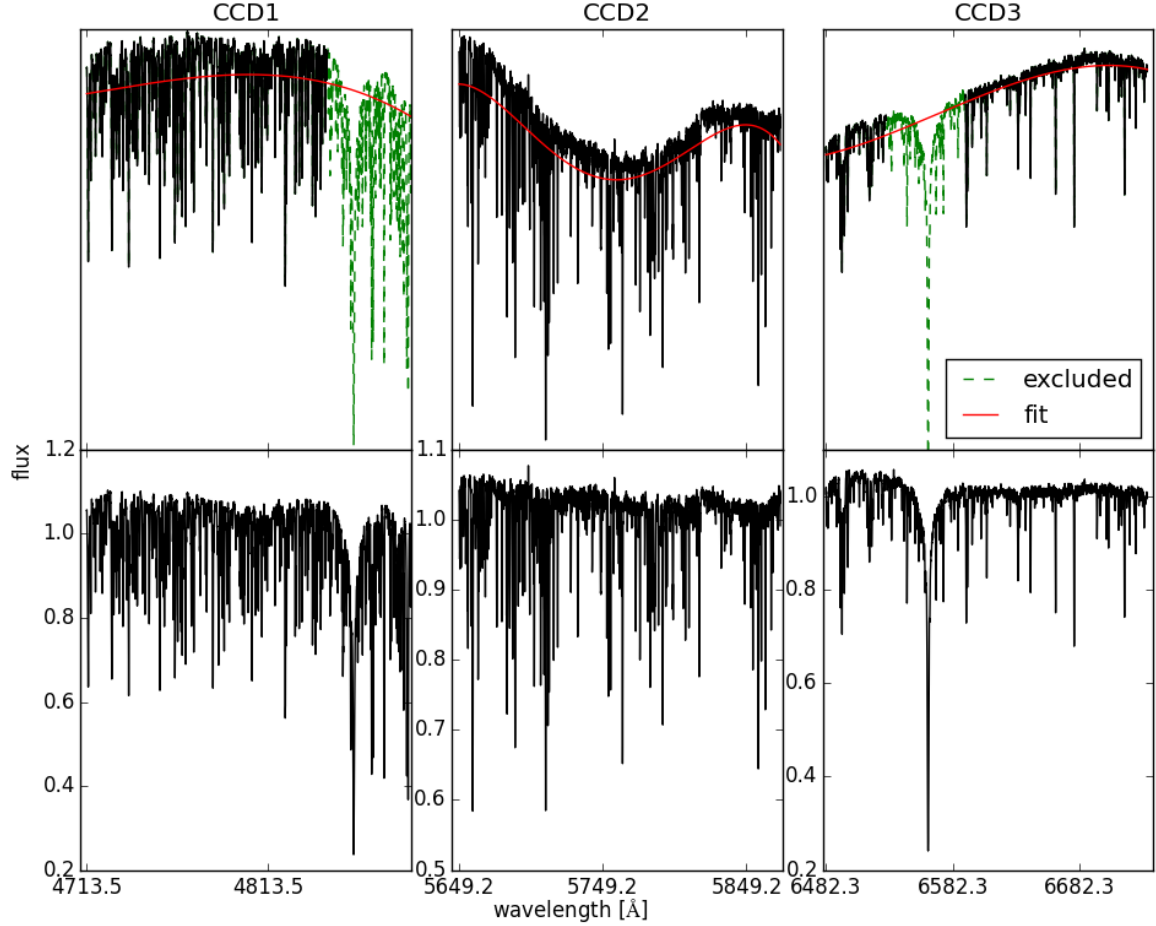


FIGURE 3.4: Upper panel: An example of the unnormalised spectrum of a star. Bottom panel: normalised spectrum. The dashed regions are excluded from the fit (red line).

Both the model and data spectra are then multiplied by a window function. The window function consists of two ramps which covers 10% of the spectrum on either side (see Figure 3.7). This again softens the edges of the spectra to reduce the noise in the cross correlation peak.

For each CCD, the data spectrum is individually cross correlated with the grid of 15 model spectra. The cross correlation peak is fitted with a polynomial and its maximum is taken as the coefficient value. A cross correlation is considered to be good if the normalised cross correlation coefficient is greater than 0.3. This number is chosen to be the cut-off because it is found that the lower temperature models often give out ‘false peaks’ of height  $\sim 0.25$ .

The final RV for the CCD is a coefficient weighted average of the good RVs. A star is

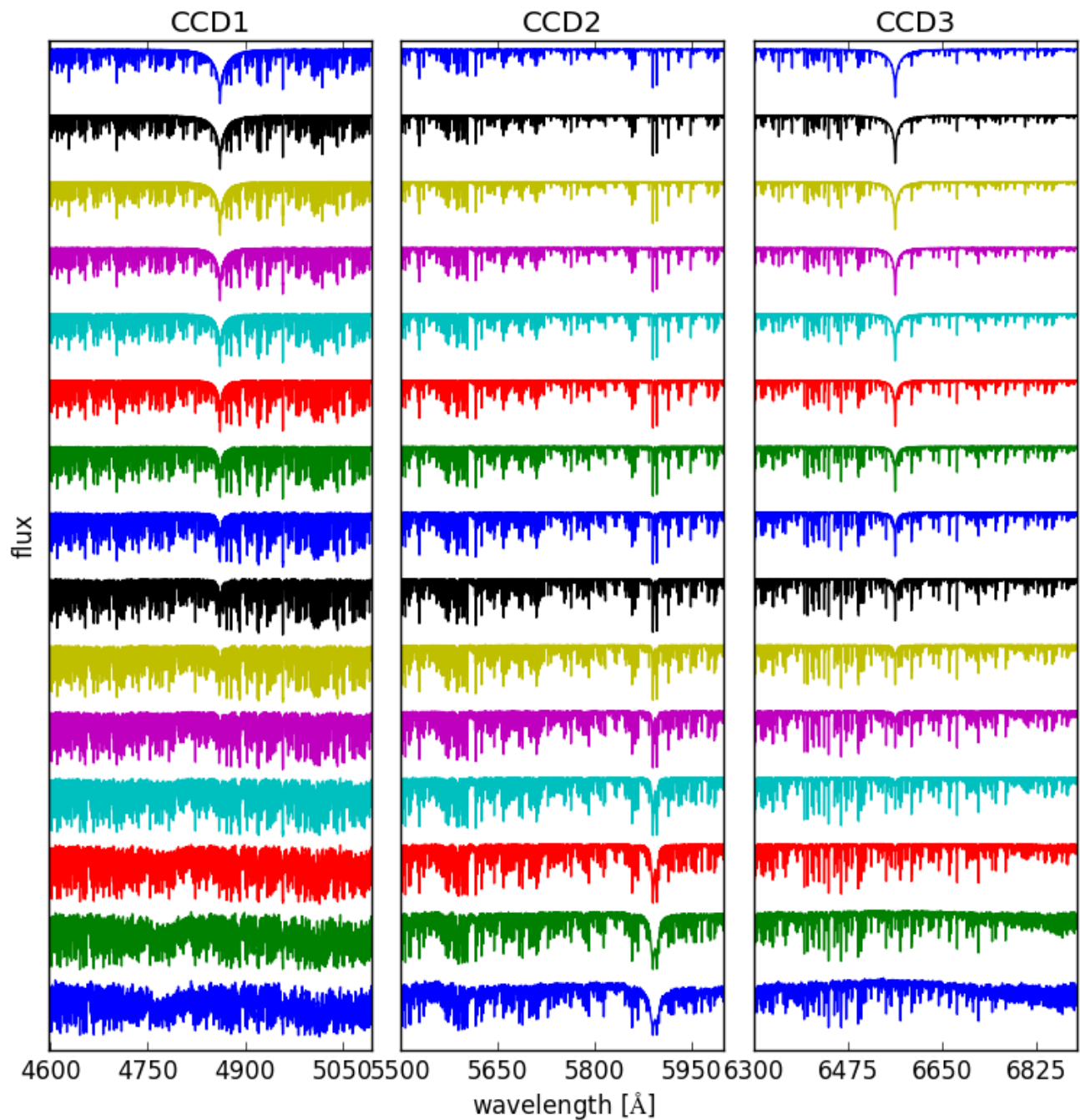


FIGURE 3.5: 15 AMBRE model spectra used for cross correlation, in descending temperature from the top down. The temperature ranges from 4000-7000 K, with 250 K intervals.

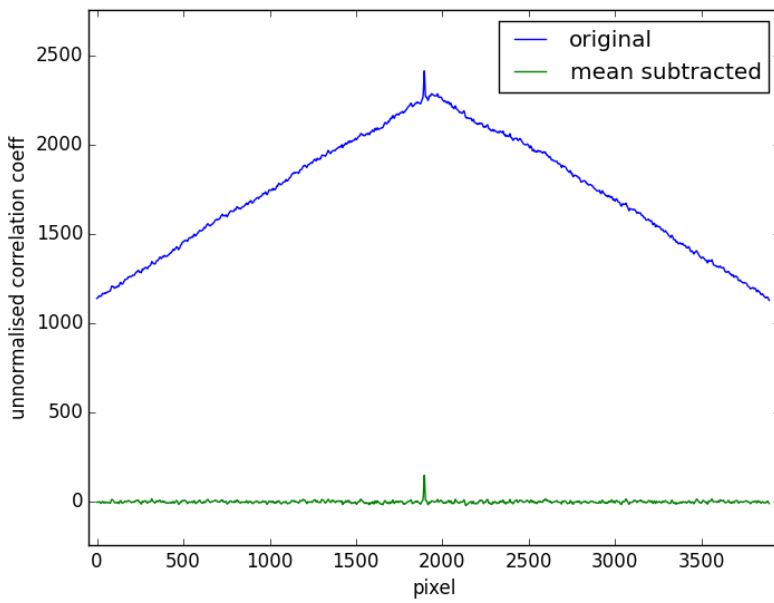


FIGURE 3.6: Comparison of the cross correlation peaks of the original spectra (top) and mean subtracted spectra (bottom). The triangle artefact present at the top is due to the continua being at 1. If the cross correlation peak is not well defined, it is possible to mistake the peak of the triangle as the peak of the cross correlation. This problem is circumvented by reducing the continua down to zero, as shown on the bottom plot.

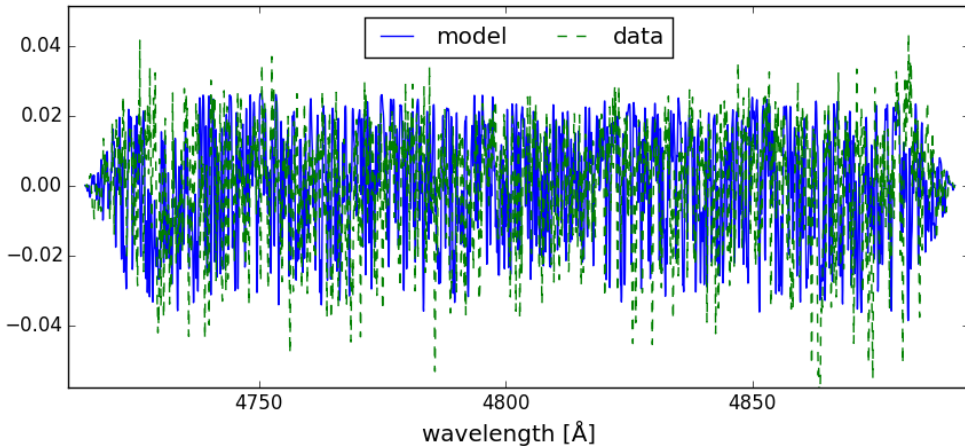


FIGURE 3.7: Mean subtracted, windowed spectra ready to cross correlate.

flagged as having ‘bad weights’ if all 15 coefficients are below 0.3 for one or more CCDs. Figure 3.8 shows an example of a badly weighted CCD. It is found that the green arm (CCD2) is most problematic in this aspect (see the detailed discussion in Section 3.4).

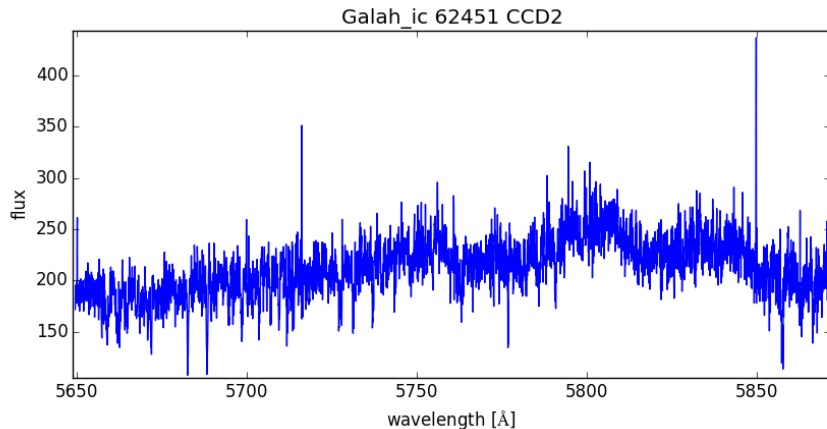


FIGURE 3.8: Raw spectrum of a badly weighted CCD. This specific CCD is flagged because the wiggles in the continuum making normalisation and cross correlation difficult.

Finally, the final velocity of the star is the average of the three CCDs. For stars with unusually large velocity scatter- one CCD having a RV which lies more than 2 times further away from the other two, it is excluded from the final average (e.g., if the RVs are 1km/s, 1.2km/s and 5km/s for CCDs 1, 2 and 3, then CCD 3 is excluded). The CCDs which have ‘bad weights’ are also excluded from the final RV.

### 3.1.4 Uncertainties

There are multiple sources of uncertainties in the derived RV values. They range from instrumental (e.g., pixel to pixel variations, read out noises) to algorithmic (e.g., cross correlation). However, the dominant source of uncertainty which dwarfs all these factors is from the RV dispersion between three CCDs. Thus GUESS adopts  $\sigma(\text{RV})$  as the error on the final velocities. For most stars,  $\sigma(\text{RV})$  is smaller than 1 km/s, as shown in Figure 3.9, bottom panel.

## 3.2 Comparison with GAP and APOGEE

In this section, the results from GUESS are compared with GAP and APOGEE. In GAP, radial velocities are calculated by the IRAF function `fxcor` which performs Fourier cross correlation with the asteroid Ceres, a spectral standard. Figure 3.9 shows RVs of a sample set of  $\sim 70000$  stars.

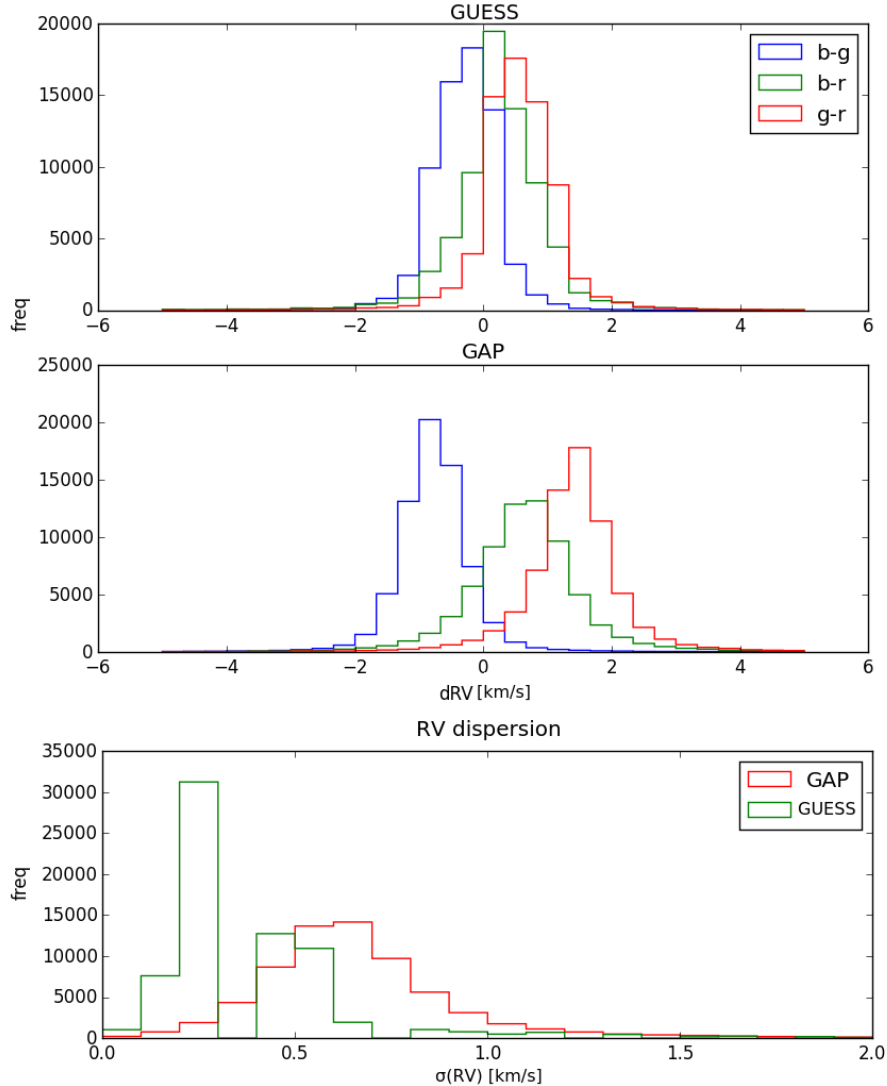


FIGURE 3.9: Top and middle panels: difference in RVs between three CCDs (blue-green, blue-red, green-red) for GUESS and GAP, respectively. Bottom panel: standard deviation distribution between the three CCDs for both sets of RVs.

Ideally, all three histograms in Figure 3.9's top two panels should peak at zero, as there should not be any systematic RV offsets across the CCDs. However both GUESS and GAP results show non-zero offsets. On average, GUESS produces offsets smaller than 1km/s whereas GAP's offsets are roughly 1.5km/s. The green CCD (CCD2) again is the most problematic, as both blue-green and green-red peaks are more off center than blue-red. This systematic offset could be an indication of wavelength calibration problems within the GAP reduction procedure. Figure 3.9's bottom panel shows the dispersion (measured as the standard deviation) between three CCDs. Again GUESS outperforms

GAP in producing more consistent RVs, with its histogram peaking sharply at 0.3km/s and GAP's peaking at 0.7km/s with a substantial tail.

Both GUESS and GAP results are compared with APOGEE, using a sample of  $\sim 40$  stars (The APOGEE RVs and parameters are provided by K. Schlesinger). The APOGEE RVs are determined by multiple cross correlations with best match templates. From the results shown in Figure 3.10, it can be concluded that GUESS is performing marginally better in terms of agreement with APOGEE and again is producing more consistent RVs.

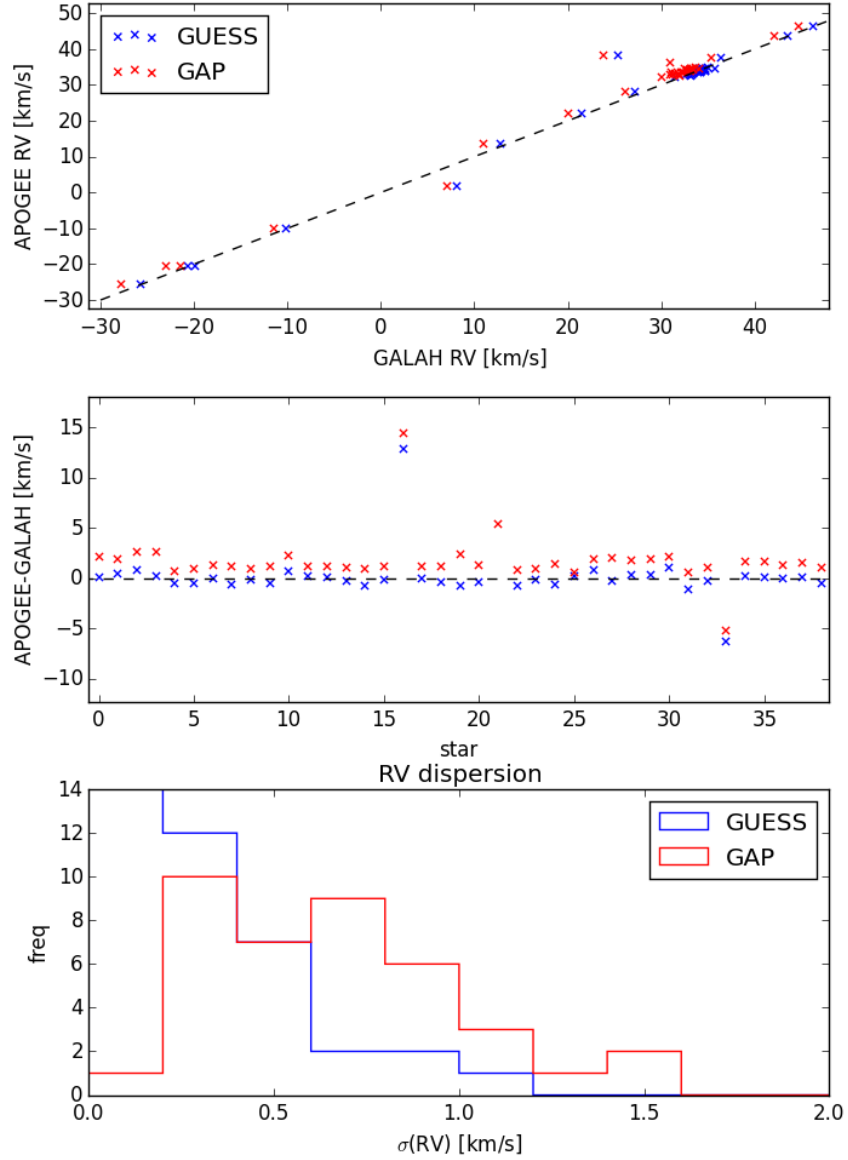


FIGURE 3.10: Top panel: one to one comparison of GALAH (blue-GUESS, red-GAP) vs APOGEE RV values. Middle panel: RV differences between the two surveys (note the 21st star is missing from GUESS as it was flagged as having bad weights). Bottom panel: velocity dispersions of GAP and GUESS relative to APOGEE.

### 3.3 Clusters

In this section, stars from M67 and 47Tuc are analysed using GUESS. The observations are extracted from the GAP database and heliocentric corrected by K. Schlesinger.

### 3.3.1 M67

1062 stars from M67 are processed through GUESS. The average heliocentric corrected RV is found to be 33.8 km/s, with a standard deviation of 20.1 km/s. Girard et al. (1989) found M67 velocity to be 33.6 km/s. The velocity distribution of the 1062 stars is plotted in Figure 3.11. Judging from the plot, the peak of the distribution coincides with literature value, however the standard deviation is quite large due to its long tail.

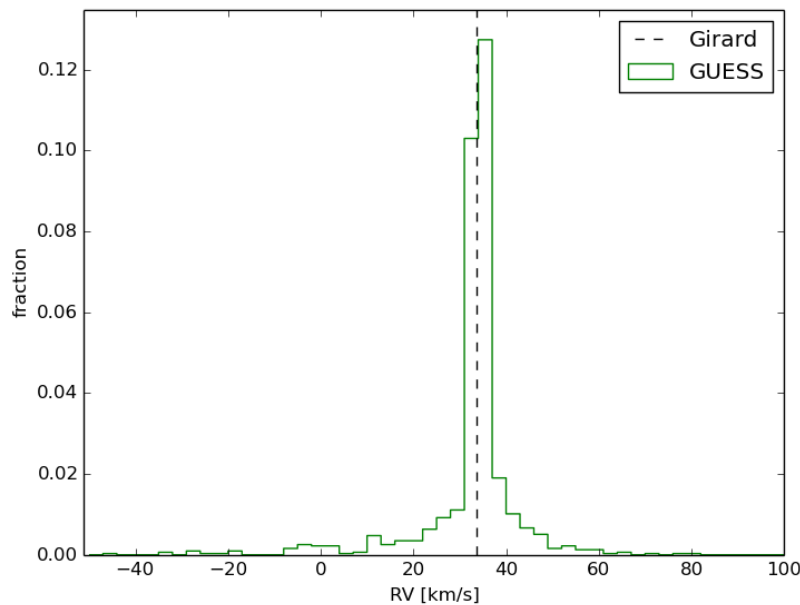


FIGURE 3.11: Velocity distribution of 1062 M67 stars. The literature value of Girard et al. (1989) is represented by the dashed line.

### 3.3.2 47Tuc

1134 stars from 47Tuc are processed through GUESS. The average heliocentric corrected RV is found to be -17.2 km/s, with a standard deviation of 6.84 km/s. The velocity distribution is plotted in Figure 3.12. As a comparison, RVs of 174 stars from AAOmega<sup>1</sup> are also shown in Figure 3.12. They have an average of -17.14 km/s and a standard deviation of 6.9 km/s. Harris (1996) found the mean velocity of 47Tuc to be -18 km/s.

<sup>1</sup>A separate spectrograph also mounted on the AAT.

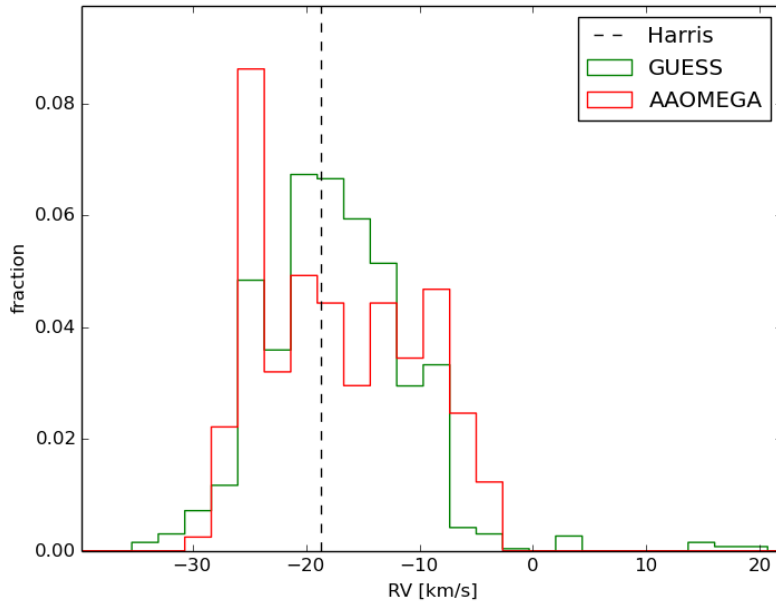


FIGURE 3.12: RV distributions of 1134 47Tuc stars from GUESS (green), 174 stars from AAOmega (red) and Harris (dashed line). Both distributions coincide with each other, with GUESS appearing more Gaussian like with its peak at literature value.

### 3.4 Comparison of Multiple Reductions

The official GALAH reduction pipeline GAP is wrapper of 2dfdr, an existing data reduction software for multi-fibre spectroscopic data. In rough terms, the data reduction process contains three steps. Firstly, individual fibre profile and centre are identified from a quartz-halogen flat field. Each fibre is then extracted into 1D format and sky subtracted. Finally wavelength calibration is performed using a Thorium-Xenon arc lamp.

From testing GUESS on GAP reduced data, it is found that a number of stars have continuum wiggles in their green arm (for example, Figure 3.8). This apparently is a persistent issue within 2dfdr. In addition to this, the wavelength calibration is also not perfect, as shown by the non-zero offsets in Figure 3.9. These two issues, coupled with other factors such as the non-transparent nature of 2dfdr motivated the construction of two additional reduction pipelines:

- IRAF- an IRAF pipeline written by J. Kos. It follows the same general steps as GAP, but with built-in IRAF functions.

- HerPy- a Python based pipeline written by M. Ireland, with the main aim to be transparent and simple.

Figure 3.13 shows an example of a star successfully reduced by all three pipelines. Figure 3.14 shows a star which has wiggles in the GAP reduced version but is successfully reduced in HerPy and IRAF.

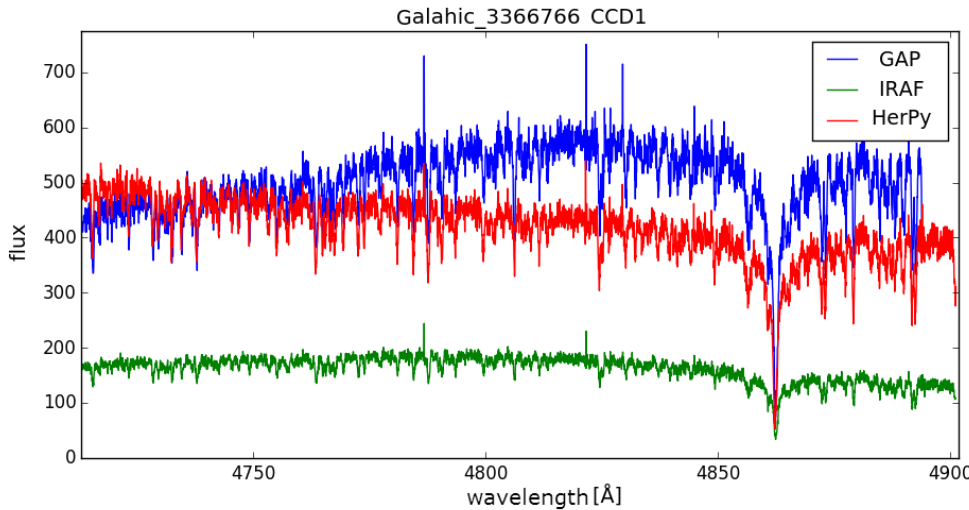


FIGURE 3.13: CCD1 of a star which has been successfully reduced by all three pipelines. Note the HerPy spectrum has already been heliocentrically corrected hence  $H_{\beta}$  is at a slightly different wavelength.

Both IRAF and HerPy are under construction. In fact at the time of this writing, HerPy has only reduced 2 GALAH fields. But even from this limited sample, it is apparent that HerPy does not have the continuum wiggle issue (which plagues about 10% of GAP stars in the same sample).

SNR from the three pipelines are also different. Figure 3.15 shows the MAD SNR distributions of a common set of 335 stars from the three pipelines. GAP and IRAF have similar SNR distributions, with GAP having slightly higher values for CCD2 and 3. HerPy outperforms both GAP and IRAF by a significant amount.

Personally, the author thinks HerPy is the ideal reduction pipeline for GALAH, as it is free from continuum wiggles and produces the highest SNR out of the three pipelines. Testing its wavelength solution will be the next important step.

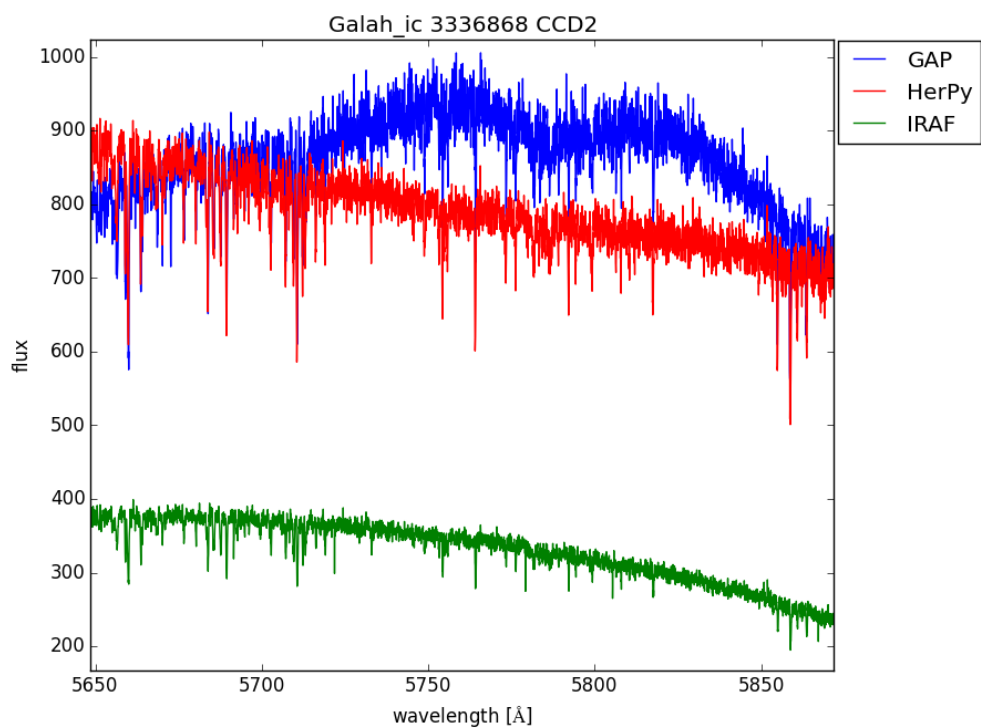


FIGURE 3.14: Comparison of a star successfully reduced by Herpy and IRAF but has continuum wiggles in GAP.

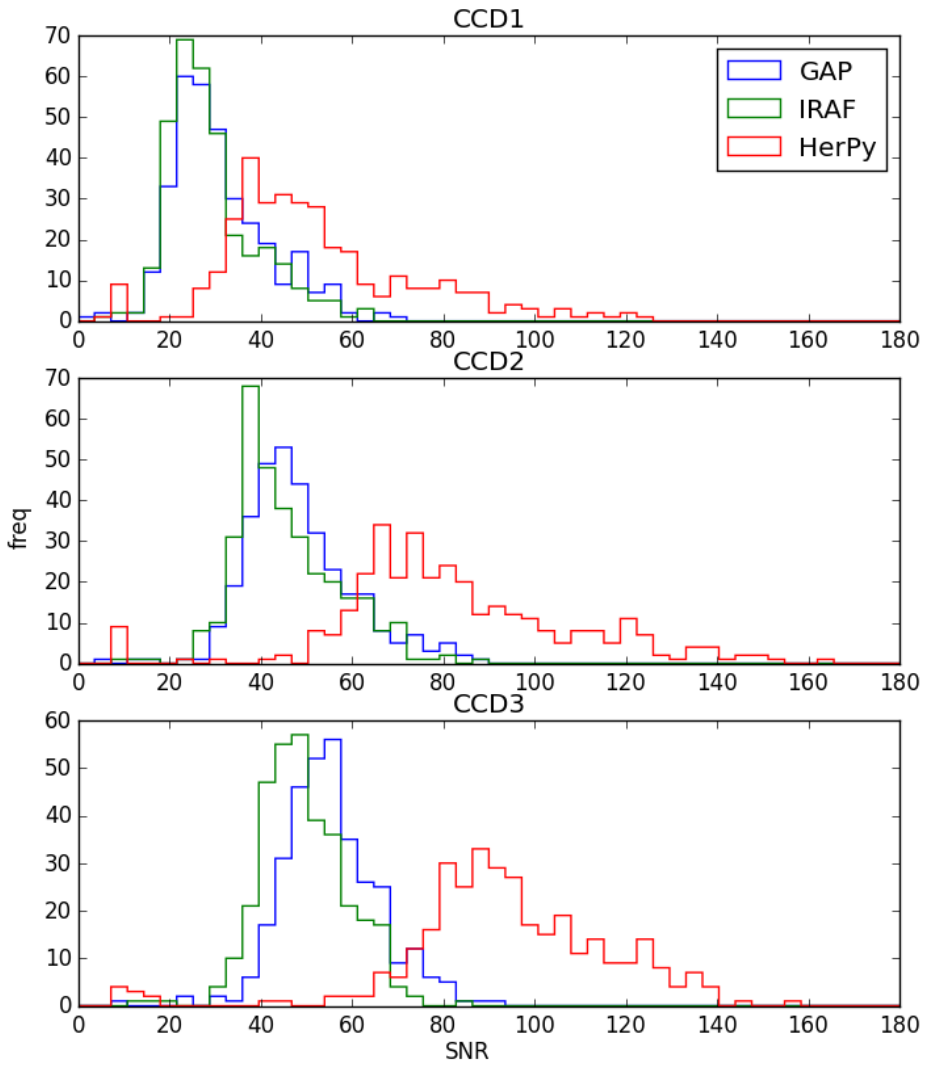


FIGURE 3.15: SNR distributions of 335 stars from GAP (blue), IRAF (green) and HerPy (red). SNR values are derived using the MAD method.

## Chapter 4

# GUESS II- Parameter Estimation

MOST traditional abundance analysis pipelines determine atmospheric parameters iteratively. Depending on the algorithm and the number of iterations, process time for an individual star ranges from seconds to minutes (for example on a Mac book, Theremin takes few minutes to converge based on a decent set of initial parameters). Figure 4.1 shows the number of iterations required for convergence as a function of initial temperature guesses for the star 18Sco, running on an earlier version of Oracle.

In Figure 4.1, around the accepted  $T_{\text{eff}}$  value for 18Sco (5810K), the number of iterations required for convergence decreases visibly. Thus it is possible to minimise computation time by supplying the analysis pipeline with an accurate initial guess of parameters. For 18Sco, a temperature guess at roughly  $\pm 250\text{K}$  around 5810K will be sufficient to reduce the iteration number by 4. Although this number seems insignificant for a single star, it can be a non-trivial improvement for the one million stars GALAH will observe.

In this chapter, the second part of GUESS which provides initial parameter estimations of  $T_{\text{eff}}$ ,  $\log g$  and [Fe/H] is described.

### 4.1 GUESS (Part II)

The second part of GUESS provides a first estimate of stellar parameters by global model fit. In this section, two methods of obtaining parameters- simplex and nearest neighbor are tested and compared. Both methods are partially inspired by the local linear embedding algorithm (Roweis and Saul (2000)), a detailed discussion and its applicability in GALAH are presented in Chapter 5).

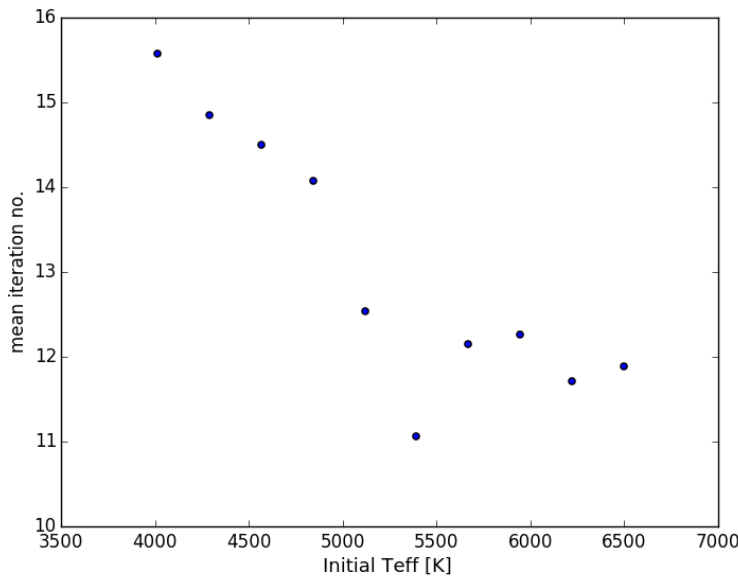


FIGURE 4.1: Plot of mean number of iterations against starting temperature guesses for 100 runs of 18Sco on Oracle. The initial temperature guesses are binned into 10 bins and the average number of iterations for each bin is calculated. There is a visible decrease in iterations around the neighborhood of accepted  $T_{\text{eff}}$  value of 5810K for 18Sco. Although the lowest number of iterations occurs at around 5250K.

#### 4.1.1 Continuum normalisation

For every star, the RV component of GUESS outputs a RV value and three RV corrected, median filtered spectra (for the three CCDs). The parameter component of GUESS fits each CCD individually. A list of 88 continuum regions (17 for CCD1, 36 for CCD2 and 35 for CCD3) are compiled by examining high resolution spectra of the sun, Arcturus and MuLeo. Arcturus and MuLeo are cool giants with large amounts of spectral lines, both located at the end of the GALAH temperature range. Continuum regions derived from them should be free of lines for most GALAH targets.

The continuum points are fitted by the Python function `scipy.interpolate.UnivariateSpline` with smoothing factors `s=1e6` for CCD1 and 2 and `s=1e8` for CCD3. These values are chosen after trial and error fitting of over a hundred spectra by eye.

As GUESS uses a global model fit to derive parameters, the spectra are interpolated on to a common wavelength grid before dividing by the continuum fit. Table 4.1 shows the wavelength range for each CCD.

TABLE 4.1: Wavelength table for the common grid.

CCD	colour	wavelength [Å]	$\Delta\lambda$ [Å]
1	blue	4717 - 4887	0.0453
2	green	5651 - 5864	0.0546
3	red	6483 - 6729	0.0623

TABLE 4.2: Parameter summary of the model grid.

parameter	range	increments
$T_{\text{eff}}$ [K]	2500 - 8000	200 ( $T_{\text{eff}} < 4000$ ), 250 ( $T_{\text{eff}} > 4000$ )
$\log g$ [cms $^{-2}$ ]	-0.5 - 5.5	0.5
[Fe/H] [dex]	-5 - 1	1 ([Fe/H] < -3), 0.5 (-3 < [Fe/H] < -1), 0.25 (-1 < [Fe/H])

These wavelength windows are smaller than most of the stars to minimise the possibility of a stellar spectrum lying partially outside the grid. They will fit all stars with radial velocities below 1040 km/s, this is substantially larger than the local escape velocity of 317 km/s. Figure 4.2 shows an example of a normalised star.

After each CCD is continuum normalised, all three CCDs are stacked together for parameter estimation. If continuum is not fitted properly, the star is flagged and discarded.

A total of 16783 AMBRE models are used for deriving stellar parameters. The parameter ranges are summarised in Table 4.2. The model grid has an initial resolution of  $R=150000$  before being convolved down to HERMES resolution. The next sections compare the accuracy of two approaches in obtaining stellar parameters- simplex and nearest neighbor.

#### 4.1.2 Simplex

Geometrically, in a given  $n$  dimensional space, a simplex is a generalised tetrahedral region which has  $n + 1$  vertices. It is so named because it represents the simplest shape in the given space. A simplex in stellar parameter space ( $T_{\text{eff}}$ ,  $\log g$ , [Fe/H]) would be a tetrahedron with four vertices.

The basic rationale behind the simplex method is to constrain the stellar parameters of a star by interpolating between only the four models consisting the parameter simplex. Treating all spectra as high dimensional vectors, the simplex is constructed by firstly finding the closest model to the data spectrum (for clarity, it is referred as model<sub>c</sub>) in

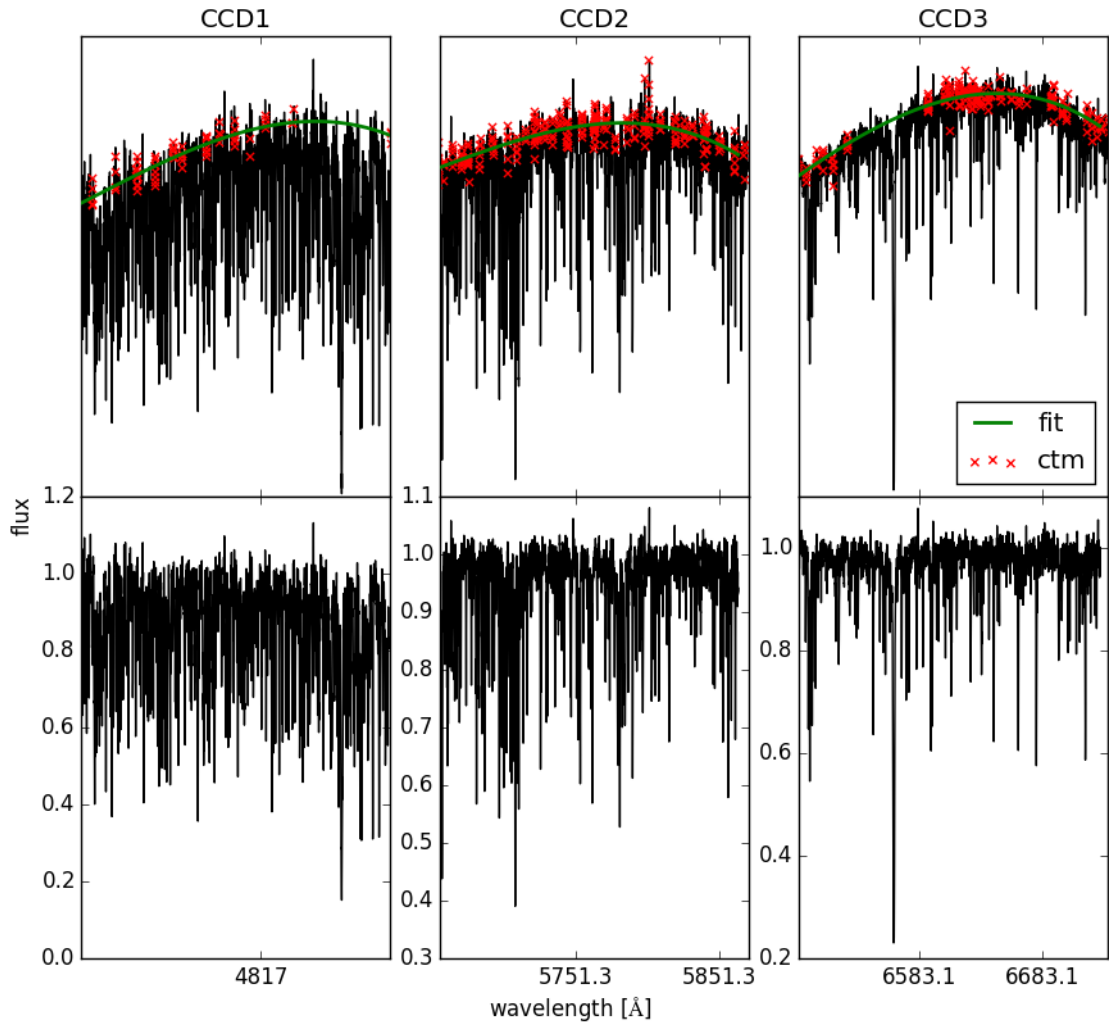


FIGURE 4.2: Upper panel: An example of the unnormalised spectrum of a star. Bottom panel: the corresponding normalised spectrum. The red crosses are the HERMES continuum regions used in the fit (green line).

Euclidean space by minimising the dot product<sup>1</sup>. The next step is to find all the models with parameters within one increment of  $\text{model}_c$ . For example, if one particular model<sub>c</sub> has  $T_{\text{eff}} = 4500\text{K}$ , then all models with  $T_{\text{eff}} = 4250\text{K}$  and  $4750\text{K}$  are selected (this is similarly applied to the other two parameters). The Euclidean distance from all selected models to  $\text{model}_c$  are calculated to find the model which is both closest to  $\text{model}_c$  in both Euclidean and parameter spaces. This leaves four models for each star-  $\text{model}_c$  and three models closest to  $\text{model}_c$ .

<sup>1</sup>Finding the distances to all 16783 models is the most time consuming part of the algorithm. M. Ireland has kindly provided a matrix operation script which calculates distances to all models for all stars in a very efficient way.

Ideally, these four models should form a simplex in parameter space which encloses the (yet unknown) parameters of the data spectrum, as illustrated in Figure 4.3. The four models are combined linearly to reconstruct the data spectrum using the Python package `numpy.linalg.lstsq`, which solves a linear matrix equation by minimising the Euclidean 2-norm. The final parameters for the data are the linear combinations of the model parameters, with the weights being the normalised linear matrix solution.

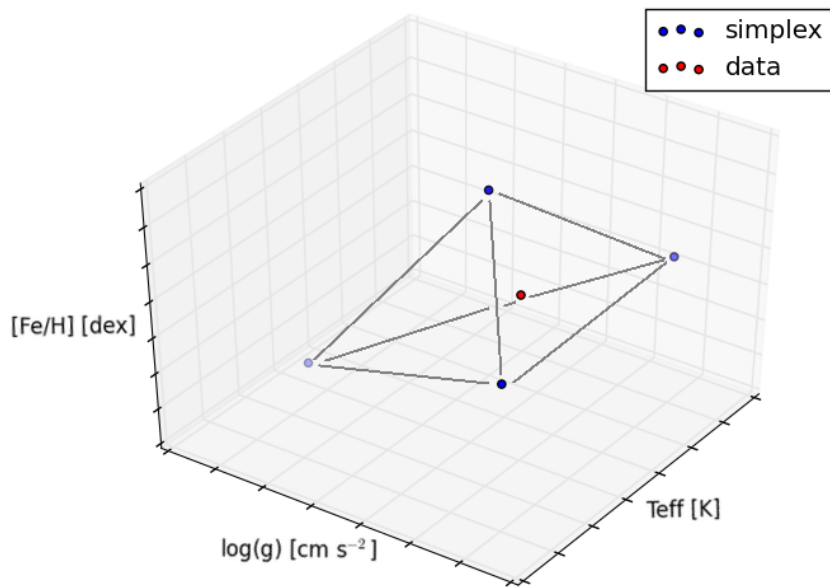


FIGURE 4.3: Illustration of the simplex method. The four blue vertices are the four models constructing the simplex which encloses the red data point.

The advantage of this method is that given a close enough  $\text{model}_c$ , it constrains the final parameters to be within the simplex, hence reducing the possibility of wildly wrong values. However after testing this method on Gaia benchmark stars with known parameters, three non trivial issues are discovered-

1. It is not guaranteed that the simplex will enclose a given star. If the star lies very far away from the model grid, the simplex constructed from its  $\text{model}_c$  will also be distant from the star.
2. There is also no guarantee that the final derived parameters will be within the simplex, as the final linear combination is an independent process. Figure 4.4 illustrates both issue 1 and 2 for the star 18Sco.

3. For stars located on the edges of the model grid, its  $\text{model}_c$  will have parameters at the ends of the parameter sequence. The simplices for these stars are certainly non-enclosing.

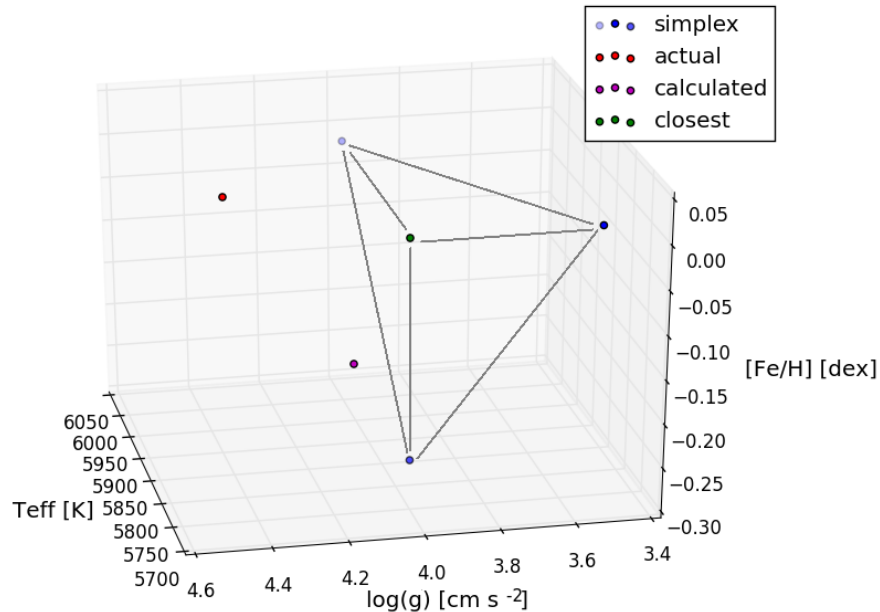


FIGURE 4.4: The ‘actual’ point (red) represents the Gaia parameters for 18Sco. The simplex is constructed using the closest model (green) and three other model points (blue). The final parameter from linear combination of the simplex points is in purple. Problematically, both the actual and calculated parameters are outside the simplex.

Issue one can be somewhat mitigated by minimising the model-data distance by finding the full width at half maximum (FWHM) which corresponds to the least distances in the resolution convolving function. The FWHM is combination of macroturbulence and instrumental broadening. Figure 4.5 shows the distributions of median model distances for three values of FWHM- 3.5, 4.0 and 4.5 for a set of 7000 HERMES stars. It is found that a FWHM of 4.5 produces the minimum median distances, hence this value is adopted. However as shown by the similarities in the three distributions, the effects of FWHM is not very significant.

Another way to ensure enclosure is to increase the size of the simplex itself- instead of selecting only the models within one parametric increment, models within two parametric increments are included also. However this defeats the whole purpose of the simplex- creating the smallest possible parameter space. Testing shows the derived parameters are less accurate.

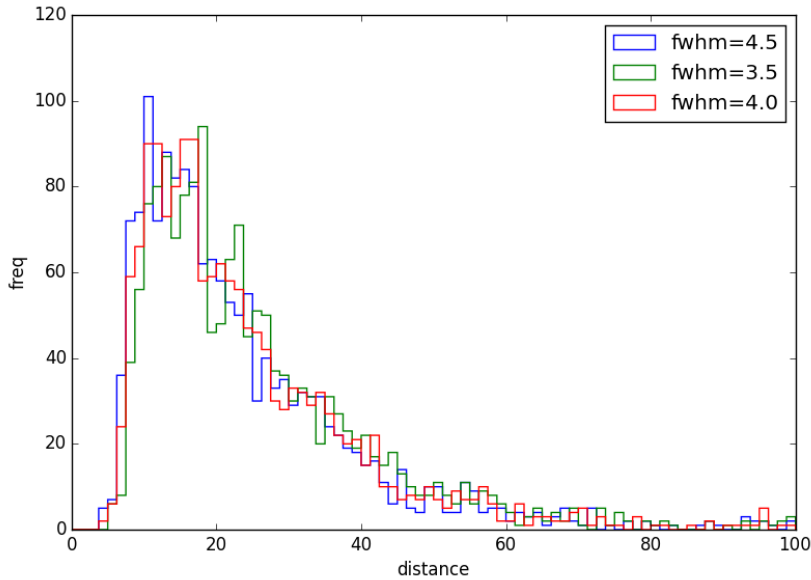


FIGURE 4.5: Distribution of median distances for three values of FWHM- 3.5 (green), 4.0 (red) and 4.5 (blue) based on a set of 7000 HERMES stars. Most of the models have distances between 10-30 units from the star. There are only a few models with distances greater than 50. Overall the FWHMs have similar distributions, with 4.5 being slightly better than the other two.

Issue two is equally hard to solve. One possible way to ensure the derived parameters being within the simplex is to use the median or the mean of the four simplex model parameter sets, in lieu to using an optimised linear combination. However since the model grid has fixed parameter increments, this would cause all derived parameters to also be quantised into increments. It is decided in the end to still use the linear combination, despite the occasional parameters being outside the simplex.

Issue three is a limitation of global model fitting and is not unique to the simplex method. Here it is dealt with in a rather pragmatic way- if  $\text{model}_c$  is on the end of the model parameter sequence, the script selects two increments in the same direction (for example, if a given  $\text{model}_c$  has  $T_{\text{eff}} = 8000\text{K}$ , then models with  $T_{\text{eff}} = 7750\text{K}$  and  $7500\text{K}$  are selected). Again, this means the likelihood of the simplex to enclose the parameters is lowered. Fortunately most of the stars are within reasonable distance from the grid, as shown by the sharp decrease in median distances in Figure 4.5.

Recognising these unsolved problems, the algorithm is run on 24 Gaia benchmark stars (Table 1.2). The differences between Gaia values and simplex values are summarised in Table 4.3.

TABLE 4.3: Benchmark results for the simplex method.

	Gaia – sim	Gaia – sim	std(Gaia – sim)
$T_{\text{eff}}$ [K]	190	-25	225
$\log g$ [cm s <sup>-2</sup> ]	0.55	0.34	0.56
[Fe/H] [dex]	0.37	0.34	0.27

One to one comparison with Gaia values and their differences are shown in Figure 4.9 and Figure 4.10 (the blue points).

#### 4.1.3 Nearest neighbor

Compared to the simplex method, the nearest neighbor method is less sophisticated but more robust. As its name suggests, this method finds the closest  $n$  models neighbors to the data spectrum in Euclidean space, then reconstructs the data spectrum using again a linear combination of these  $n$  neighbors. Similar to the simplex method, the final parameters are weighted averages of the  $n$  neighbor parameters, with the weights being the normalised linear combination solution.

Similar to the simplex method, minimising model-data distances is very important, and it is noted that this method will give wildly wrong results if a star is located too far away from the grid (hence the minimum distance FWHM=4.5 AMBRE model grid is used again). But unlike the simplex method, it does not break at the edge of the parameter grid.

The number of neighbors  $n$  is the only tweakable parameter in this algorithm. To find the optimal  $n$ , 7 different values are tested by running the algorithm on the 24 Gaia benchmark stars (Table 1.2). The results are shown in Figure 4.6. It is found that when  $n=10$ , the agreement with Gaia benchmark results is the best. Figure 4.7 shows a comparison between the actual data spectrum and the reconstructed spectrum from a linear combination of its nearest neighbors.

After deciding  $n$  to be 10, a trial run on 1626 stars is carried out to produce an HR diagram. Out of these 1626 stars, over 90% produced reasonable parameters which are within the parameter bounds of the model grid. They are plotted in Figure 4.8. Overall the HR diagram appears decent, with a defined main sequence and metallicity/temperature gradient in the giant branch. However there are two artefacts- firstly, there are lots of stars clustered around model temperatures in the green box near 6500K. Secondly, there

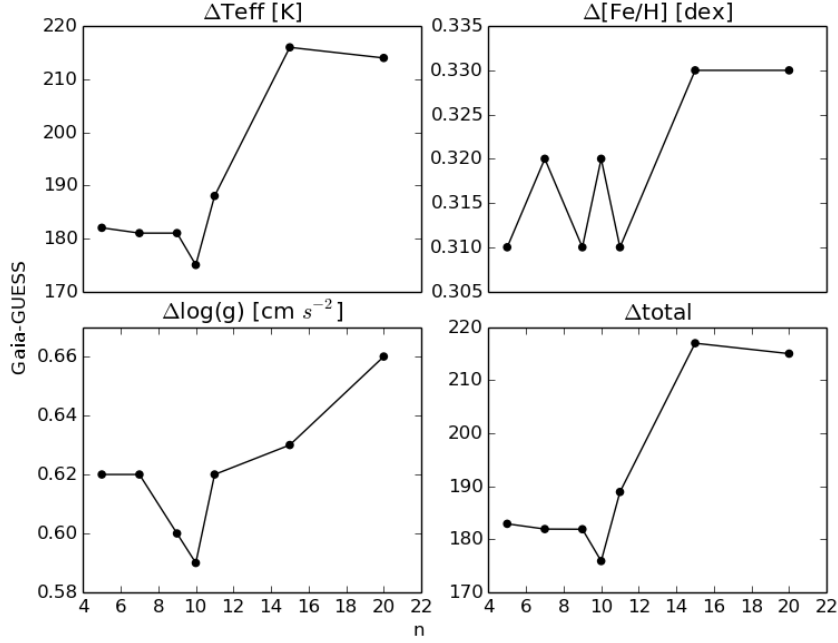


FIGURE 4.6: Average absolutes difference between Gaia and GUESS of the three parameters and their sum for 7 different  $n$ s (5, 7, 9, 10, 11, 15 and 20). The differences fluctuate from  $n=5$  to 9, reaching a minimum at 10 and increases dramatically after 11.

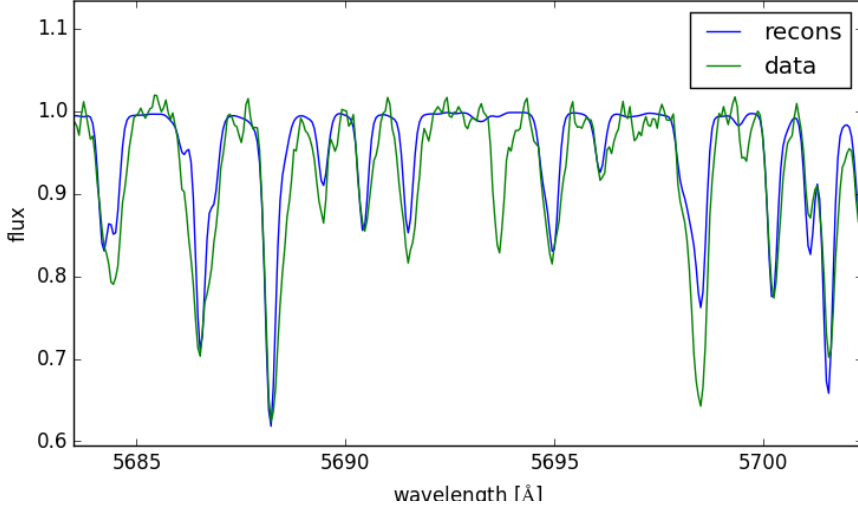


FIGURE 4.7: Comparison between the actual data spectrum (green) and the reconstruction spectrum (blue). With the exceptions of one missing line at  $5693\text{\AA}$  and two lines with incorrect line strength-  $5684\text{\AA}$  and  $5698\text{\AA}$ , all other features are well reproduced in the reconstruction. The models are not expected to reproduce the data perfectly as the data is subjected to observational limitations.

is an erroneous logg upturn at the beginning of the main sequence (corresponds to cool

dwarves).

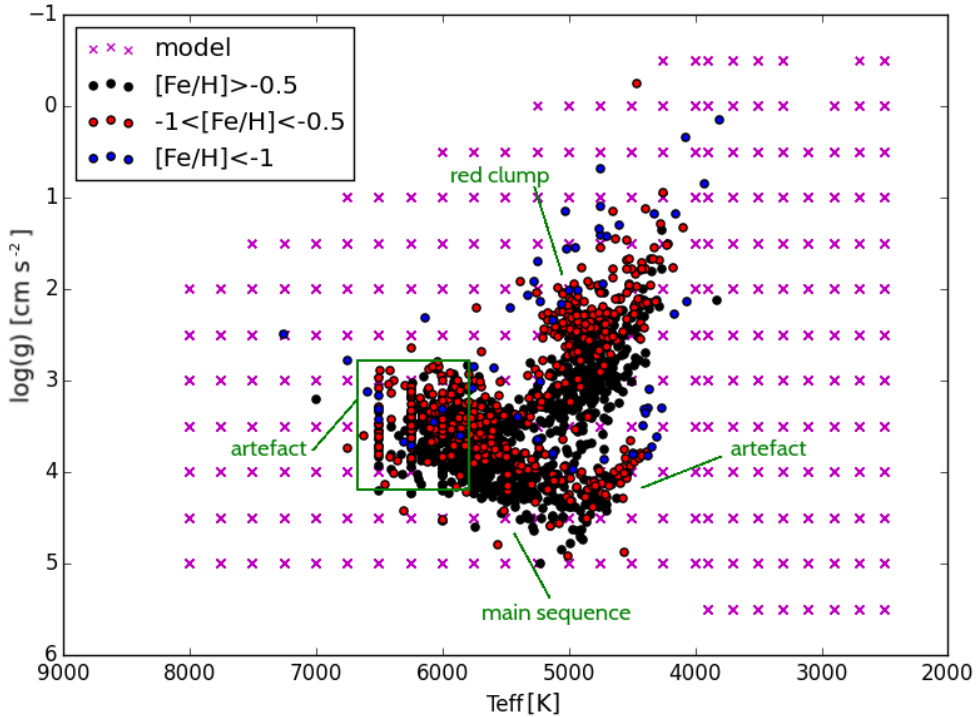


FIGURE 4.8: HR diagram of  $\sim 1500$  stars produced using nearest neighbor method, with metallicity binned into 3 bins. Two features of HR diagrams are labelled- the main sequence and red clump. Two artefacts are also present- the vertical striations in the green box and an upturn at the beginning of the main sequence. The model parameters are shown as purple crosses.

The first artefact is temperature dependent. All stars located on the clusters share the same  $T_{\text{eff}}$  for all 10 nearest neighbors, hence the derived temperatures are the same as the model values. This is because for spectra around 6000K, the Balmer series produce very dominant spectral features, thus causing all the nearest neighbors to have the same  $T_{\text{eff}}$ . To combat this, the algorithm is altered such that at least one of the 10 neighbors must have a different parameter value. For example, if all 10 neighbors have  $T_{\text{eff}} = 6000\text{K}$ , then the model furthest from data is replaced by the closest model within one increment (i.e. 5750K or 6250K, depends on which one is closer). The other two parameters are also altered this way, but instead of replacing the furthest model, the replacement model is appended. Thus in extreme cases when all three parameters are degenerate, the star will have 12 models.

The second artefact is a problem common to all global fitting parameter methods, originating from limitations in computing synthetic spectra. For cool dwarves, the iron atoms in the upper layers of the photosphere experience more ionisation than 1D LTE models

predict, this leads the predicted electron density to be lower than the actual value. This in turn decreases the model surface gravity to compensate, leading to inaccurate synthetic spectra in this parameter range. This upturn is also observed in the MATISSE global fitting algorithm (Recio-Blanco et al. (2006)). This is an issue in modelling, hence will not be addressed in this project.

24 Gaia benchmark stars are run through the algorithm, with results plotted in Figure 4.9 and Figure 4.10 (red dots). The differences between Gaia benchmark values and nearest neighbor values are listed in Table 4.4.

TABLE 4.4: Benchmark results for the nearest neighbor method.

	Gaia – nn	Gaia – nn	std(Gaia – nn)
$T_{\text{eff}}$ [K]	184	2.5	231
$\log g$ [ $\text{cm s}^{-2}$ ]	0.6	0.5	0.69
[Fe/H] [dex]	0.31	0.31	0.14

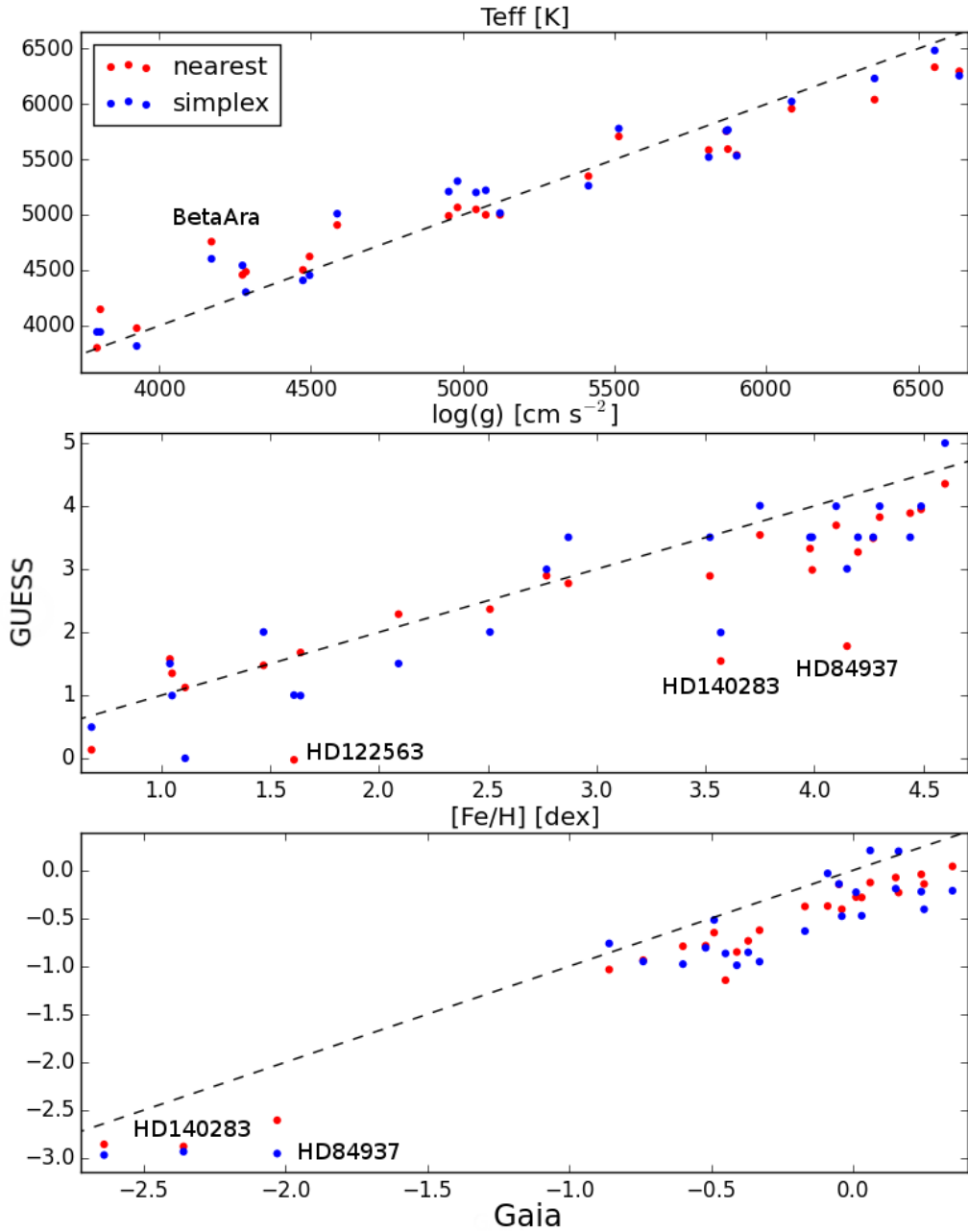


FIGURE 4.9: One to one comparisons of simplex method (blue points) and nearest neighbor method (red points) with Gaia parameters for 24 benchmark stars.  $T_{\text{eff}}$  seems to be in good agreement,  $\log(g)$  is less agreed and there seems to be a systematic offset in metallicity. All the outliers with labels are either cold or very metal poor, thus making their parameters very hard to pinpoint.

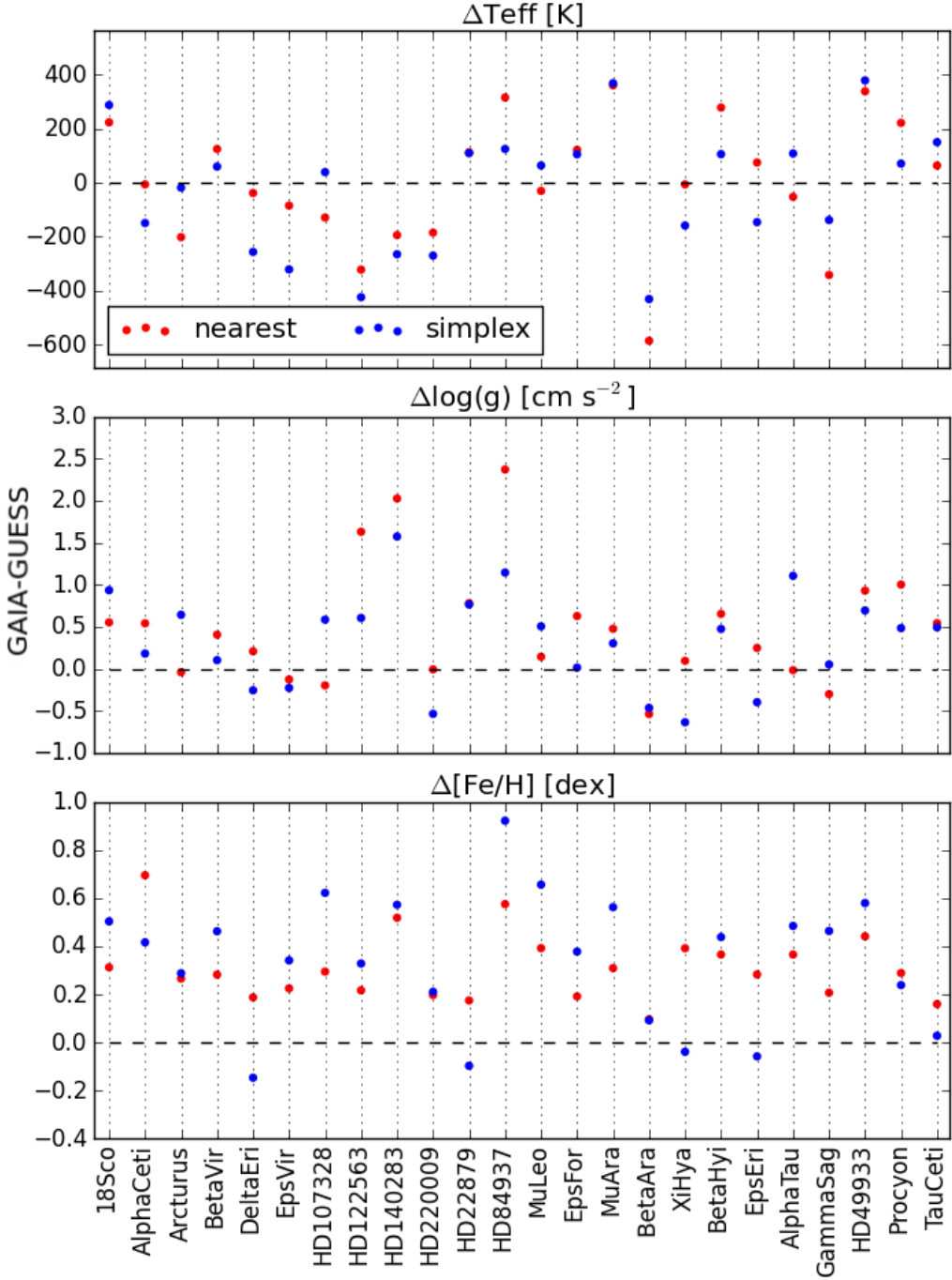


FIGURE 4.10: Differences between the Gaia parameter values for simplex method (blue) and nearest neighbor method (red). Again  $T_{\text{eff}}$  is in reasonable agreement,  $\log g$  is less agreed. Both methods seemed to be underestimating metallicity, with nearest neighbor being worse. Overall, nearest neighbor performs marginally better in terms agreement with Gaia benchmark stars.

#### 4.1.4 Compare and contrast

This section compares the simplex method and nearest method in terms of accuracy, efficiency and robustness in deciding which one will be included in the final GUESS release.

In terms of accuracy, nearest neighbor performs marginally better than simplex in agreeing with Gaia values for  $T_{\text{eff}}$  and [Fe/H]. Simplex gives a more accurate  $\log g$  by 0.05 cm s<sup>-2</sup>. The  $\log g$  inaccuracy of nearest neighbor is mainly due to three outliers- HD140283, HD122563 and HD84937, all of them being metal poor (reflecting the weakness of the GALAH wavelength choices as a metal rich disk survey). Removing these three outliers, nearest neighbor has the same order of accuracy.

In terms of efficiency, both methods require only one global neighbor search. However nearest neighbor is quicker because it usually does not require additional parameter searches whereas simplex requires three parameter searches.

In terms of robustness, both methods in their current incarnations seem to be equally robust. However, simplex method has the aforementioned three unresolved issues, making it not as optimal as it should be.

Overall, it is decided to use nearest neighbor as the parameter estimation for GUESS, with the intention of refining the simplex method so it can be added to the next GUESS expansion. An example output from both RV and parameter parts of GUESS is shown in Table 4.5.

## 4.2 Comparison with Other Pipelines

In this section, the stellar parameters derived by GUESS are compared to other independent pipelines. With the exception of Theremin (Section 4.2.3), all pipelines are external of GALAH.

### 4.2.1 ASPCAP

The APOGEE stellar parameters and chemical abundances are derived using the APOGEE Stellar Parameters and Chemical Abundances Pipeline (ASPCAP) (Shetrone et al. (2015)). ASPCAP relies heavily on its grid of several million synthetic spectra, computed using

TABLE 4.5: Example output from GUESS. The 999 values in the RV columns and 9999 values in the parameter columns indicate the star is not processed through the pipeline. The stars with flags are represented by 1s in the ‘sn\_low’, ‘bad\_weights’, ‘ctm’ and ‘out’ columns. The ‘out’ flags are overall quality indicators, which flag the stars with derived parameters outside the model ranges.

ID	v_ccd1	v_ccd2	v_ccd3	v_final	v_sigma	s/n_ccd1	s/n_ccd2	
133888	80.1	80	79.8	79.9	0.1	34.9	55.9	
133298	-55.2	-54.4	-55.4	-55.3	0.4	14.8	31.3	
133758	58.4	58.1	57.7	58.1	0.3	29.6	52.8	
133032	13.2	13.7	13.7	13.7	0.2	21	34.6	
133079	-10.8	-10.8	-11.3	-10.8	0.3	22.8	38.3	
133713	3.4	3.7	3.4	3.4	0.2	20.5	30.6	
133460	-22.5	-22.4	-22.9	-22.4	0.2	43.3	66.8	
133341	-16.1	-16.4	-16.8	-16.4	0.3	17.8	28.8	
133681	13.7	14.5	13.8	13.7	0.3	18.3	34.3	
133951	81.7	81.9	81.9	81.9	0.1	34	50.1	
	s/n_ccd3	sn_low	b_w	ctm	$T_{\text{eff}}$	logg	feh	out
	71.7	0	0	0	5418.1	3.505	-0.332	0
	43.3	0	0	1	9999	9999	9999	1
	66.8	0	0	0	5153.2	3.549	-0.245	0
	36.8	0	0	0	6215.9	3.955	-0.354	0
	45.2	0	0	0	5943.7	3.371	-0.512	0
	35.7	0	0	0	6049.4	4.029	0.049	0
	84.5	0	0	0	5784.4	4.137	-0.466	0
	39.7	0	0	0	5926.1	3.62	-0.336	0
	44.3	0	0	0	4666.3	2.795	-0.182	0
	58.2	0	0	0	5504.4	3.747	-0.687	0

Kurucz atmospheric model (Castelli and Kurucz (2004)). In addition to the usual stellar parameters of  $T_{\text{eff}}$ , logg and [Fe/H], the grid also has the dimensions of carbon, nitrogen, alpha element abundances.

The stellar parameters are determined by finding the best matched synthetic spectra from the grid. This is done by solving  $\chi^2$  minimisation problem in the 6 dimensional stellar parameter-abundance space. Abundances are again derived using  $\chi^2$  minimisation using the model grid- but instead of fitting the whole spectrum, only areas sensitive to the individual elements are fitted.

Based on a sample of 37 stars (provided by K. Schlesinger), it is found that GUESS and ASPCAP are in reasonable agreement for both  $T_{\text{eff}}$  and logg. Table 4.6 and Figure 4.11 summarise the differences between two pipelines. For [Fe/H], similar to the benchmark stars, GUESS appears to consistently under estimate. It should be noted however, that

ASPCAP metallicites themselves are not highly trust worthy, as indicated by the mismatch with SAGA photometric metallicities (Casagrande et al. (2014)), observed by K. Schlesinger.

TABLE 4.6: Differences between ASPCAP and GUESS for 37 stars.

	$ ASPCAP - G $	ASPCAP - G	std(ASPCAP - G)
$T_{\text{eff}}$ [K]	68	-23	96
$\log g$ [ $\text{cm s}^{-2}$ ]	0.23	0.17	0.23
[Fe/H] [dex]	0.28	0.27	0.14

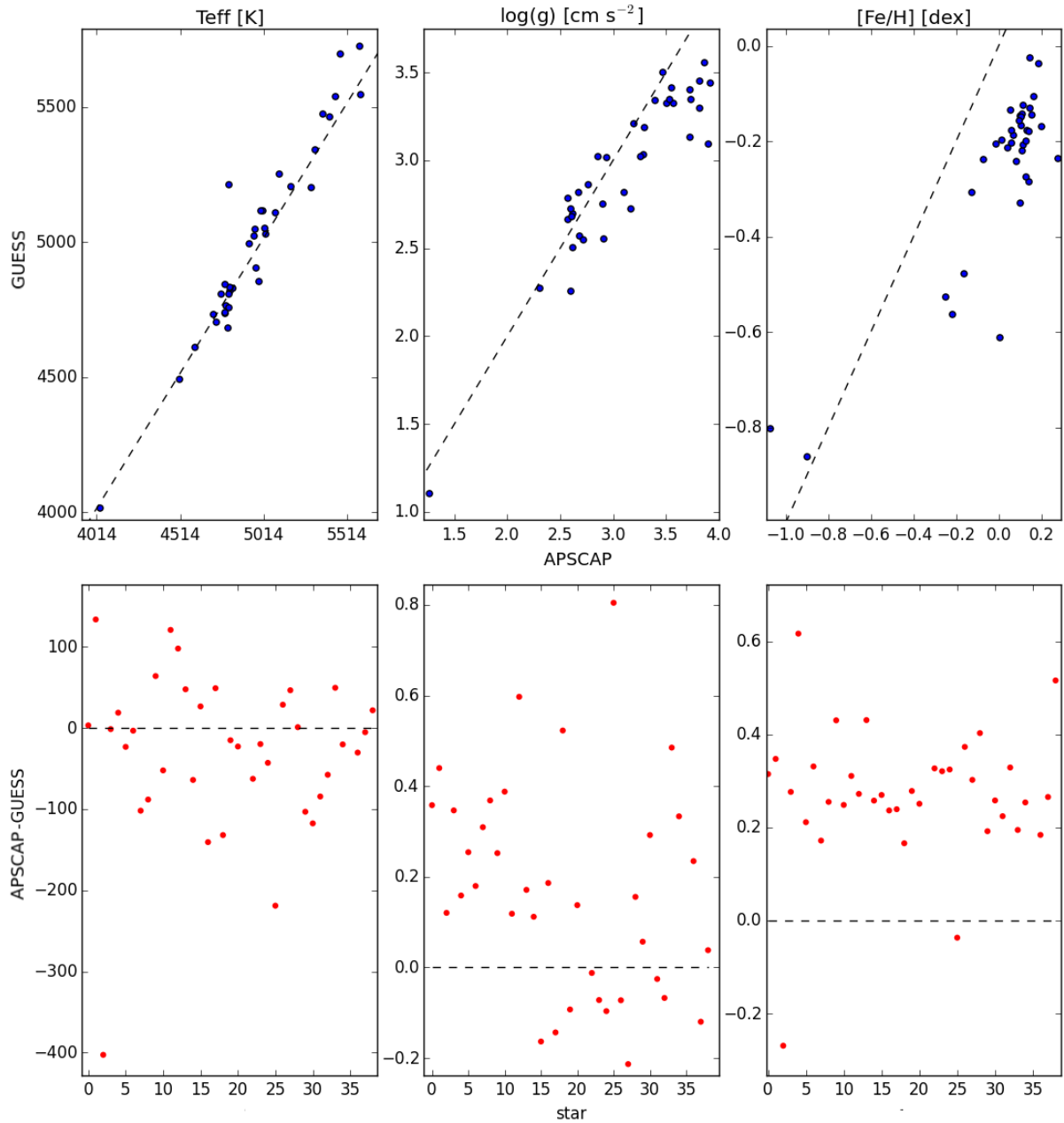


FIGURE 4.11: One to one comparison between ASPCAP and GUESS (top panels) and ASPCAP-GUESS differences (bottom panels) for 37 stars.  $T_{\text{eff}}$  and  $\log g$  are in good agreement but there is a clear offset in metallicity.

### 4.2.2 IRFM

The Infra-red Flux Method (IRFM, Blackwell et al. (1990), Casagrande et al. (2010)) is a photometric way of calculating  $T_{\text{eff}}$ , independent of synthetic spectra. The main motivation behind IRFM is to calibrate spectroscopic temperatures, as they are the dominant source of uncertainties in derived parameters/abundances.

IRFM uses the ratio of the total integrated flux ( $J_E$ ) to the monochromatic flux at a wavelength  $\lambda$  ( $F_{E,\lambda}$ ) as an indicator of temperature (Equation 4.1).

$$T_{\text{eff}}^4 = \frac{\phi(T_{\text{eff}}, g, \lambda, M)}{\sigma} \frac{J_E}{F_{E,\lambda}} \quad (4.1)$$

Where  $\sigma$  is the Stefan–Boltzmann constant and  $\phi$  is the monochromatic flux as a function of  $T_{\text{eff}}$ , surface gravity ( $g$ ), wavelength and metallicity ( $M$ ). Both  $J_E$  and  $F_{E,\lambda}$  are measured at the top of Earth’s atmosphere. The function  $\phi$  is determined theoretically from models. For stars hotter than 4200 K and wavelength greater than  $1.2\mu\text{m}$ , the stellar energy distribution is strictly Rayleigh-Jeans, hence model dependence of  $\phi$  is weak, making it relatively easy to calculate. Theoretically, IRFM provides excellent  $T_{\text{eff}}$  measurements, but its accuracy is limited by reddening in reality.

IRFM is run on a set of 1449 stars from 6 clusters by L. Casagrande using APASS and 2MASS photometry with Kurucz models. Comparison with GUESS are summarised in Table 4.7 and Figures 4.12, 4.13 and 4.14.

TABLE 4.7: Difference between IRFM and GUESS for 6 clusters.

cluster	stars	$ \text{IRFM} - \text{G} $ [K]	$\text{IRFM} - \text{G}$ [K]	$\text{std}(\text{IRFM} - \text{G})$ [K]
47Tuc	418	181	-150	208
M67	647	151	-22.2	302
NGC288	18	357	-208	409
NGC362	52	334	-151	440
NGC1851	12	195	-188	135
OmegaCen	302	197	-85	252

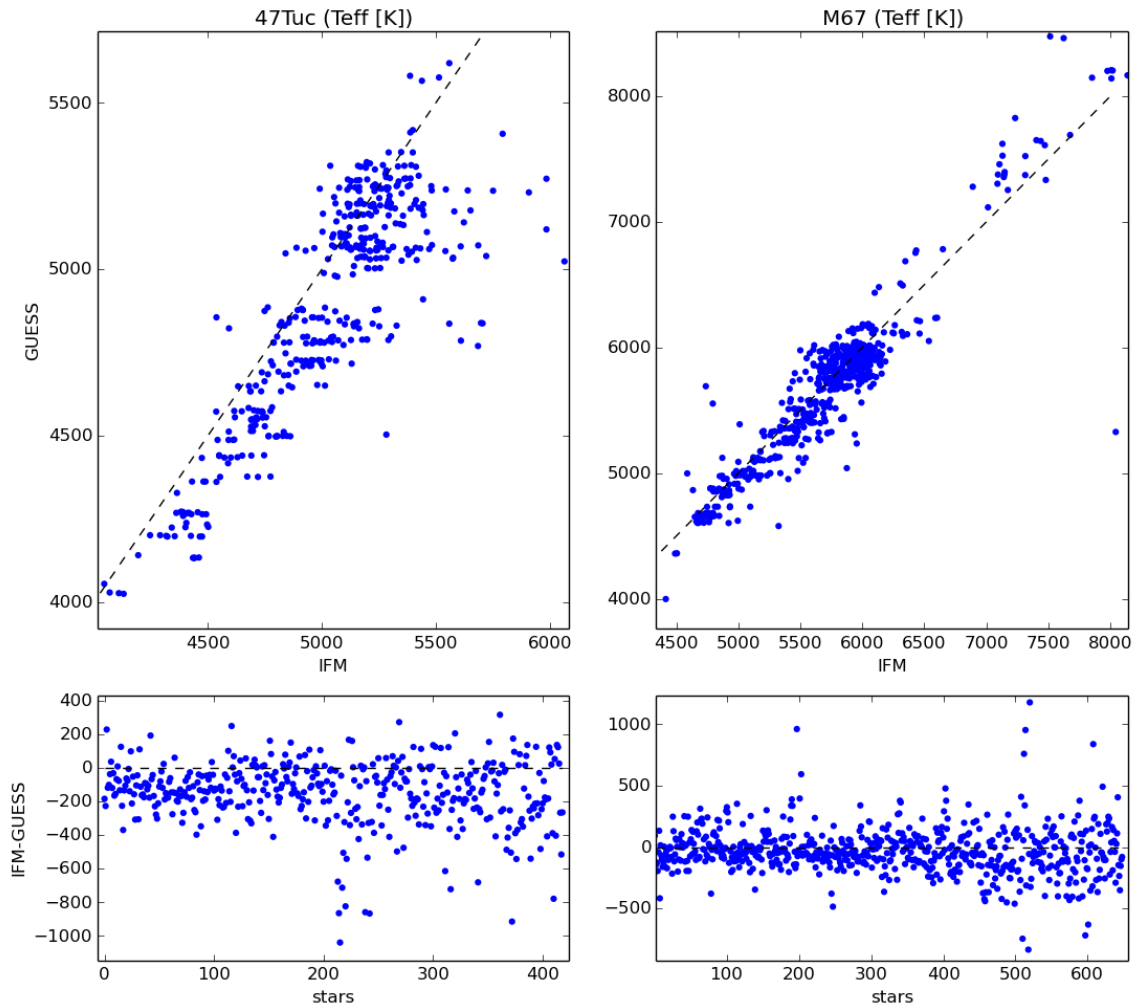


FIGURE 4.12: Top panels- one to one comparisons between IRFM and GUESS of 47Tuc (418 stars) and M67 (647 stars), respectively. Bottom panels- IRFM-GUESS for both clusters. There are horizontal temperature artefacts for both clusters in the top panels.

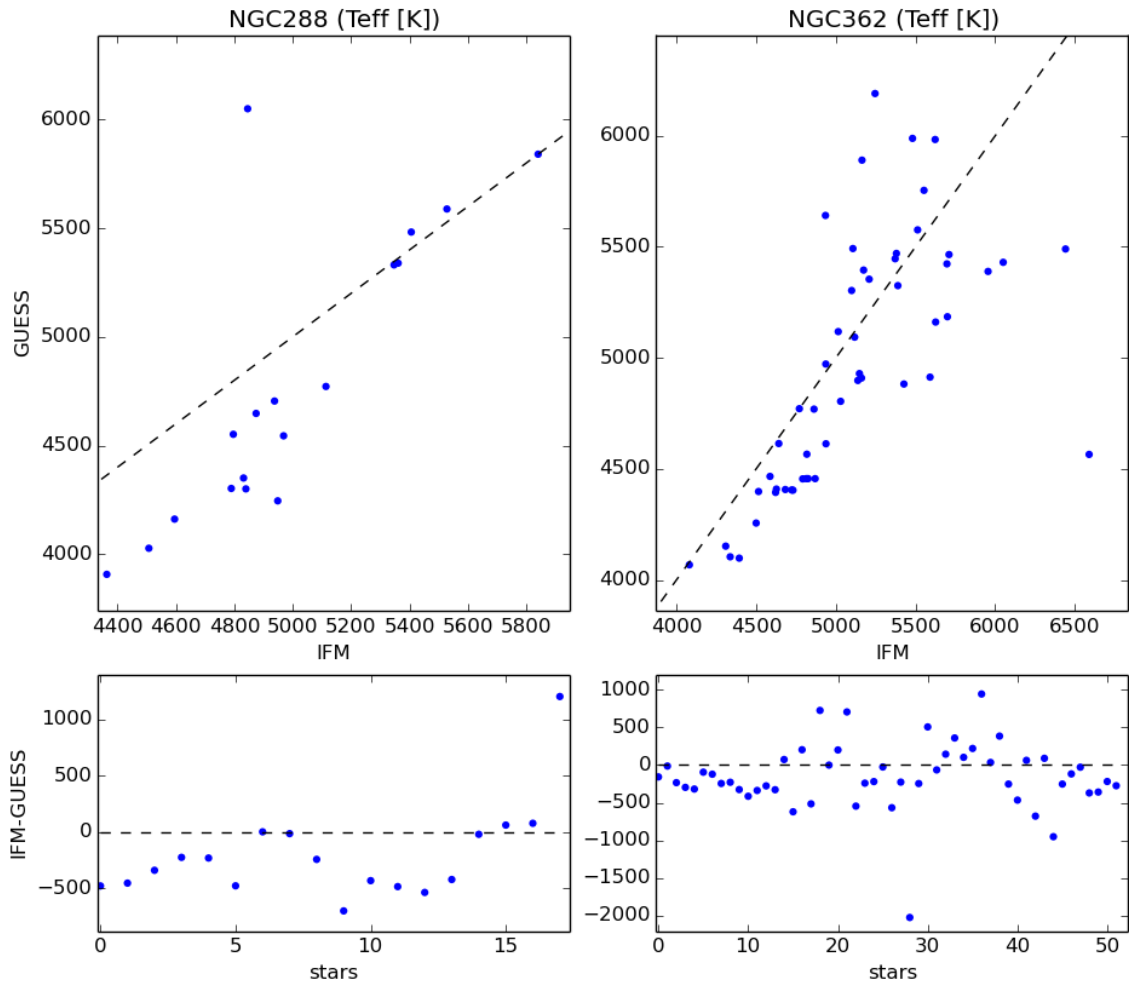


FIGURE 4.13: Top panels- one to one comparisons between IRFM and GUESS of NGC288 (18 stars) and NGC362 (52 stars), respectively. Bottom panels- IRFM-GUESS for both clusters. There are possible horizontal temperature artefacts for NGC362 in the top panel.

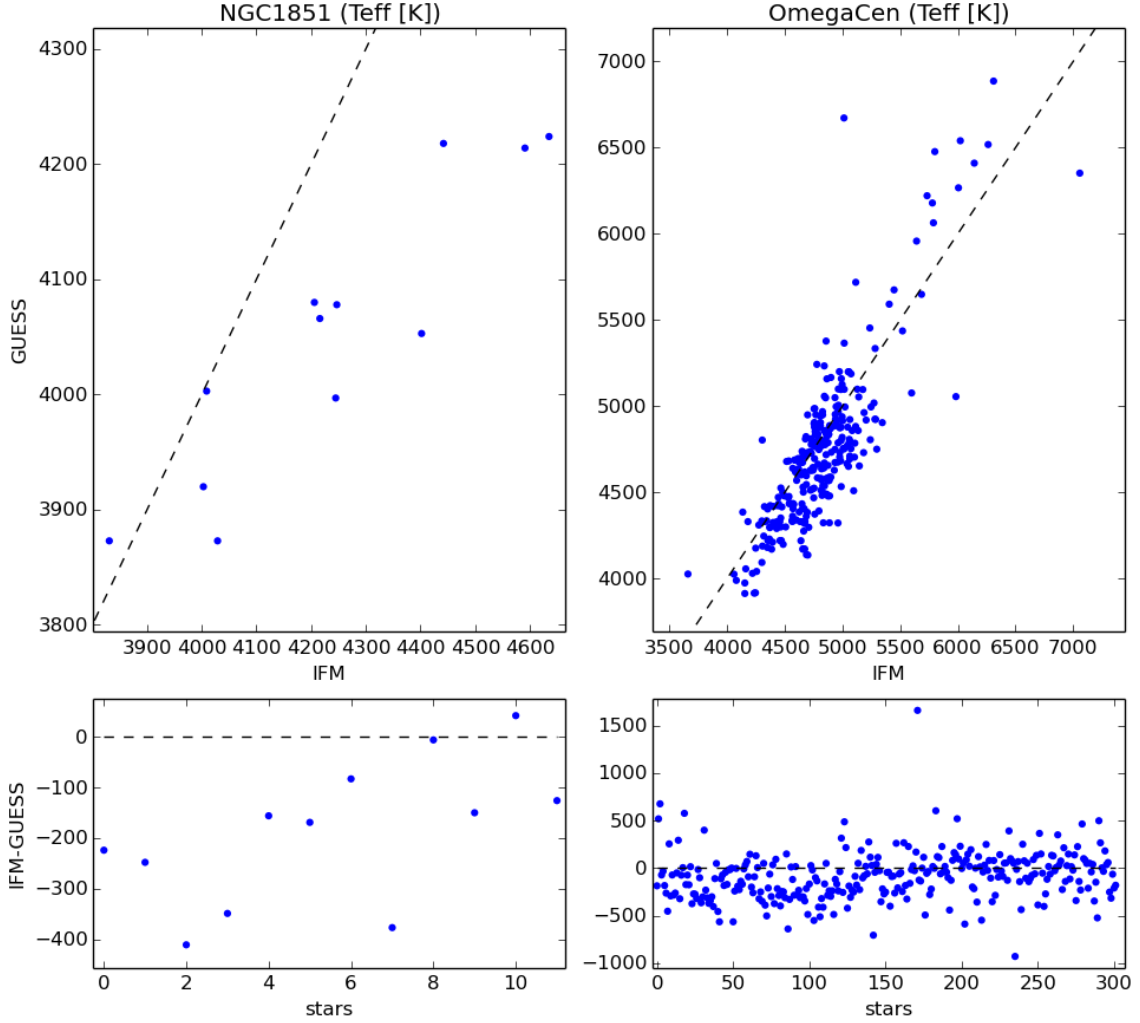


FIGURE 4.14: Top panels- one to one comparisons between IRFM and GUESS of NGC1851 (302 stars) and OmegaCen (302 stars), respectively. Bottom panels- IRFM-GUESS for both clusters. Both clusters are free from temperature artefacts in the top panels.

47Tuc, M67 and NGC362 exhibit temperature artefacts as horizontal dense rows. NGC1851 and NGC288 have too few stars to distinguish artefacts and OmegaCen appears to be artefact free. Interestingly, the artefacts are separated by  $\sim 80$  K, not coinciding with the 200 K temperature increment. They are also more prominent at lower temperatures ( $\sim 4000$  K). It is not entirely clear whether the artefacts are solely due to GUESS as they are not present in the ASPCAP and ARGOS samples (Section 4.2.4), both overlapping the same

problematic temperature range. A more detailed discussion of artefacts is presented in Section 4.4.2.

### 4.2.3 Theremin

Theremin (Wylie de Boer et al.) uses the EW method based on MOOG (Sneden et al. (2012)), with Kurucz or MARCS model atmospheres. The model parameter ranges are listed in Table 4.8.

TABLE 4.8: Parameter ranges for the model grid used in Theremin.

parameter	range	increments
$T_{\text{eff}}$ [K]	4000 - 7000	500
$\log g$ [ $\text{cm s}^{-2}$ ]	-1.5 - 5	0.5
[Fe/H] [dex]	-2 - 0.5	0.25

Originally, initial temperature and  $\log g$  guesses are obtained photometrically from 2MASS and/or APASS (Henden et al. (2012)). And Theremin provides its own metallicity estimates based on line strength. Using these parameters, Theremin synthesises model spectra at all nearby model grid points and accesses the excitation and ionisation balance from iron and titanium lines. Using rough interpolation to firstly narrow down the approximate location of the optimal parameters, Theremin then uses BOBYQA (Powell (2009)), a finer optimisation method to pin point the exact parameters. This process is done iteratively, until the convergence criteria (based on the sum of excitation potential slope, ionisation differences and reduced equivalent width slope) is achieved.

In the future, Theremin will also be capable of deriving individual elemental abundances. This is done by synthesising spectra at the previously determined stellar parameters for a range of abundances and finding the best matching abundance. There will be uncertainties associated with each stellar parameter and elemental abundance.

Both Theremin and GUESS are run on two samples of 10000 random stars. Figure 4.15 shows the HR diagrams from both pipelines. The GUESS HR diagram is similar to the one presented in Figure 4.8, with the temperature artefacts corrected. The  $\log g$  of the turn-off stars are underestimated by  $\sim 0.5 \text{ cm s}^{-2}$  and again there is an erroneous upturn at the beginning of the main sequence as the result of global fitting. The Theremin HR diagram is puzzling, as it contains no discernible structure and no metallicity gradient across the giant branch. Further more, there are clear artefacts at every increment in

temperature (500K) and substantial edge effects, especially at the 7000K end. With this troubling result, work is currently being done on implementing GUESS initial guesses into Theremin to constrain its outputs<sup>2</sup>. Figure 4.16 and 4.17 are Theremin outputs of 18 Gaia benchmark stars with and without GUESS priors, the differences between Gaia and Theremin are listed in Table 4.9 and 4.10.

---

<sup>2</sup>One additional possibility being investigated is a hybrid approach of inputting Theremin metallicities into GUESS to better constrain GUESS surface gravities.

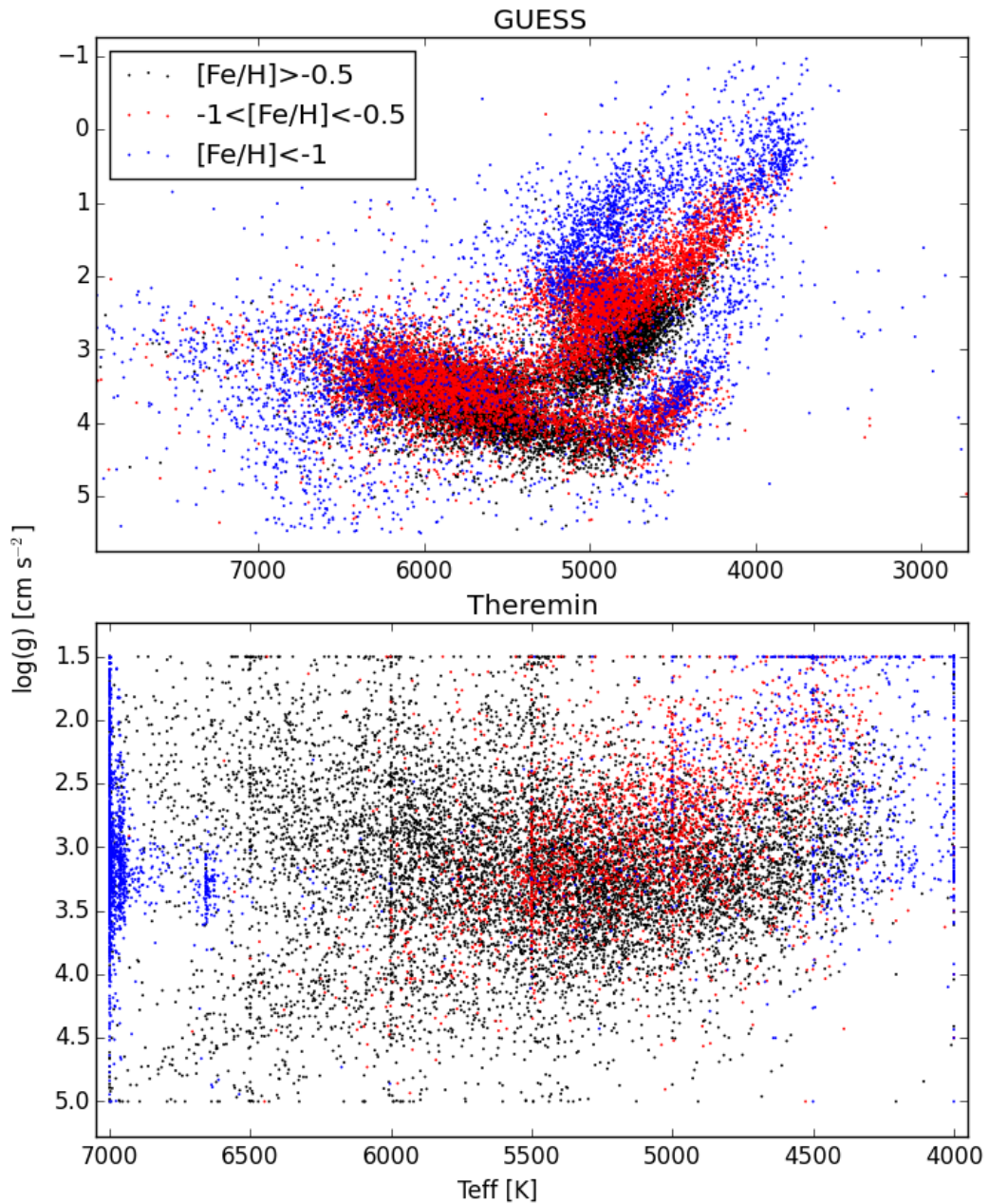


FIGURE 4.15: HR diagrams from GUESS (top) and Theremin (bottom) from two samples of 10000 randomly selected stars, with metallicity binned into three bins.

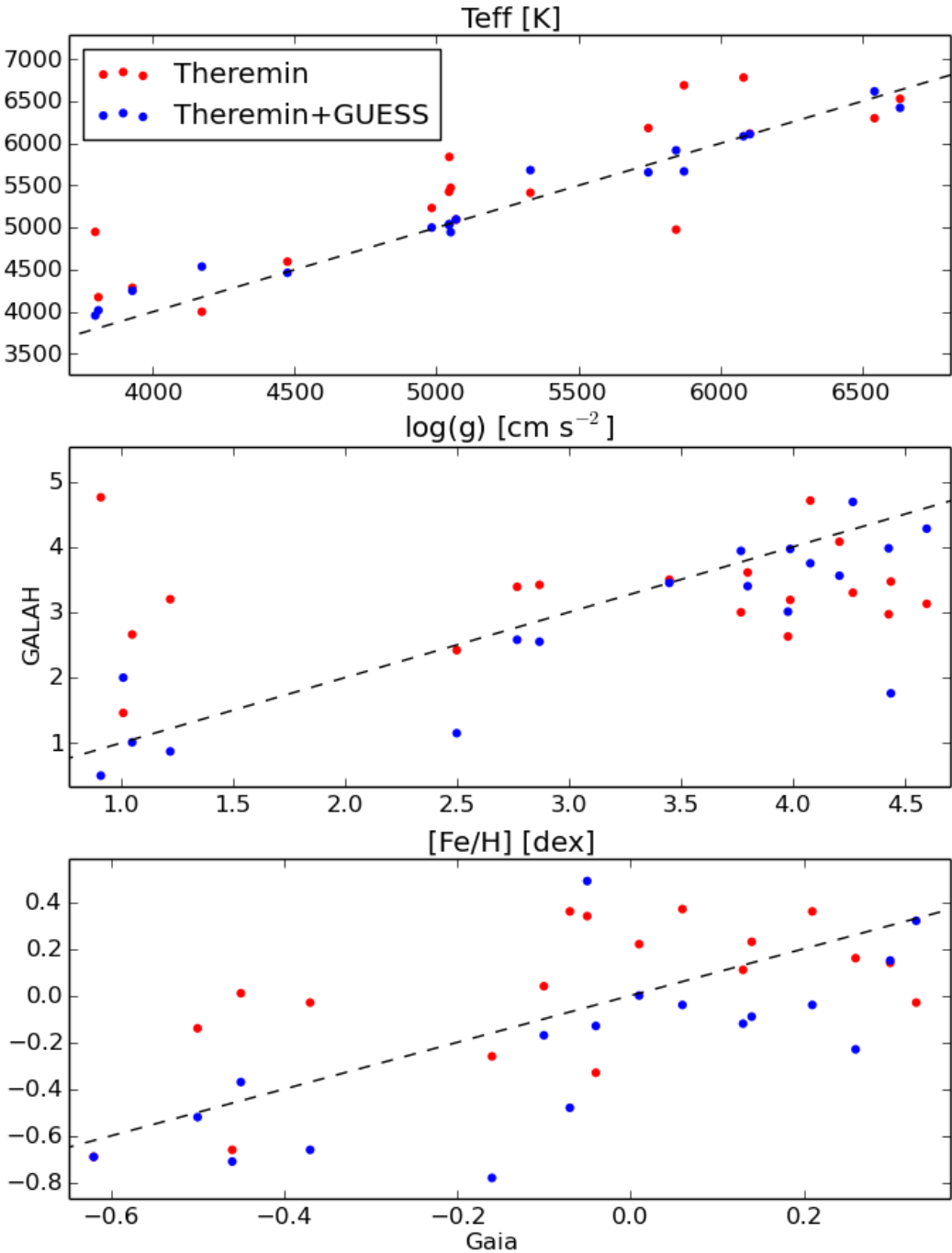


FIGURE 4.16: One to one comparisons between Gaia (x axis) and Theremin (y axis) for 18 benchmark stars. The red points are native Theremin outputs and blue are Theremin with GUESS.

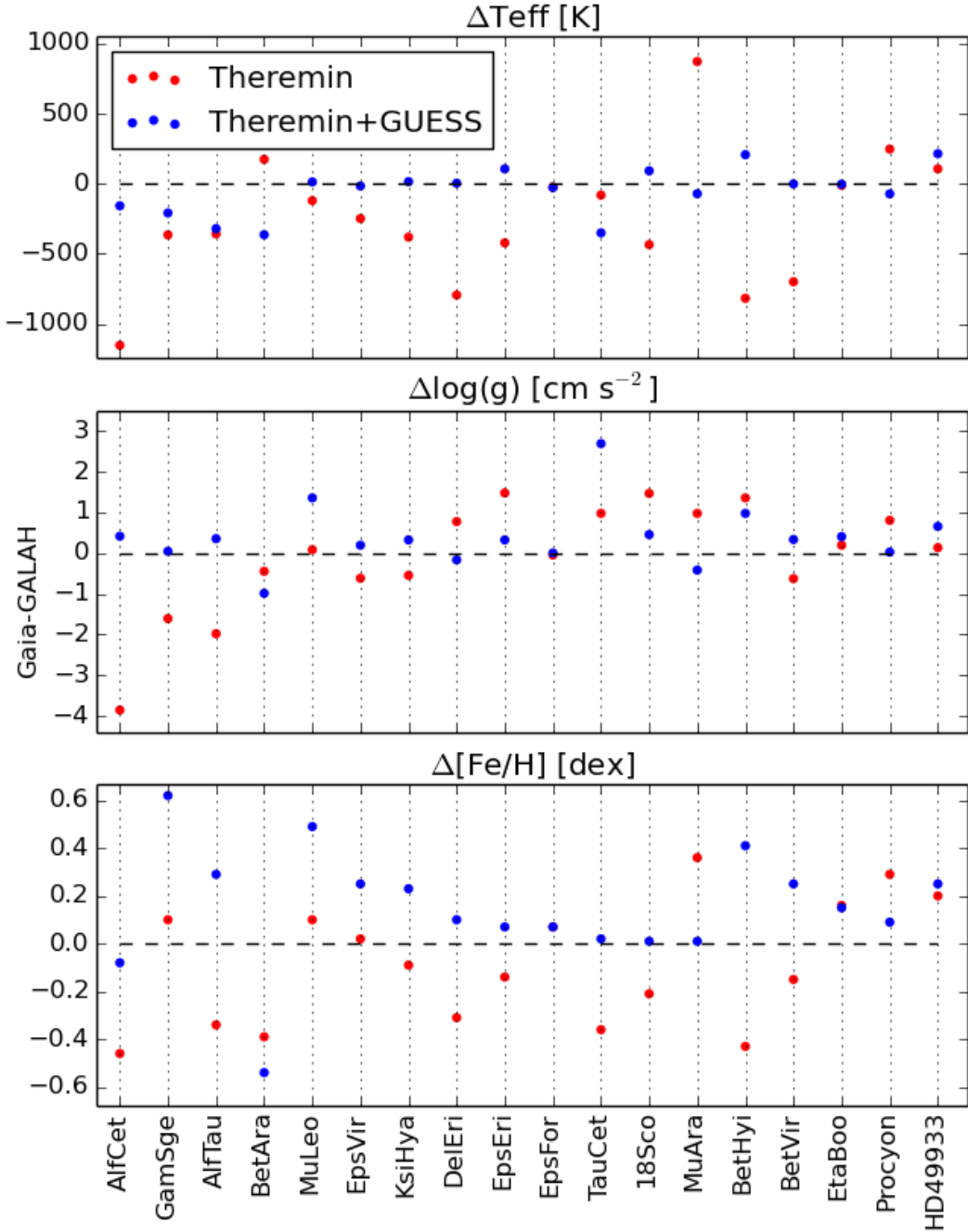


FIGURE 4.17: Differences between Theremin and Gaia for 18 benchmark stars. The red points are native Theremin outputs and blue are Theremin with GUESS.

These preliminary results appear to show that native GUESS (Table 4.4) outperforms native Theremin in  $T_{\text{eff}}$  and  $\log g$  and encouragingly, Theremin with GUESS outperforms

TABLE 4.9: Differences between Gaia and Theremin for 18 benchmark stars.

	Gaia – T	Gaia – T	std(Gaia – T)
$T_{\text{eff}}$ [K]	406	-252	453
$\log g$ [ $\text{cm s}^{-2}$ ]	1.0	-0.09	1.32
[Fe/H] [dex]	0.23	-0.09	0.25

TABLE 4.10: Differences between Gaia and Theremin with GUESS for 18 benchmark stars.

	Gaia – T + G	Gaia – T + G	std(Gaia – T + G)
$T_{\text{eff}}$ [K]	125	-54	166
$\log g$ [ $\text{cm s}^{-2}$ ]	0.56	0.38	0.74
[Fe/H] [dex]	0.22	0.15	0.24

both in all three parameters. However the scatter in [Fe/H] is still larger than native GUESS.

#### 4.2.4 ARGOS

The Abundances and Radial velocity Galactic Origins Survey (ARGOS) is a survey of 28000 stars in the Galactic bulge and surrounding disk. ARGOS stellar parameters are determined in a hybrid approach (Freeman et al. (2013)) using wavelength regions around the Ca-triplet. For  $\log g$ , [Fe/H] and  $[\alpha/\text{Fe}]$ , ARGOS finds the best matched model from a grid of synthetic spectra computed from 1D LTE Kurucz models by minimising  $\chi^2$ . To avoid degeneracy,  $T_{\text{eff}}$  is measured both photometrically by  $(J - K)_0$  colours and from a calibration sample which requires [Fe/H].

The process is iterative as  $(J - K)_0$  temperatures are  $\log g$  and [Fe/H] dependent and  $\chi^2$  minimisation of  $\log g$  and [Fe/H] is temperature dependent. In practice, an initial temperature estimate is firstly calculated using  $(J - K)_0$  colours with fixed  $\log g$  and [Fe/H]. Based on this estimate,  $\chi^2$  minimisation is performed to pin point  $\log g$  and [Fe/H]. The updated metallicities are then input into the calibration sample to produce the final temperature. This temperature is again passed to the  $\chi^2$  minimisation to produce  $\log g$ , [Fe/H] and  $[\alpha/\text{Fe}]$ . And finally, the  $[\alpha/\text{Fe}]$  value is used to derive the final  $\log g$  value using an alpha-enhanced grid.

Table 4.11 and Figure 4.18 show the comparison of 329 ARGOS stars with GUESS (provided by L. Doung). Figure 4.19 shows the HR diagrams from both pipelines, with BaSTI isochrones over plotted.

TABLE 4.11: Differences between ARGOS and GUESS for 329 stars.

	$ \text{ARGOS} - \text{G} $	$\text{ARGOS} - \text{G}$	$\text{std}(\text{ARGOS} - \text{G})$
$T_{\text{eff}}$ [K]	149	38	193
$\log(g)$ [ $\text{cm s}^{-2}$ ]	0.38	-0.06	0.49
[Fe/H] [dex]	0.22	0.11	0.28

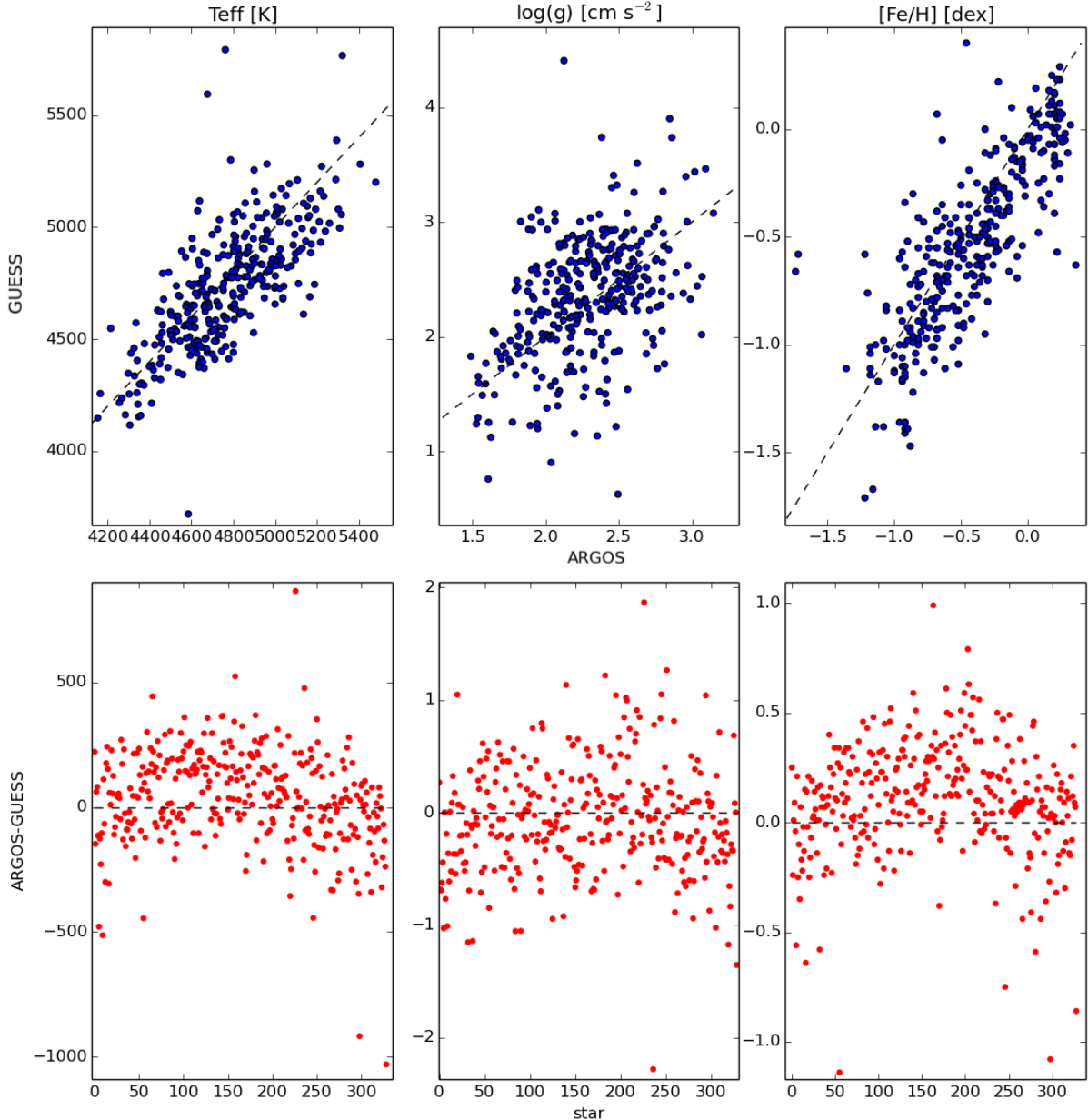


FIGURE 4.18: One to one comparisons between ARGOS and GUESS (top panels) and ARGOS-GUESS differences (bottom panels) for 329 stars. From the one to one plots, all three parameters are in good agreement, with  $\log(g)$  having a large scatter. It possible for the scatter to be caused by the  $\log(g)/[\text{Fe}/\text{H}]$  degeneracy in the Ca-triplets used in ARGOS.

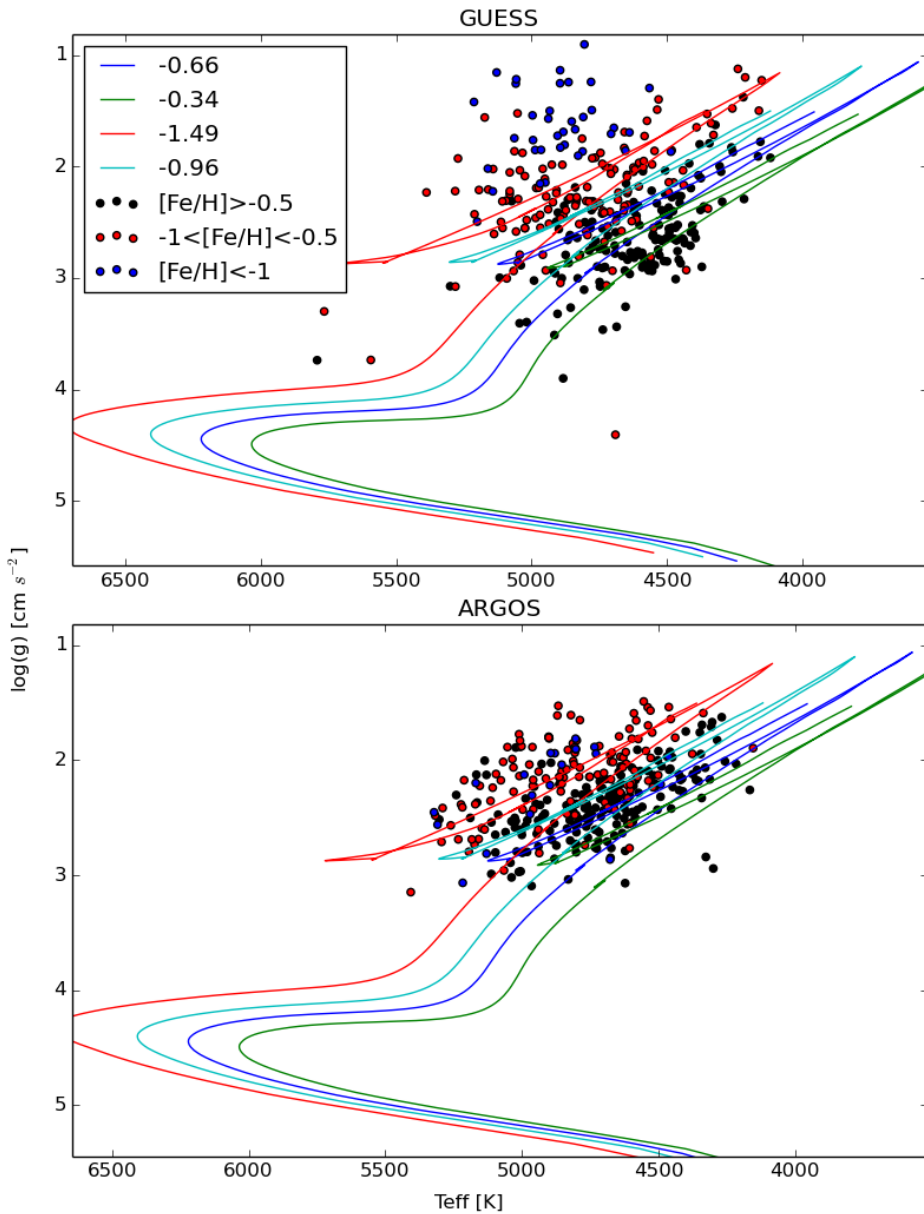


FIGURE 4.19: HR diagrams of both GUESS (top) and ARGOS (bottom) over plotted with four BaSTI isochrones with different metallicities- -0.34 (green), -0.66 (blue), -0.96 (cyan) and -1.49 (red). ARGOS appear to have smaller scatter than GUESS. GUESS has a clearer metallicity gradient consistent with the isochrones.

### 4.3 Clusters

In this section, stars from M67 and 47Tuc are analysed using GUESS. It is found that similar to the stars in Section 4.2, GUESS under estimates metallicities for both clusters.

### 4.3.1 M67

M67 is an open cluster estimated to be between 3.5 to 4 Gyr old (Sarajedini et al. (2009)). It is one of the oldest clusters in the near by galaxy. 1021 stars are analysed with GUESS and yielding reasonable parameters (i.e. the derived parameters are within the model parameter ranges listed in Table 4.2). They are presented in Figure 4.20. The mean metallicity is found to be -0.37 dex with a standard deviation of 0.43 dex. Burstein et al. (1986) gives M67 a metallicity of 0.1 dex. Bottom panel of Figure 4.20 shows diagonal artefacts which are previously undiscovered. A more detailed discussion on them is presented in Section 4.4.2.

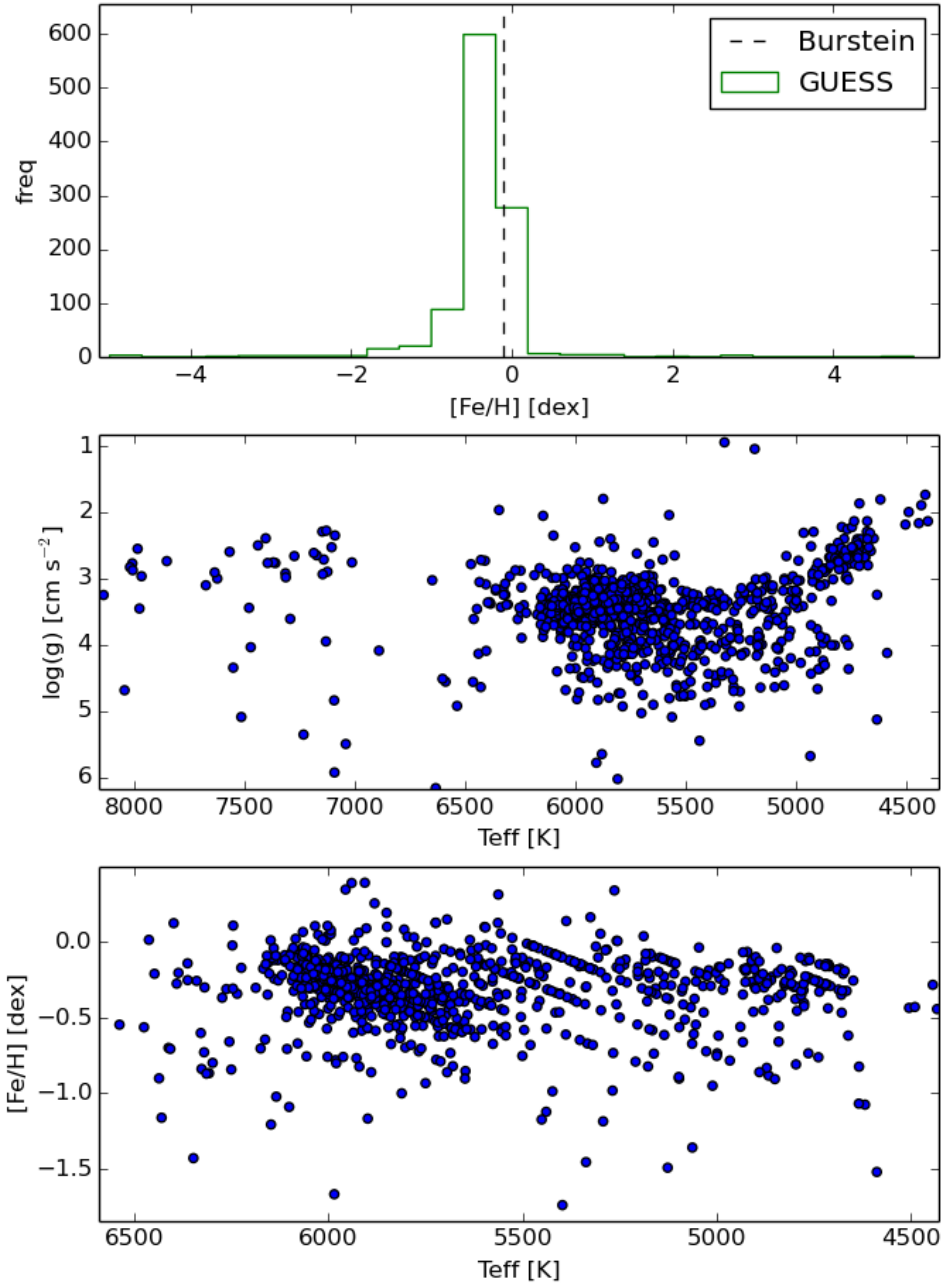


FIGURE 4.20: Top- GUESS metallicity distribution of M67 stars, with literature value plotted as the dashed line. Middle- plot of  $\log(g)$  vs  $T_{\text{eff}}$ . Bottom- plot of  $T_{\text{eff}}$  vs  $[\text{Fe}/\text{H}]$ . There are diagonal artefacts in the bottom panel.

### 4.3.2 47Tuc

47Tuc is a globular cluster with an estimated age of 13 Gyr (Carretta et al. (2000)). It is believed to be one of the most massive globular clusters in the galaxy. 1134 stars are analysed with GUESS and yielding reasonable parameters. In this sample, 174 stars have additional APASS photometry. GUESS parameters are presented in Figure 4.21. The mean metallicity is found to be -0.8 dex with a standard deviation of 0.23 dex. Harris (1996) gives 47Tuc a metallicity of -0.72 dex. Again diagonal artefacts are present in the [Fe/H] vs  $T_{\text{eff}}$  plot.

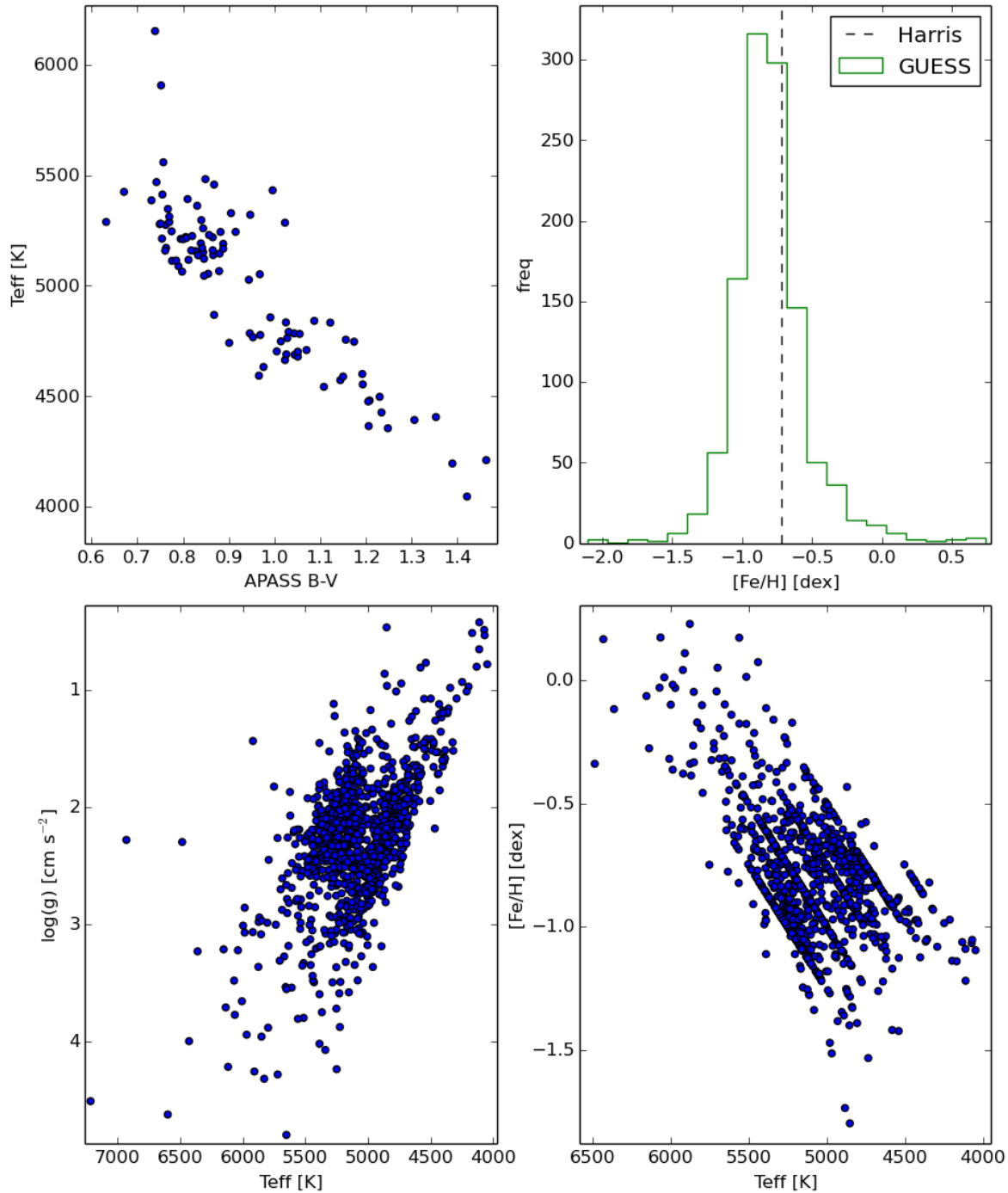


FIGURE 4.21: Top left- plot of APASS B-V photometry vs  $T_{\text{eff}}$ . Top right- metallicity distribution of 47Tuc, with literature value as the dashed line. Bottom left- plot of  $T_{\text{eff}}$  vs  $\log(g)$ . Bottom right- plot of  $T_{\text{eff}}$  vs  $[Fe/H]$ .

## 4.4 Discussion

This section addresses the problems found by comparing GUESS with other pipelines and ideas for improvements.

### 4.4.1 Uncertainties

Quantifying uncertainties is an important aspect for all analysis pipelines. It is a non-trivial issue since there are multiple sources of uncertainties ranging from instrumental to machine precision. Some pipelines adopt a fixed percentage of the derived stellar parameters as uncertainties. Others, like Oracle, use Monte-Carlo for a more quantitative treatment.

As GUESS is a first estimate pipeline, the issue of quantifying uncertainties is not as vital as the more sophisticated pipelines like Theremin. Thus a more pragmatic approach is used to give an indication of the errors involved.

In Section 4.2, a total number of 1757 stars have their GUESS parameters compared to corresponding literature. Adopting the mean absolute difference as the uncertainty indicator (these values are summarised in Table 4.12), the approximate uncertainties for the three parameters are:  $T_{\text{eff}} = 164$  K,  $\log g = 0.38 \text{ cm s}^{-2}$  and  $[\text{Fe}/\text{H}] = 0.23 \text{ dex}$ , calculated as the size weighted averages of the samples. It should be noted that GUESS is consistently under estimating metallicity. One possible explanation is the dominating effects of  $T_{\text{eff}}$  in the spectra lead to the nearest neighbors having erroneous metallicities. The exact cause for this behaviour is under investigation.

TABLE 4.12: Mean absolute differences between GUESS and 4 other pipelines compared in this section.

method	stars	$T_{\text{eff}}$ [K]	$\log g$ [ $\text{cm s}^{-2}$ ]	$[\text{Fe}/\text{H}]$ [dex]
Gaia	24	184	0.6	0.31
ASPCAP	37	68	0.23	0.28
IRFM <sup>3</sup>	418, 647, 302	181, 151, 197	n/a	n/a
ARGOS	329	149	0.38	0.22
	weighted average	164	0.38	0.23

<sup>3</sup>Only the clusters with more than 100 stars are selected. The smaller clusters (18, 52 and 12 stars) have relatively large temperature scatter (with the exception of the 12 stars from NGC1851). It is unknown if the large scatter is caused by erroneous GUESS parameters or is an artefact of small sample sizes (although the latter is more likely, judging from the larger clusters). Thus until more stars are added, these clusters are excluded.

#### 4.4.2 Issues

One repeated problem in GUESS is the presence of artefacts. Firstly, there are artefacts present in temperature (Figure 4.8), likely due to the prominent Balmer series dominating the Euclidean norm, causing all nearest neighbors having the same temperature. This is solved by forcing GUESS to have at least one neighbor with different parameters (Section 4.1.3). However this solution did not entirely work, as in Section 4.3, artefacts are also found in  $T_{\text{eff}}$  vs [Fe/H] plots. Figure 4.22 shows the  $T_{\text{eff}}$  vs [Fe/H] plot of a random sample of 936 stars. The red crosses are stars corrected for temperature artefacts. As predicted, they are near the Balmer range ( $\sim 6000$  K). The diagonal artefacts seem to be most pronounced near  $\sim 5500$  K. The spacing between each artifact is roughly around the temperature and metallicity increments. One can conclude that simply using the nearest neighbors and forcing some of them to be different parametrically is not sufficient enough to eliminate these structures. This calls for more sophisticated methods (such as the simplex method) and a more carefully constructed model grid.

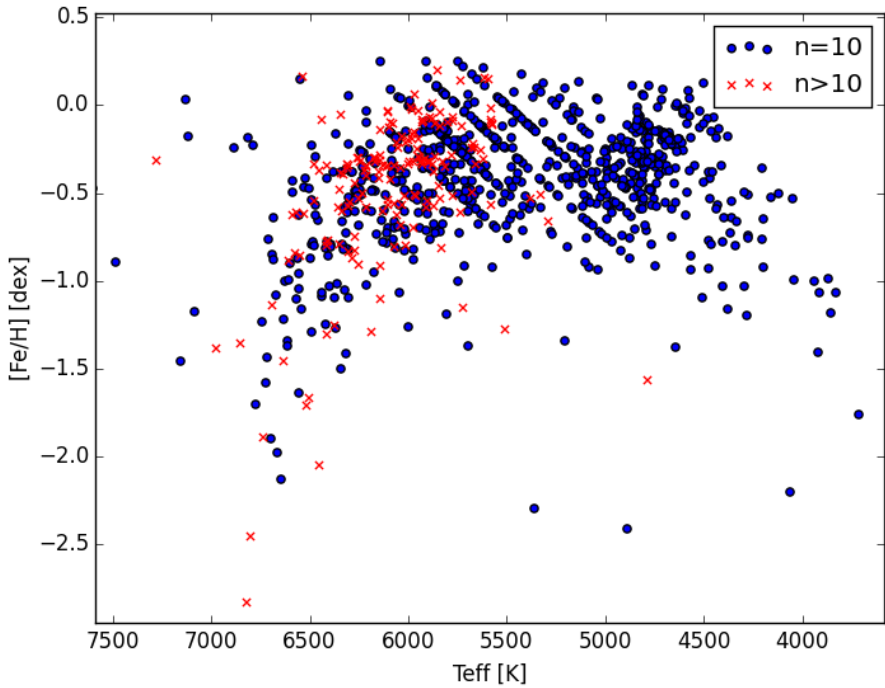


FIGURE 4.22:  $T_{\text{eff}}$  vs [Fe/H] plot for a selection of 936 random stars. The stars with 10 neighbors are represented by blue circles and stars with more than 10 neighbors (174 stars) are red crosses.

There are additional artefacts found in the IRFM comparison (Section 4.2.2). However these structures do not appear in any other comparisons. Therefore it is difficult to determine if they are of the same origin.

GUESS also appears to under estimate metallicities repeatedly. This is believed to be caused by the temperature dominance in the spectral features. One possible remedy is to add in weights during neighbor search to down play the  $T_{\text{eff}}$  influence on the nearest neighbors or using an entirely different metric. On the other hand, one can simply empirically correct for these offsets as a temporary fix.

Finally, GUESS yields unreasonable parameters for a portion ( $\sim 5\%$ ) of stars. Given a large survey, this can be problematic. It is beneficial to implement iterative algorithms in both RV and parameter parts of GUESS to ensure the maximum number of stars are successively analysed.

#### 4.4.3 GUESS 2: Electrical Boogaloo

A more sophisticated method for parameter estimation is planned for the next expansion of GUESS. After researching into the mechanics of multiple pipelines, the author believes an iterative global  $\chi^2$  minimisation in parameter space could potentially yield improved results. In particular, the method outlined in Xiang et al. (2015) is very inspiring. It uses a hybrid approach combining a) a weighted average of the parameters of nearest neighbors and b)  $\chi^2$  minimisation in parameter space. There are procedures in place to account for  $T_{\text{eff}}$  dominance in  $\chi^2$  and model outliers.

The choice of models is another vital component of GUESS. The AMBRE grid currently employed is purely synthetic and it suffers from model related issues such as the erroneous upturn at the beginning of the main sequence. An alternative would be to adopt an empirical grid, such as the MILES library (Sánchez-Blázquez et al. (2006)). Empirical grids are free of modelling biases but do not have the comprehensive parameter coverage of the synthetic grids. Obviously, more work needs to be done to test out these potential alternatives.

*Stay tuned for GUESS 2: Electrical Boogaloo. Coming to a server near you in 2020.*

## Chapter 5

# Application- Local Linear Embedding

**T**HIS chapter explores one application of GUESS parameters as substructure indicators in the Local Linear Embedding projection of GALAH stars.

### 5.1 Local Linear Embedding

The main aim of dimensional reduction is to reduce the dimensionality of the data yet preserving as much information as possible. One widely used method is the Principle Component Analysis (PCA). PCA is a way of identifying patterns in a set of high dimensional data, and reducing its dimensionality, with minimal information lost. Only the principle components which encode majority of the information are retained. Mathematically, this is done by finding the covariance matrix of the data set and finding the associated eigenvalues and eigenvectors. The principle components are expressed as the eigenvectors with the highest eigenvalues (Smith (2002)).

Local Linear Embedding (LLE) is a relatively new way of performing dimensional reduction first proposed by Roweis and Saul (2000). The input spectra can be seen located on a manifold in high dimensional space. The LLE algorithm compresses the dimensions by performing a mapping between this high dimensional space and a low dimensional space. The effect of LLE is illustrated by Figure 5.1.

More formally, the set of observed spectra can be considered as  $N$  vectors, each with dimension  $D$ , sampled over the manifold. As they are all stellar spectra, one would expect

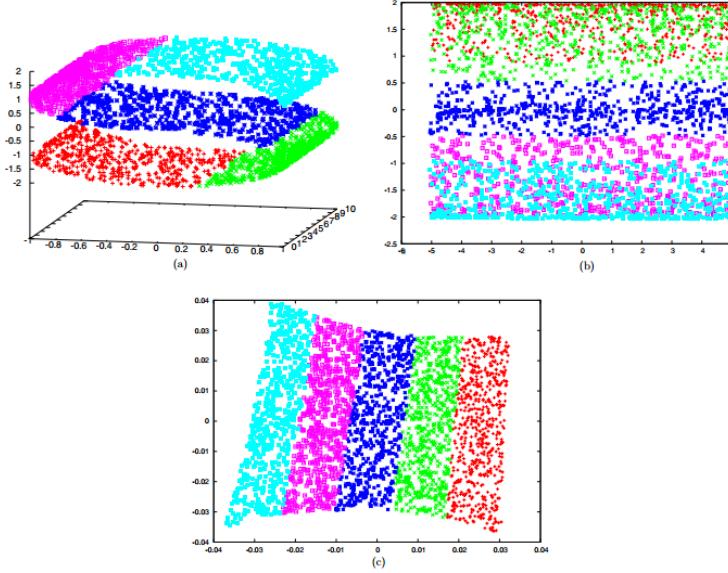


FIGURE 5.1: (a) is the 2D manifold which contains the data in a 3D space. (b) is the projection of the points in 2D done by PCA. (c) is the projection done by LLE. Both PCA and LLE ‘unravel’ the manifold out. Note in (b) the unraveled points are mixed up whereas in (c) the points are separated. Figure taken from Daniel et al. (2011).

the spectra to be very similar within any neighborhood of the manifold. The reduction in dimensionality is performed firstly by reconstructing each spectrum ( $\vec{x}_i$ ) using its  $n$  nearest neighbors. This is essentially a least squares problem with the goal of minimizing the total reconstruction error  $\epsilon$

$$\epsilon(W) = \sum_i^N |\vec{x}_i - \sum_j^k W_j^i \vec{x}_j|^2 \quad (5.1)$$

The matrix  $W$  has columns of weight vectors required for reconstructing each individual spectrum.  $W$  is invariant under the linear mapping between the high and low dimensional spaces. This means that the high dimensional geometry is equally valid in the lower dimensional space. Hence the nonlinearity between the neighborhood is preserved after transformation. The next step would be to find the LLE coordinates in the lower dimensional space. The problem is again of least squares-

$$\epsilon(y) = \sum_i^N |\vec{y}_i - \sum_j^k W_j^i \vec{y}_j|^2 \quad (5.2)$$

Where  $\vec{y}$  is the lower dimensional LLE vector. Since  $W$  is invariant, we need to find coordinates  $\vec{y}$ 's such that the reconstruction error  $\epsilon(y)$  is minimal. Mathematically, this

is the same as solving a  $N \times N$  eigenvalue problem, where the eigenvectors corresponding to the  $l$  number of smallest eigenvalues<sup>1</sup> are the  $l$  LLE dimensions of the original data. Over all, about 95% of the information embedded in the original data is preserved in the first three LLE dimensions (Vanderplas and Connolly (2009)).

The main LLE algorithm can be summarized in the following three steps-

- Neighborhood search: finding the nearest  $n$  Euclidean neighbors.
- Weight matrix construction.
- Calculating the LLE coordinates by solving the eigenvalue problem.

There is only one parameter adjustable in this algorithm, which is the number of neighbors  $n$ .

The LLE procedure is computationally intensive- for the addition of each new spectrum, the algorithm has to rerun from the start. One way to avoid long computation time would be to train it on a training set (Vanderplas and Connolly (2009)), new points can be added without resolving the eigenvalue problem. This can be done by firstly decompose the new points by the training set (obtaining the normalised weight matrix  $W$ ), then multiplying by the LLE coordinates of the training set-

$$LLE_{\text{new}} = W^T \times LLE_{\text{trainning}} \quad (5.3)$$

Other than being computationally costly, LLE relies on the assumption that the original manifold is sampled evenly. Despite having these weaknesses, LLE still out performs PCA in terms of unraveling the manifold, as seen in Figure 5.1. This is because PCA assumes each data point can be reconstructed using the a linear combination of the *whole* data set, whereas LLE only reconstructs using the nearest  $n$  neighbors. This means that the overall nonlinearity is preserved. Another advantage over PCA is the volume of information contained within the LLE components- the first LLE component contains all the information in the first five PCA components.

---

<sup>1</sup>Actually one takes only from the second smallest eigenvalue onwards, as the smallest eigenvalue corresponds to a global translation of the data.

### 5.1.1 Number of neighbors

The art of choosing  $n$  is somewhat subtle, as there is no ‘correct’ way of selecting this number. If  $n$  is set too low, then the underlying manifold would be under sampled. This would mean a loss of information between the neighborhoods and making the projection more prone to outliers. On the other hand, if  $n$  is set too high, the assumption of local linearity would be destroyed by over sampling. To explore this, the LLE algorithm (using the Python package `mdp`) is run on 500 GALAH stars for a range of  $n$  values. The resulting projections are limited to 3 LLE dimensions and are colour coded in GUESS  $T_{\text{eff}}$  (Figure 5.2).

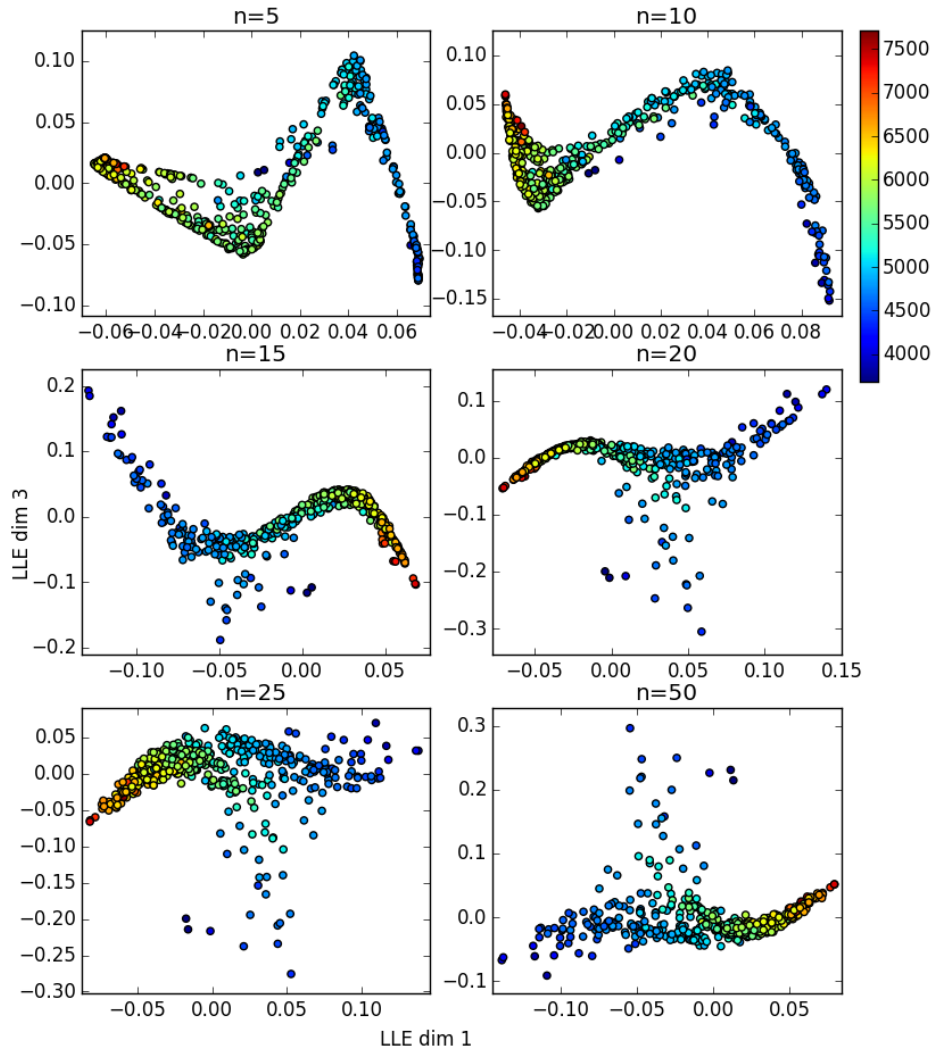


FIGURE 5.2: LLE projections of 6 different  $ns$ , colour coded with GUESS temperatures.

One thing immediately noticeable in Figure 5.2 is the clear trend of temperature in all projections. This is unsurprising as temperature is the dominating stellar parameter. The  $n=5$  projection appears to be under sampled, as many stars lie on straight structures. On the other end,  $n=50$  projection is over sampled, as indicated by its diffuse shape. In fact, it would appear that larger  $n$  corresponds to more over sampling. In the end,  $n$  is set to 10 as a compromise between the two extremes.

## 5.2 The GALAH LLE Projection

A larger sample of 2000 GALAH stars is decomposed with LLE using 10 nearest neighbors and 3 LLE output dimensions. The projection is colour coded with GUESS  $T_{\text{eff}}$  (Figure 5.3) ,  $\log g$  (Figure 5.4) and [Fe/H] (Figure 5.5).

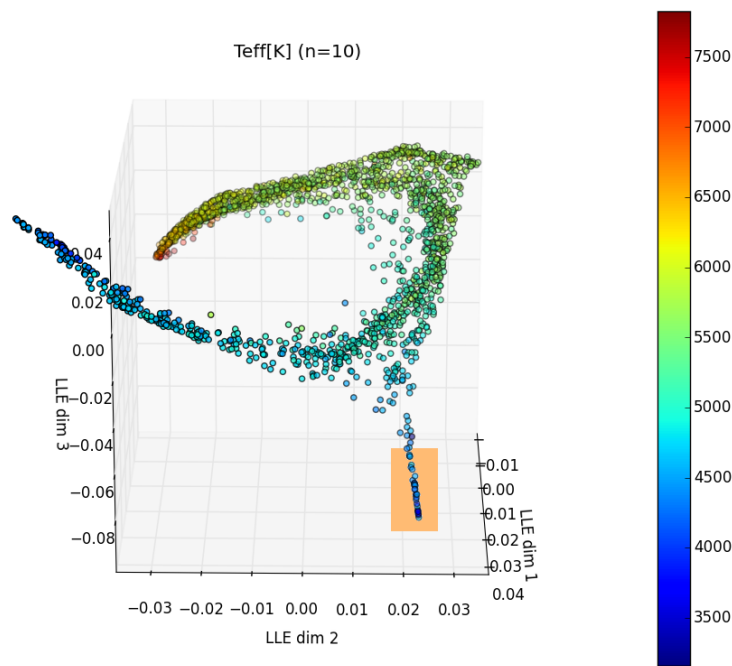


FIGURE 5.3: LLE projection of 2000 GALAH stars, colour coded with GUESS  $T_{\text{eff}}$ . An outlying group is identified in orange.

The outlying group in Figure 5.3 is of particular interest. Since it is located substantially far from the main stellar locus, one expects the spectra to be very different. Figure 5.6 shows six stars from the group.

All six stars in Figure 5.6 appear to have the continuum normalisation problem described in Chapter 3 Section 3.4. This illustrates the power of LLE as a mean to pick out peculiar

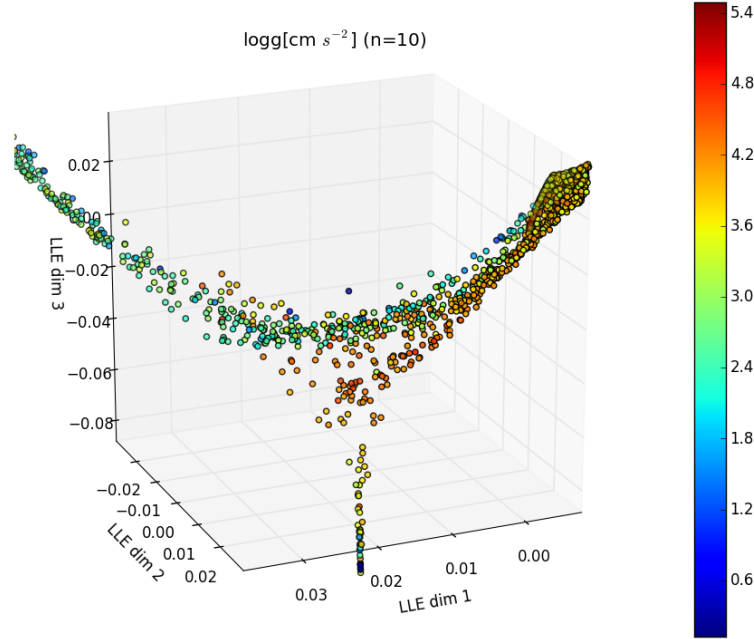


FIGURE 5.4: Same LLE projection of 2000 GALAH stars, colour coded with GUESS  $\log g$ . Two groups of stars are separated by their  $\log g$ .

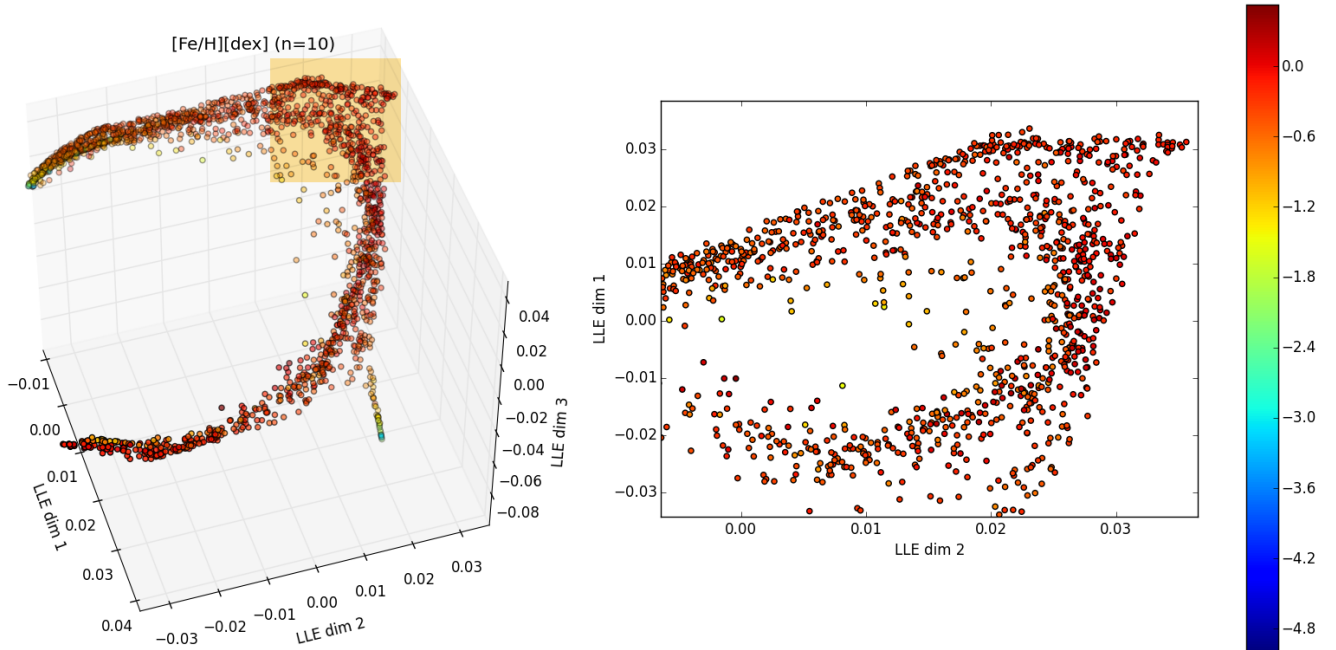


FIGURE 5.5: Left- same LLE projection of 2000 GALAH stars, colour coded with GUESS  $[Fe/H]$ . Right- zoomed in 2D projection of the section in orange, showing a possible metallicity gradient perpendicular to the direction of the over all projection.

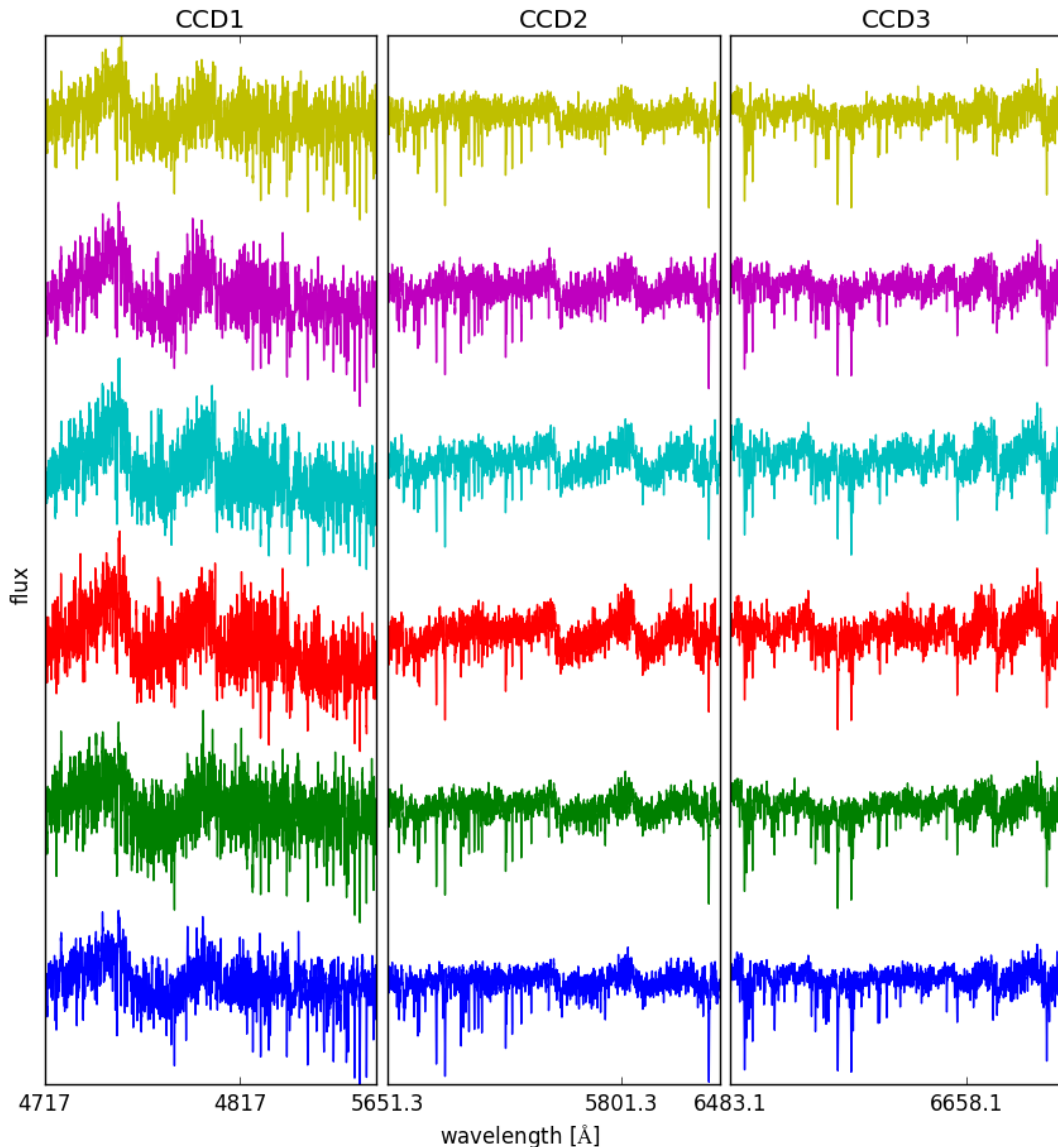


FIGURE 5.6: Spectra of six stars belonging to the outlying group.

stars and can potentially be incorporated as a checkpoint within the overall GALAH data flow structure. Computational time is not an issue as it can be minimised by training LLE on a set of well behaved spectra.

There are two interesting substructures- the delineation of two logg groups in Figure 5.4 and a possible perpendicular metallicity gradient in Figure 5.5. Both structures are small compared to the trend in  $T_{\text{eff}}$ . It is possible that there could exist even weaker substructures corresponding to undiscovered parameters. Thus it could be fruitful to attempt

to remove the  $T_{\text{eff}}$  trend from the projection in order to investigate these substructures further.

# Chapter 6

## Conclusion

### 6.1 Summary of Results

At the time of this writing, all GAP reduced stars have been processed through GUESS. The GUESS sample contains RV and parameters for total of  $\sim 90000$  stars. It is the biggest parameters set available within the GALAH collaboration and has been used by numerous team members.

#### 6.1.1 Radial velocity

Comparing to GAP, GUESS yields more consistent RVs, with the average standard deviation between three CCDs being 0.3 km/s (as opposed to the 0.7km/s from GAP). GUESS RVs are comparable to literature results for M67 and 47Tuc, but give larger cluster dispersions. GUESS RVs are in excellent agreement with APOGEE.

Three data reduction pipelines- GAP, IRAF and HerPy are compared. GAP is found to be suffering from wavelength calibration (indicated by the systematic RV offsets between CCDs) and continuum normalisation issues (indicated by continuum wiggles in CCD 2). It is found that the problematic spectra can be isolated by their LLE coordinates. Continua from IRAF and HerPy do not suffer from the same problem.

### 6.1.2 Parameter estimation

GUESS parameters are found to be comparable to APOGEE, IRFM and ARGOS, and out performs Theremin. Preliminary work has been done in constraining Theremin outputs with GUESS initial parameters. Encouragingly, the new Theremin+GUESS combination appears to produce superior results than any of the two pipelines alone.

LLE projections are colour coded using GUESS parameters.  $T_{\text{eff}}$  is found to be the most dominant parameter, with possible  $\log g$  and [Fe/H] substructures.

## 6.2 Future Work

The most important next step is to incorporate GUESS into the over all GALAH reduction-analysis structure. Work has already begun in adapting GUESS to handle the finalised reduction format. In addition, it will be fruitful to test out the IRAF and HerPy wavelength solutions and implement LLE as a method of isolating peculiar stars. There are also multiple ideas on improving GUESS. Some of them are listed below.

In terms of RV-

- Changing the cross correlating template to an external RV standard library.
- Implement an iterative continuum fitting algorithm to minimise the number of badly weighted stars.

In terms of parameter estimation-

- Testing out different nearest neighbor metric.
- Testing out an empirical grid.
- Implement an iterative algorithm to eliminate artefacts.

# Bibliography

- Aller, L. H. (1991). *Atoms, Stars, and Nebulae*.
- Baglin, A., Auvergne, M., Barge, P., Deleuil, M., Catala, C., Michel, E., Weiss, W., and COROT Team (2006). Scientific Objectives for a Minisat: CoRoT. In Fridlund, M., Baglin, A., Lochard, J., and Conroy, L., editors, *ESA Special Publication*, volume 1306 of *ESA Special Publication*, page 33.
- Bensby, T., Feltzing, S., and Oey, M. (2014). Exploring the milky way stellar disk-a detailed elemental abundance study of 714 f and g dwarf stars in the solar neighbourhood. *Astronomy & Astrophysics*, 562:A71.
- Blackwell, D. E., Petford, A. D., Arribas, S., Haddock, D. J., and Selby, M. J. (1990). Determination of temperatures and angular diameters of 114 F-M stars using the infrared flux method (IRFM). , 232:396–410.
- Bland-Hawthorn, J. and Freeman, K. C. (2004). Galaxy Genesis - Unravelling the Epoch of Dissipation in the Early Disk. , 21:110–120.
- Bland-Hawthorn, J., Krumholz, M. R., and Freeman, K. (2010). The long-term evolution of the galactic disk traced by dissolving star clusters. *The Astrophysical Journal*, 713(1):166.
- Borucki, W. J. et al. (2010). Kepler Planet-Detection Mission: Introduction and First Results. *Science*, 327:977–.
- Bubar, E. J. and King, J. R. (2010). Spectroscopic Abundances and Membership in the Wolf 630 Moving Group. , 140:293–318.
- Burstein, D., Faber, S. M., and Gonzalez, J. J. (1986). Old stellar populations. III - The metallicities of M5, M71, and M67. , 91:1130–1139.
- Carretta, E., Gratton, R. G., Clementini, G., and Fusi Pecci, F. (2000). Distances, Ages, and Epoch of Formation of Globular Clusters. , 533:215–235.

- Casagrande, L., Ramírez, I., Meléndez, J., Bessell, M., and Asplund, M. (2010). An absolutely calibrated  $T_{eff}$  scale from the infrared flux method. Dwarfs and subgiants. , 512:A54.
- Casagrande, L., Silva Aguirre, V., Stello, D., Huber, D., Serenelli, A. M., Cassisi, S., Dotter, A., Milone, A. P., Hodgkin, S., Marino, A. F., Lund, M. N., Pietrinferni, A., Asplund, M., Feltzing, S., Flynn, C., Grundahl, F., Nissen, P. E., Schönrich, R., Schlesinger, K. J., and Wang, W. (2014). Strömgren Survey for Asteroseismology and Galactic Archaeology: Let the SAGA Begin. , 787:110.
- Castelli, F. and Kurucz, R. L. (2004). New Grids of ATLAS9 Model Atmospheres. *ArXiv Astrophysics e-prints*.
- Daniel, S. F., Connolly, A., Schneider, J., Vanderplas, J., and Xiong, L. (2011). Classification of Stellar Spectra with Local Linear Embedding. , 142:203.
- de Laverny, P., Recio-Blanco, A., Worley, C. C., and Plez, B. (2012). The AMBRE project: A new synthetic grid of high-resolution FGKM stellar spectra. , 544:A126.
- De Silva, G. M., D’Orazi, V., Melo, C., Torres, C. A. O., Gieles, M., Quast, G. R., and Sterzik, M. (2013). Search for associations containing young stars: chemical tagging IC 2391 and the Argus association. , 431:1005–1018.
- De Silva, G. M. et al. (2015). The GALAH survey: scientific motivation. , 449:2604–2617.
- De Silva, G. M., Freeman, K. C., Asplund, M., Bland-Hawthorn, J., Bessell, M. S., and Collet, R. (2007). Chemical Homogeneity in Collinder 261 and Implications for Chemical Tagging. , 133:1161–1175.
- Deng, L.-C. et al. (2012). LAMOST Experiment for Galactic Understanding and Exploration (LEGUE) The survey’s science plan. *Research in Astronomy and Astrophysics*, 12:735–754.
- Eggen, O. J., Lynden-Bell, D., and Sandage, A. R. (1962). Evidence from the motions of old stars that the Galaxy collapsed. , 136:748.
- Feng, Y. and Krumholz, M. R. (2014). Early turbulent mixing as the origin of chemical homogeneity in open star clusters. , 513:523–525.
- Freeman, K. and Bland-Hawthorn, J. (2002). The New Galaxy: Signatures of Its Formation. , 40:487–537.

- Freeman, K., Ness, M., Wylie-de-Boer, E., Athanassoula, E., Bland-Hawthorn, J., Asplund, M., Lewis, G., Yong, D., Lane, R., Kiss, L., and Ibata, R. (2013). ARGOS - II. The Galactic bulge survey. , 428:3660–3670.
- Gilmore, G., Randich, S., Asplund, M., Binney, J., Bonifacio, P., Drew, J., Feltzing, S., Ferguson, A., Jeffries, R., Micela, G., and et al. (2012). The Gaia-ESO Public Spectroscopic Survey. *The Messenger*, 147:25–31.
- Gilmore, G. and Reid, N. (1983). New light on faint stars – iii. galactic structure towards the south pole and the galactic thick disc. *Monthly Notices of the Royal Astronomical Society*, 202(4):1025–1047.
- Girard, T. M., Grundy, W. M., Lopez, C. E., and van Altena, W. F. (1989). Relative proper motions and the stellar velocity dispersion of the open cluster M67. , 98:227–243.
- Gustafsson, B., Edvardsson, B., Eriksson, K., Jørgensen, U. G., Nordlund, Å., and Plez, B. (2008). A grid of MARCS model atmospheres for late-type stars. I. Methods and general properties. , 486:951–970.
- Harris, W. E. (1996). A Catalog of Parameters for Globular Clusters in the Milky Way. , 112:1487.
- Heijmans, J. et al. (2012). Integrating the HERMES spectrograph for the AAT. In *Society of Photo-Optical Instrumentation Engineers (SPIE) Conference Series*, volume 8446 of *Society of Photo-Optical Instrumentation Engineers (SPIE) Conference Series*, page 0.
- Henden, A. A., Levine, S. E., Terrell, D., Smith, T. C., and Welch, D. (2012). Data Release 3 of the AAVSO All-Sky Photometric Survey (APASS). *Journal of the American Association of Variable Star Observers (JAAVSO)*, 40:430.
- Holtzman, J. A. et al. (2015). Abundances, Stellar Parameters, and Spectra From the SDSS-III/APOGEE Survey. *ArXiv e-prints*.
- Ibata, R., Irwin, M., Lewis, G. F., and Stolte, A. (2001). Galactic Halo Substructure in the Sloan Digital Sky Survey: The Ancient Tidal Stream from the Sagittarius Dwarf Galaxy. , 547:L133–L136.
- Jofré, P. et al. (2014). Gaia FGK benchmark stars: Metallicity. , 564:A133.
- Kalirai, J. S. (2012). The age of the Milky Way inner halo. , 486:90–92.

- Lee, Y. S., Beers, T. C., Sivarani, T., Allende Prieto, C., Koesterke, L., Wilhelm, R., Re Fiorentin, P., Bailer-Jones, C. A. L., Norris, J. E., Rockosi, C. M., Yanny, B., Newberg, H. J., Covey, K. R., Zhang, H.-T., and Luo, A.-L. (2008). The SEGUE Stellar Parameter Pipeline. I. Description and Comparison of Individual Methods. , 136:2022–2049.
- Letarte, B., Hill, V., Tolstoy, E., Jablonka, P., Shetrone, M., Venn, K. A., Spite, M., Irwin, M. J., Battaglia, G., Helmi, A., Primas, F., François, P., Kaufer, A., Szeifert, T., Arimoto, N., and Sadakane, K. (2010). A high-resolution VLT/FLAMES study of individual stars in the centre of the Fornax dwarf spheroidal galaxy. , 523:A17.
- Lindegren, L., Babusiaux, C., Bailer-Jones, C., Bastian, U., Brown, A. G. A., Cropper, M., Høg, E., Jordi, C., Katz, D., van Leeuwen, F., Luri, X., Mignard, F., de Bruijne, J. H. J., and Prusti, T. (2008). The Gaia mission: science, organization and present status. In Jin, W. J., Platais, I., and Perryman, M. A. C., editors, *IAU Symposium*, volume 248 of *IAU Symposium*, pages 217–223.
- McWilliam, A. and Rich, R. M. (1994). The first detailed abundance analysis of Galactic bulge K giants in Baade’s window. , 91:749–791.
- Mitschang, A. W., De Silva, G., Sharma, S., and Zucker, D. B. (2013). Quantifying chemical tagging: towards robust group finding in the Galaxy. , 428:2321–2332.
- Ness, M., Hogg, D. W., Rix, H.-W., Ho, A., and Zasowski, G. (2015). The Cannon: A data-driven approach to stellar label determination. *ArXiv e-prints*.
- Niemczura, E., Smalley, B., and Pych, W. (2014). *Determination of Atmospheric Parameters of B-, A-, F- and G-Type Stars Lectures from the School of Spectroscopic Data Analyses*.
- Powell, M. J. (2009). The bobyqa algorithm for bound constrained optimization without derivatives. *Cambridge NA Report NA2009/06, University of Cambridge, Cambridge*.
- Prugniel, P., Soubiran, C., Koleva, M., and Le Borgne, D. (2007). New release of the ELODIE library: Version 3.1. *ArXiv Astrophysics e-prints*.
- Recio-Blanco, A., Bijaoui, A., and de Laverny, P. (2006). Automated derivation of stellar atmospheric parameters and chemical abundances: the MATISSE algorithm. , 370:141–150.
- Roweis, S. T. and Saul, L. K. (2000). Nonlinear dimensionality reduction by locally linear embedding. *Science*, 290(5500):2323–2326.

- Rutten, R. J. (2003). *Radiative Transfer in Stellar Atmospheres*.
- Sánchez-Blázquez, P., Peletier, R. F., Jiménez-Vicente, J., Cardiel, N., Cenarro, A. J., Falcón-Barroso, J., Gorgas, J., Selam, S., and Vazdekis, A. (2006). Medium-resolution Isaac Newton Telescope library of empirical spectra. , 371:703–718.
- Sarajedini, A., Dotter, A., and Kirkpatrick, A. (2009). Deep 2MASS Photometry of M67 and Calibration of the Main-Sequence  $J - K_S$  Color Difference as an Age Indicator. , 698:1872–1878.
- Searle, L. and Zinn, R. (1978). Compositions of halo clusters and the formation of the galactic halo. , 225:357–379.
- Sharma, S., Bland-Hawthorn, J., Johnston, K. V., and Binney, J. (2011). Galaxia: A Code to Generate a Synthetic Survey of the Milky Way. , 730:3.
- Shetrone, M., Bizyaev, D., Lawler, J., Allende Prieto, C., Johnson, J. A., Smith, V., Cunha, K., Holtzman, J., Garcia Perez, A., Meszaros, S., Sobeck, J., Zamora, O., Garcia-Hernandez, A., Souto, D., Chojnowski, D., Koesterke, L., and Majewski, S. (2015). The APOGEE Spectral Line List for H band Spectroscopy. *ArXiv e-prints*.
- Skrutskie, M. F. et al. (2006). The Two Micron All Sky Survey (2MASS). , 131:1163–1183.
- Smith, L. I. (2002). A tutorial on principal components analysis. *Cornell University, USA*, 51:52.
- Sneden, C., Bean, J., Ivans, I., Lucatello, S., and Sobeck, J. (2012). MOOG: LTE line analysis and spectrum synthesis. Astrophysics Source Code Library.
- Ting, Y.-S., Freeman, K. C., Kobayashi, C., De Silva, G. M., and Bland-Hawthorn, J. (2012). Principal component analysis on chemical abundances spaces. , 421:1231–1255.
- Urquhart, J. S., Figura, C. C., Moore, T. J. T., Hoare, M. G., Lumsden, S. L., Mottram, J. C., Thompson, M. A., and Oudmaijer, R. D. (2014). The RMS survey: galactic distribution of massive star formation. , 437:1791–1807.
- Valenti, J. A. and Piskunov, N. (1996). Spectroscopy made easy: A new tool for fitting observations with synthetic spectra. , 118:595–603.
- Vanderplas, J. and Connolly, A. (2009). Reducing the Dimensionality of Data: Locally Linear Embedding of Sloan Galaxy Spectra. , 138:1365–1379.
- Xiang, M. S. et al. (2015). The LAMOST stellar parameter pipeline at Peking University - LSP3. , 448:822–854.